

REPORT DOCUMENTATION PAGE

Form Approved OMB No. 0704-0188

Public reporting burden for this collection of information is estimated to average 1 hour per response, including the time for reviewing instructions, searching existing data sources, gathering and maintaining the data needed, and completing and reviewing the collection of information. Send comments regarding this burden estimate or any other aspect of this collection of information, including suggestions for reducing the burden, to Department of Defense, Washington Headquarters Services, Directorate for Information Operations and Reports (0704-0188), 1215 Jefferson Davis Highway, Suite 1204, Arlington, VA 22202-4302. Respondents should be aware that notwithstanding any other provision of law, no person shall be subject to any penalty for failing to comply with a collection of information if it does not display a currently valid OMB control number.

PLEASE DO NOT RETURN YOUR FORM TO THE ABOVE ADDRESS.

1. REPORT DATE (DD-MM-YYYY) 11-06-2010			2. REPORT TYPE Final Report	3. DATES COVERED (From – To) 01-Dec-06 - 11-Jun-10	
4. TITLE AND SUBTITLE Towards the truly predictive 3D modeling of recrystallization and grain growth in advanced technical alloys			5a. CONTRACT NUMBER STCU Registration No: P-262		
			5b. GRANT NUMBER		
			5c. PROGRAM ELEMENT NUMBER		
6. AUTHOR(S) Professor Orest Ivasishin			5d. PROJECT NUMBER		
			5d. TASK NUMBER		
			5e. WORK UNIT NUMBER		
7. PERFORMING ORGANIZATION NAME(S) AND ADDRESS(ES) Institute for Metal Physics, NAS of Ukraine 36 Vernadsky str. Kiev 03142 Ukraine			8. PERFORMING ORGANIZATION REPORT NUMBER N/A		
9. SPONSORING/MONITORING AGENCY NAME(S) AND ADDRESS(ES) EOARD Unit 4515 BOX 14 APO AE 09421			10. SPONSOR/MONITOR'S ACRONYM(S)		
			11. SPONSOR/MONITOR'S REPORT NUMBER(S) STCU 06-8002		
12. DISTRIBUTION/AVAILABILITY STATEMENT Approved for public release; distribution is unlimited.					
13. SUPPLEMENTARY NOTES					
14. ABSTRACT <p>This report results from a contract tasking Institute for Metal Physics, NAS of Ukraine as follows: The need for computer simulation of recrystallization and grain growth is driven by necessity to make quantitative predictions of the microstructure and properties of thermo mechanically processed materials. There are several approaches to modeling the recrystallization phenomenon: vertex models, phase field models, Monte Carlo (MC) models and Cellular automata (CA) models. For our opinion, further development of the MC Potts modeling approach has an outstanding perspective: it allows accounting for many factors which are spatially inhomogeneous and affect grain growth and recrystallization locally in 3D. The goal of the proposed project is to develop the widely used Monte Carlo (MC) Potts model of microstructural evolution in polycrystalline metallic materials to incorporate all possible combinations of exact grain boundary misorientation and inclination. In proposed approach the molecular dynamic (MD) simulation will use for the first time to simulate the misorientational dependence of grain boundary properties. This will help to fill the lack of reliable information on grain boundaries characteristics. As a result a predictive 3D modeling tool will be developed for simulating of microstructural evolution (i.e. grain growth and recrystallization) applicable to advanced technical alloys.</p>					
15. SUBJECT TERMS EOARD, Materials, Metallurgy and Metallography					
16. SECURITY CLASSIFICATION OF:		17. LIMITATION OF ABSTRACT UL	18. NUMBER OF PAGES 81	19a. NAME OF RESPONSIBLE PERSON WYNN SANDERS, Maj, USAF	
a. REPORT UNCLAS	b. ABSTRACT UNCLAS	c. THIS PAGE UNCLAS		19b. TELEPHONE NUMBER (Include area code) +44 (0)1895 616 007	

**Towards the truly predictive 3D modeling
of recrystallization and grain growth
in advanced technical alloys**

P - 262

(EOARD 068002)

Final Project Report

“Towards the truly predictive 3D modeling of recrystallization and grain growth in advanced technical alloys”

Project manager: Prof. Orest M. Ivasishin

Phone: (044) 424-22-10, Fax: (044) 424-33-74, E-mail: ivas@imp.kiev.ua

Participating Institutions: Institute for Metal Physics NASU

Financing countries: USA, EOARD

Project duration: 01 December 2006 – 31 January 2010

Reporting period: 01.12.2006-31.01.2010

Date of submission: 30.03.2010

Stages according to WP and corresponding report section

Reported stages:	<i>Report Section</i>
1. Development of the mathematical background for incorporating the exact grain boundary crystallography into the computer simulation routines.	1.1-1.3
2. Representation of the microstructures and textures using the true 3D geometry with accounting of spatial local textures, development of the integrated computer code for simulation of the recrystallization and grain growth phenomena using exact grain boundary geometry.	1.2-1.5; 2
3. Collecting and systematization of the experimental data on grain boundary crystallographical statistics and information on as deformed microstructures as well as grain boundary misorientation distributions.	8; 11
4. Implementation of molecular dynamic simulation as a source of data on grain boundary energy and mobility.	3; 4; 6; 7
5. Development of the integrated software, in parallel modeling calculations will be performed for the set of different boundaries, which has been agreed with project coordinator. Monte Carlo simulations based on molecular dynamic results will be performed and results will be compared with ones obtained by traditional approaches.	5; 8-10

<i>Content</i>	PAGE 3
Introduction	PAGE 10
1. EXACT GB GEOMETRY	PAGE 11
1.1. Incorporating grain boundary inclination	PAGE 11
1.2. Test run on GBI estimation procedure	PAGE 15
1.3. Implementation of the GBI estimation procedures into 3D Monte Carlo modeling software	PAGE 16
1.4. Implementation of GBM in matrix form	PAGE 18
1.5. MC Modeling of Grain Growth with implemented GBM/GBI	PAGE 20
1.6. MC Modeling of Recrystallization with implemented GBM/GBI	PAGE 24
2. MODELING OF INHOMOGENIOUSLY TEXTURED MATERIAL	PAGE 28
2.1. Introducing texture inhomogeneities into 3D modelling volume	PAGE 28
2.2. MC modeling with texture inhomogeneities in 3D (accounting GBM only)	PAGE 29
2.3. MC Modeling with implemented GBM/GBI (Grain Growth, spatially inhomogeneous texture)	PAGE 32
3. MD ESTIMATION OF RELATIVE GB ENERGIES	PAGE 34
3.1. Testing of cubic and spherical modeling domains.	PAGE 34
3.2. Grain boundary energy as function of GBM.	PAGE 38
3.3. Grain boundary energy as function of GBI.	PAGE 39
3.4. Relative GB energy dependencies on GBI and GBM. 2D maps	PAGE 43

4. MC MODELING WITH IMPLEMENTED GBI AND MD DATA (STEADY STATE GB MIGRATION)	PAGE 48
5. FORMATION AND ANALYSIS OF GB PROPERTIES DATABASE	PAGE 53
5.1. Relative GB energy for specified GBM averaged on possible GBIs	PAGE 53
5.2. Database validation on available experimental data	PAGE 56
5.3. Comparison of different potential usage effect on relative GB energy	PAGE 57
6. β-Ti RECRYSTALLIZATION EXPERIMENT AND ADVANCED MC MODELING	PAGE 60
6.1. Recystallization in cold drawn LCB alloy	PAGE 60
6.2. Recrystallization in specially textured 3D MC volume	PAGE 63
6.3. MC Recrystallization Software development	PAGE 71
7. RELATIVE GB EFFECTIVE MOBILITY	PAGE 72
8. TOOL FOR ANALYSIS OF NOT RELAXED GB GEOMETRY	PAGE 76
9. PUBLICATIONS IN THE FRAMES OF THE PROJECT	PAGE 77
10 . LIST OF REFERENCES	PAGE 77
11. LIST OF SELECTED REFERENCES, STAGE 3	PAGE 78
12. LIST OF SYMBOLS, ABBREVIATIONS, AND ACRONYMS	PAGE 80

LIST OF FIGURES	
Fig.1.1. Geometry of two Cartesian cross sections, namely xz and yz, for the GB $z = f(x,y)$ with GBI close to the xy plane .	PAGE 12
Fig.1.2. GB cross-sections: (a) cross section showing MUs neighboring the M_0 , the best linear fit with the normal direction projection; and (b) cross section including single MU.	PAGE 12
Fig.1.3. Cross-sections generated using test model which represents accuracy of the GBI estimation: (a) exact result for $R=50\text{MU}$; (b), (c) error origin for large and small GB curvature radius, respectively.	PAGE 13
Fig. 1.4. GB curvature radius for most microstructures is larger than average grain size.	PAGE 13
Fig.1.5. GB effective mobility v.s. GBI [3]: (a) Optical microscope image of GB; (b) Dependence of the relative GB energy on crystallographic parameters of the GB plane in two adjacent grains (I and II). The letters A-H refer to eight positions along GB and (c) Dependence of the relative GB energy on the tilt/twist component (TTC) and disorientation angle; d) averaged effective GB mobility as TTC function for 30-45 deg misorientation interval.	PAGE 15
Fig.1.6. Cross-sections generated using test model which represent initially spherical grain shrinkage due to relative GB energy dependence on GBI (TTC): (a) initial state $R=100\text{MU}$; (b), (c) grain shape after 50 and 100MCS. Deviation from the spherical shape is evident.	PAGE 16
Fig.1.7. Modeling volume cross-sections: (a) cross section showing GB normal estimated at M_0 (projection within the section plane; and (b) the same cross-sections with several more GB normal lines projections, at which areas excluded from GB normal estimation are shown by deep blue color.	PAGE 16
Fig.1.8. (a) Grain shape approximated with the Dodecahedron and (b) estimation of GB volume part for which GBI can be derived.	PAGE 17
Fig. 1.9. Cross-sections generated using model of normal grain growth with only GBI dependence of GB effective energy: (a) initial microstructure; (b, c) after 20 and 200 MCS correspondingly.	PAGE 18
Fig.1.10. Effective GB mobility as function of TTC component (a) and of scalar GB misorientation (b).	PAGE 19
Fig.1.11. Cross-sections generated using model of normal grain growth: (a) initial microstructure; (b) with no misorientational but only GBI dependence of GB effective energy after 200MCS; and (c,d) with both misorientational and GBI dependence of GB effective energy after 200 and 800 MCS, correspondingly.	PAGE 20
Fig.1.12. Effective GB mobility as function of scalar GB misorientation only (a); of TTC component (b) and both misorientation and TTC component (c).	PAGE 20
Fig.1.13. Initial microstructure (a) and initial grain size distribution (b) for Cases A to C.	PAGE 21

Fig. 1.14. Predicted grain growth kinetics for Cases A to C.	PAGE 21
Fig.1.15. Initial microstructure (a) and grain size distribution (b) for Case D.	PAGE 22
Fig. 1.16. Schematically: difference in GBI dispersion for Cases A to C and D.	PAGE 23
Fig. 1.17. Predicted grain growth kinetics for Case D in comparison with the Case C (dashed line).	PAGE 23
Fig. 1.18. Predicted microstructures for Case D (a) initial, after 150 MCS (b) and 500 MCS (c). (d, e). Initial (d) and predicted grain size distribution (500 MCS).	PAGE 24
Fig.1.19. (a) 3D image of selected deformed grains and some rex. nuclei, and (b) cross-section (b) generated for simulation initial microstructure.	PAGE 25
Fig.1.20. Stored energy distribution shown with color (blue to red scale) within the modeling domain. Cross-sections generated transverse plane (a) and rolling plane (b) and 3D image (c) showing some rex. nuclei and not recrystallized volume after 50 MCS (Case A).	PAGE 25
Fig.1.21. Effective GB mobility as function of both scalar GB misorientation TTC component.	PAGE 25
Fig. 1.22. MC predicted microstructures after 75 MCS: (a) Case A (90% rex.) and (b) Case B (80% rex.)	PAGE 26
Fig. 1.23. Predicted recrystallization kinetics for Cases A and B.	PAGE 26
Fig. 1.24. Predicted microstructures for Cases A and B after recrystallization completes: a) Case A, 100 MCS b) Case B, 250 MCS.	PAGE 27
Fig. 2.1. Interface for introducing the spatial texture inhomogeneities into the modeling volume.	PAGE 28
Fig. 2.2. Local textures implemented into the model of deformed material microstructure. Spatial region A corresponds to the 001 fiber texture, region B is close to 011 texture component and region C is random background (undefined).	PAGE 28
Fig. 2.3. Local textures implemented into the model of material microstructure, with bands consisting from small subgrains of low misorientation.	PAGE 30
Fig. 2.4. Cross sections of locally textured initial modeling volumes: (a) and (b) BW/SBG ratio is 10 and 4 respectively.	PAGE 30
Fig. 2.5. Growth of large grains at textured band boundaries, as predicted by MC modeling for BW/SBG = 10 case, after: (a) 10 MCS; (b) 20 MCS; (c) 50 MCS. Slow growth of subgrains within the bands also occurs.	PAGE 30
Fig. 2.6. Growth of grains as predicted by MC modeling for BW/SBG = 4 case, after: (a) 30 MCS; (b) 100 MCS; (c)150 MCS.	PAGE 31
Fig. 2.7. Two bcc lattice orientations within the modeling volume and major GB orientation within the modeling volume (most probable GBI) (a), and (b) initial microstructure (cross-section) for modeling volume.	PAGE 32
Fig. 2.8. Modeling domain initial texture ODF; (a) (intensities in MU per angular unit) and (b) ODF.	PAGE 32

Fig. 2.9. Effective GB mobility as function of both scalar GB misorientation TTC component and its relation with modeling volume texture components (A) and (B) (schematically).	PAGE 32
Fig. 2.10. MC predicted microstructures after (a) 75 MCS; (b) 200 MCS; c) 400 MCS; and d) 800 MCS.	PAGE 33
Fig. 3.1. Cubic MD modeling domain of 2300 atoms with two lattices in different misorientations.	PAGE 34
Fig. 3.2. Spherical MD modeling domain of 1650 atoms with two lattices in different misorientations and inclinations.	PAGE 35
Fig. 3.3. Simple pair interatomic potential and STGB geometry assumed for test MD run.	PAGE 35
Fig. 3.4. Geometry of the [100] STGB, projection on (001) plane (not relaxed).	PAGE 36
Fig. 3.5. [100] STGB model (relaxed).	PAGE 37
Fig. 3.6. Relative STGB [100] energy as function of misorientation, MD simulation	PAGE 37
Fig. 3.7. Result for bcc STGB [100] obtained in [8].	PAGE 38
Fig. 3.8. Geometry of the simulated GB (central horizontal plane) with misorientation (a) (30, 90, 30) and, (b) (30, 19, 30), central part of the modeling volume.	PAGE 38
Fig. 3.9. GB energy for (30, Theta, 30), Theta = [0, 90] boundary. Positions 1 and 2 correspond to atomic structures (a) and (b), respectively, Fig. 3.8.	PAGE 39
Fig. 3.10. Introducing GBI into GB energy estimation procedure.	PAGE 39
Fig. 3.11. GB energy for (30, 0, 30) (0,0,0) misorientation; GBI = [0 to 70] deg. (a) all data and (b) – points for 0 and 1 deg GBI are excluded.	PAGE 39
Fig. 3.12. Relative GB energy for (45, Theta, 45), Theta = [0, 20] boundary. Marked positions correspond to CLS patterns presented on Fig.3.14	PAGE 40
Fig. 3.13. Relative GB energy for (45, Theta, 45), Theta = [0, 90] boundary. Marked position corresponds to $\Sigma 9$ CLS GB.	PAGE 40
Fig.3.14. GB for (45, Theta, 45) (0, 0, 0) CLS visualization: Theta = (a) 34.6 (b) 38.6 and 38.8 (c) deg.	PAGE 41
Fig 3.15. GB energy for (45, Theta, 45), Theta = [38, 39] boundary. Position. (c) corresponds to $\Sigma 9$ CLS GB.	PAGE 41
Fig. 3.16. GB energy as function of GBI. GB misorientation (30, 30, 30) (0,0,0) (a). Not inclined GB position is shown by bold arrow on the GB energy misorientation dependence (b).	PAGE 42
Fig. 3.17. GB energy as function of GBI. GB misorientation (45, 0, 0) (0,0,0), rotation around 100 axis.	PAGE 43
Fig.3.18. GB inclination for (0,0,0)(20,20,20): GBM (a) $\omega = 0$ deg, $\phi = 20$ deg; (b) $\omega = 20$ deg, $\phi = 20$ deg	PAGE 43

Fig. 3.19. Relative GB energy for GBI (0, 0, 0) (20,20,20). Inverted color scheme used for points on lines AB and CD.	PAGE 44
Fig. 3.20. Relative GB energy for sections A-B (a) and C-D (b) (see Fig. 2). Marked position (bold arrows) correspond to geometry, for which GB normal orientation is close to 110 direction of (20,20,20) oriented part of bicrystal.	PAGE 44
Fig.3.21. Relative GB energy smoothed (adjusted-averaging) color map for GBI (0, 0, 0) (20,20,20), $\phi \in [0, 90]$ and $\omega \in [0, 90]$.	PAGE 45
Fig. 3.22. Relative GB energy 3D plot, scale divided by factor 2 is used for best imaging	PAGE 45
Fig. 3.23. GB Energy maps (J/Unit Cell) as function of GBI for series of GBM (0,0,0 – x,y,z) : a) x,y,z = 1,3,7; b) 6,15,55 c) 8,2,6 d) 25,20,60 e) 40,15,10 f) 50, 0, 10	PAGE 46-47
Fig. 4.1 Initial GB geometry for 3D MC and MD simulation (a) cross-section and (b) 3D view.	PAGE 48
Fig. 4.2. GB energy as function of GBI (used as GB effective mobility in 3D MC runs). GB misorientation (30, 30, 30) (0,0,0).	PAGE 48
Fig. 4.3. MC simulated GB migration in bicrystal (3D half-loop geometry) with inclination independent GB effective mobility (a) and locally GB inclination dependent effective mobility (b).	PAGE 49
Fig. 4.4. Cross sections are parallel to the 001 planes of the “external” lattice.	PAGE 50
Fig. 4.5. Effective GB mobility (Fig. 1.33) for (0, 0, 0 20, 20, 20) misorientation - proportional to the GB relative energy GBI dependence	PAGE 50
Fig. 4.6. Analysis of GB faceting in 3D after 4000 MCS. Reconstruction by voxels in gray light (a) and colored facets (b).	PAGE 52
Fig. 5.1. GB energies for misorientations of: (a) 2 deg.; (b) 3 deg.; (c) 10 deg.; (d) 13 deg.; (e) 29 deg and (f) 45 deg presented as dependence on Bunge angles variant number in corresponding dataset (proportional to first rotation angle, for GBI (20, 20)	PAGE 55
Fig. 5.2. Averaged for all orientation variants GB energy as function of misorientation (a) GB Inclination = (20, 20); (b) GB Inclination = (30, 30).	PAGE 56
Fig. 5.3. Bicrystal with a [1 1 0] asymmetric tilt boundary [15]. The misorientation is defined as the angle θ (= 38,9 deg) between the [0 0 1] directions of two single-crystal grains, and the inclination is defined as the angle φ between the boundary plane and the bisector of the misorientation	PAGE 56
Fig. 5.4. Dependence of the tilt grain boundary energy on inclination φ : (a) MD estimated, lines correspond to deep spline averaging (dash green) and bin (20) averaging (solid blue) and, (b) experimentally measured in [15].	PAGE 57
Fig. 5.5. Relative GB energy for GBI (0, 0, 0) (20,20,20). (a) Born-Mayer map (b) – Lennard-Jones map and (c) Lennard-Jones map rescaled for 4 levels	PAGE 58

Fig. 5.6. Relative GB energy for GBI (0, 0, 0) (20,20,20) calculated with Lennard-Jones (solid line) and Born-Mayer (dashed line) potentials.	PAGE 58
Fig. 6.1. Optical (left) and EBSD (right) images of a) solid solutioned; b) cold drown; c) 50% Recrystallized and d) 100% recrystallized material.	PAGE 61
Fig. 6.2. Predicted recrystallization kinetics for Cases A and B.	PAGE 62
Fig. 6.3. Simulated microstructures for Cases 1 (left) and 2 (right). GB color is proportional (red GBs > 15 deg mis, other < 15, blue < 2 deg)	PAGE 62-63
Fig. 6.4. LCB 95% Rex. EBSD Grain Boundary Map (400*500 μm) shows grain arrangements (marked with green color) which looks similar to Case 4 simulated patterns (right).	PAGE 63
Fig. 6.5. Initial (as-deformed) microstructure.	PAGE 64
Fig. 6.6. Dependence of GB energy on GBI for high symmetry GBMs: (a) (45,45,45) and (b) (45,45,0).	PAGE 64
Fig. 6.7. Dependence of relative GB energy on GBI for general GBMs from table 6.1	PAGE 65-68
Fig. 6.8. Recrystallization kinetics for Cases 1 and 2.	PAGE 69
Fig. 6.9. Microstructural evolution: (a) Case 1; and (b) Case 2.	PAGE 69-70
Fig. 6.10. Some favorite GB planes for Case 2, 60 MCS.	PAGE 70
Fig. 6.11. MC Potts Rex. and GG software: (a) modeling volume analysis; (b) searching for GB energy value within included database.	PAGE 71
Fig 7.1. Steady state GB migration (half-loop) geometry as proposed for MD estimation of GB mobility (a) and (b) – geometry, often used for experimental GB mobility estimation.	PAGE 72
Fig. 7.2. Experimental GB mobility estimation for Al alloy [11]. (a) low temperature, essential GBI dependence (three nearly flat segments), (b) high temperature, almost no GBI dependence	PAGE 73
Fig. 7.3. Example of spatial orientation of the rolled sample with respect to the magnetic field H, provides essential driving for GBs force due to the anisotropy of the magnetic susceptibility of titanium (magnetic annealing of titanium, [12])	PAGE 73
Fig. 7.4. Relative GB energy for (0,0,0) (20,20,20) misoriented GB as function of GBI component ϕ . Open circles are GB energy values when additional driving force is effective.	PAGE 74
Fig. 7.5. Example of flat relaxed GB in MD simulation	PAGE 74
Fig. 7.6. Migrating hemispheric GB geometry used in MD simulation.	PAGE 75
Fig. 8.1. CLS visualization tool (a) and CLS patterns changing from LABs to HABs (twist GB, $\Theta= 2 \text{ deg.}$ (b), 4 deg. (c), 6 deg. (e) 12 deg and (f)15 deg).	PAGE 76

INTRODUCTION

The final microstructures and textures of most technical alloys are the result of their multistage thermomechanical processing. Hence, characterizing and understanding of microstructure and texture evolution during various thermomechanical processes are important for improving their behavior and properties.

Recently, computer modeling of microstructural evolution has established itself as an essential tool for predicting final (post processing) microstructures and properties. The most important components of polycrystalline materials are internal interfaces and, especially, grain boundaries separating adjacent crystals (grains) with identical chemical composition and crystallography, that differ only by mutual misorientation of their crystal lattices. The grain boundaries in polycrystalline create a three-dimensional net spreading throughout the material (the main feature of the microstructure); they have different properties and therefore, they substantially contribute to the behavior of the material through forming material grain structure and crystallographic texture. Due to a large variety of possible misorientations of the adjacent grains, as well as of the orientation of the actual joining planes, there is a huge number of grain boundaries possessing different structures and thus, different properties.

A weak point of grain growth and recrystallization modeling is lack of reliable information on characteristics of grain boundaries (GB energy and mobility), which are critical for quantitative modeling. It was assumed in all previous computer models (and in experiments on grain boundary migration in bicrystals) that the spatial orientation of a boundary does not seriously affect GB energy and mobility. This is not true, because in the case of a curved GB its structure (and properties) changes along the boundary.

Hence, the aim of the project was to build a really predictive model of recrystallization and grain growth. A number of problems were solved, including accounting of an exact grain boundary crystallogeometry, i.e. local GBI together with three-parameter GBM as arguments for local GB energy and mobility, development of modeling procedure. MD simulation together with recent experimental data analysis were applied for obtaining effective values for GB energy and mobility for all possible combinations of exact GBM and GBI. An attempt of estimating realistic data for MC modeling concerning deformed technical Ti-based alloy (LCB) (grain and subgrain structure, GBM and GBI distributions) and introducing them as starting conditions for MC modeling has been performed.

1. EXACT GB GEOMETRY.

Stage 1 of project was aimed at implementing of an exact description of grain boundary geometry into the MC Potts modeling procedure instead of commonly used scalar GBM. It was shown how two-parameter grain boundary inclination (GBI) could be accounted in modeling procedure. GBMs were presented in their exact matrix form.

In all previous computer models of microstructure evolution it was assumed that the spatial orientation of a boundary does not seriously affect grain boundary energy and mobility. However, structure and properties of a curved grain boundary changes along the boundary. Hence, to build a really predictive model of recrystallization and grain growth not only three-parameter grain boundary misorientation (GBM) but local grain boundary inclination (GBI) must be accounted as arguments for local grain boundary energy and mobility.

In this project formulation of the mathematical background for incorporating the exact grain boundary crystallography into the computer simulation routines (algorithm aimed to derive local grain boundary inclination (GBI) for the Monte-Carlo (MC) Potts modeling volume unit (MU) at grain boundary (GB)) was carried out. Simple and effective routine for GBI estimation was created and implemented into the basic MC Potts code. GBM was implemented into MC Potts modeling in matrix form. Test programs were run to show how the “pure” GB properties dependence on GBI affects both the isolated grain shrinkage and the modeling microstructure evolution.

1.1. Incorporating grain boundary inclination (GBI)

Algorithm aimed at deriving local GBI for the MC Potts modeling volume point at GB was formulated basing on following assumptions. Unlike GBM, the GBI should be determined locally. The GBI is a subject to constant change while GB migrates, hence information obtained during previous MC steps cannot be used for next ones. Therefore, it is not worthwhile to use the most precise approach, namely GB approximation by spatial (3D) analytical function because one needs to repeat this time-consuming procedure after each elementary MC event. Another problem with GBI estimation procedure, if based on analytical function fit, is that GB may consist from very different number of MUs; up to thousands; this makes developing of the unified fit procedure very complicated. Let us consider the case when the GB is represented by function $z = f(x, y)$. We suggest to estimate GBI locally using planar linear approximations for basic Cartesian GB cross-sections. Cross-sections parallel to xz and yz through the $M_o(x, y, z)$ point in the modeling volume for which local GBI should be estimated are shown in Fig. 1.1.

Partial derivatives $\partial f / \partial x$ and $\partial f / \partial y$ define tangential lines for each cross-section. Then, tangential plane for $z = f(x, y)$ includes two tangential lines within the cross-sections parallel to xz and yz , angles α and β are determined by linear approximation. Tangential plane normal, that characterizes GBI in point M_o is:

$$\bar{m} = \left(\frac{\partial f}{\partial x}(M_o); \frac{\partial f}{\partial y}(M_o); -1 \right),$$

and normal line (which includes given MU) equation is:

$$\frac{x - x_0}{\frac{\partial f}{\partial x}(M_0)} = \frac{y - y_0}{\frac{\partial f}{\partial y}(M_0)} = \frac{z - z_0}{-1}.$$

Next algorithm was developed. For each cross-section the nearest vicinity (48MUs) of the MU under consideration was taken into account, as shown in Fig. 1.2a. Although two Cartesian cross-sections are sufficient for linear approximation sometimes number of MUs within one of them is not enough, as shown in Fig 1.2b. We propose to use three Cartesian cross-sections to guarantee that at least two of them will be suitable for linear approximation.

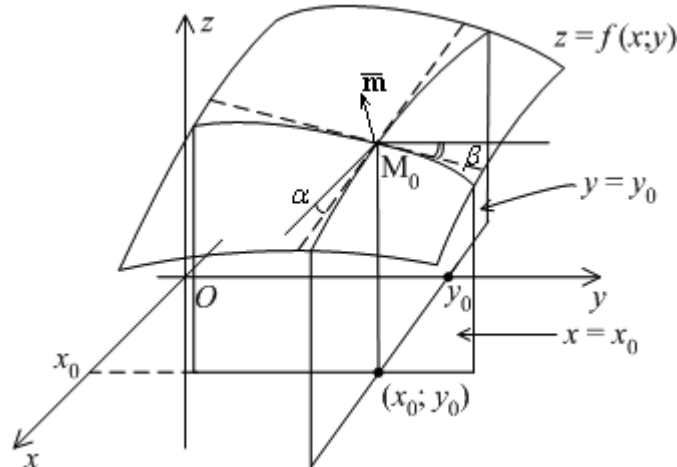


Fig.1.1. Geometry of two Cartesian cross sections, namely xz and yz , for the GB $z = f(x,y)$ with GBI close to the xy plane .

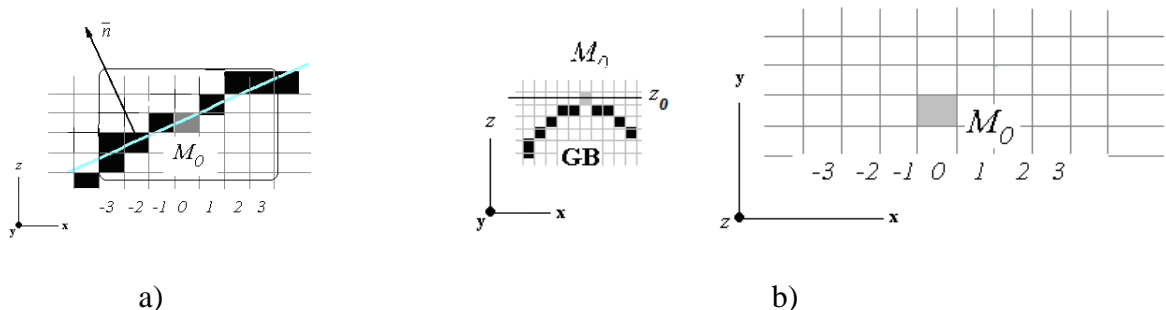


Fig.1.2. GB cross-sections: (a) cross section showing MUs neighboring the M_0 , the best linear fit with the normal direction projection; and (b) cross section including single MU.

For procedure error estimation a model of spherical grain of different radius R was tested. Such test geometry insured that all possible GBIs and curvatures would be tried. The second advantage is that unlike for real GB, exact GB tangential plane position is known.

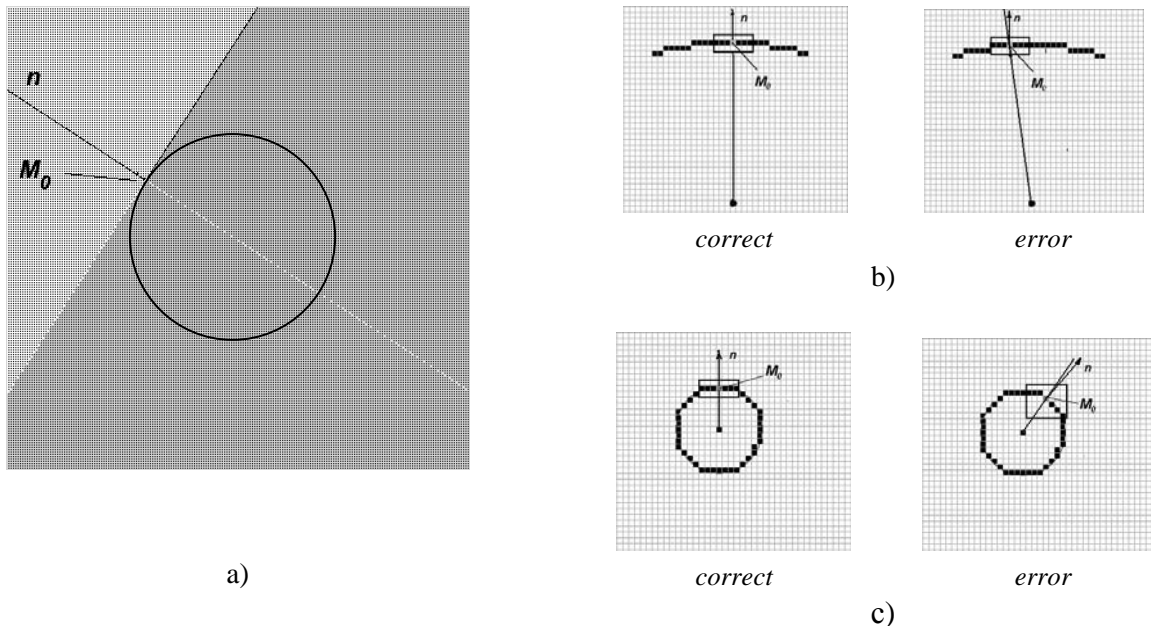


Fig.1.3. Cross-sections generated using test model which represents accuracy of the GBI estimation: (a) exact result for $R=50\text{MU}$; (b), (c) error origin for large and small GB curvature radius, respectively.

It was assumed that acceptable average error, i.e. angle between exact and estimated normals is 2 deg., i.e. not more than commonly used Euler angle step for discrete representation of orientations. Fig. 1.3a presents the cross-section of simulated spherical grain and a normal line projection estimated by using the above procedure.

The acceptable errors were obtained for more than 99% estimations at all curvatures having radius above 20MU. For small curvatures a number of successful estimations dropped to 94%. The average errors are shown in Table 1.1. For GB curvatures above 50MU average error in GBI estimation remains constant, i.e. result is not improved with further growth of GB curvature. Figures 1.3b and 1.3c illustrates origin of errors in GBI estimation for large and small GB curvatures, correspondingly.

1.

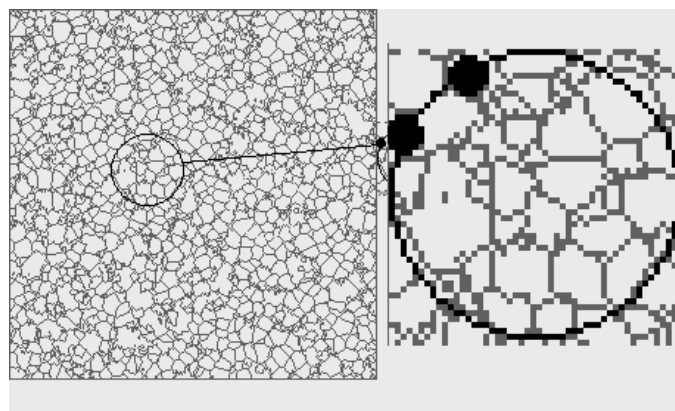


Fig. 1.4. GB curvature radius for most microstructures is larger than average grain size.

Usually GB curvature radius 20MU corresponds to microstructure of average grain size 10-12MU [5]. Fig. 1.4 illustrates correspondence between GB curvature in real modeling microstructure and the curvature of the spherical grain. The conclusion is that procedure developed cannot define correctly GBI for small grains (GB segments) because the whole GB segment is smaller than working field shown in Fig. 1.2a. For fine microstructures we propose to use 5×5 working field (25 MUs), what still gives acceptable results.

It should be mentioned that contrary to study [7] in which method of estimation of GBI in discrete microstructural modeling for modeling volumes was proposed, our procedure does not require adding extra information for data storage.

Table 1.1. Error (angle between estimated and exact normal to GB) statistics versus GB curvature radius R, based on 200 estimations for randomly selected GBI for each R.

Curvature Radius, R	100	50	30	25	20	15	10	8
Average error, deg	1.641	1.687	2.255	2.536	2.423	4.301	6.562	7.24
Standard deviation, deg	1.029	1.039	1.642	1.77	1.643	3.002	4.301	4.167
Fraction of exact GBI determination, %	10.5	13.0	11	11	10	8	5	6
Unsuccessful , % (error > 2%)	N/A	N/A	0.5	0.5	1.0	0.5	4.0	6.0

1.2 Test run on GBI estimation procedure

For procedure test run model, shrinkage of spherical grain ($R = 100\text{MU}$) was modeled. Such test geometry insured that all possible GBIs and curvatures would be tried. Test mimics the one described in [4], which was aimed to prove the MC procedure validity by modeling the shrinking spherical grain. The grain/matrix misorientation was taken as 35 degrees. In [4] the GBM was the only parameter which defined the boundary mobility. The grain remained spherical until full disappearing. In our case, the boundary is defined not only by GBM but GBI as well. The experimental data were found on how GBI affects effective GB mobility/energy [3]. Unlike previous works, the paper [3] was not restricted to plane boundaries only (simple tilt or twist) around high symmetry lattice directions. Fig. 1.5 illustrates these experimental data for combined twist and tilt GBs in NiAl alloy. Our test MC model was run using GB properties versus GBI according to [3].

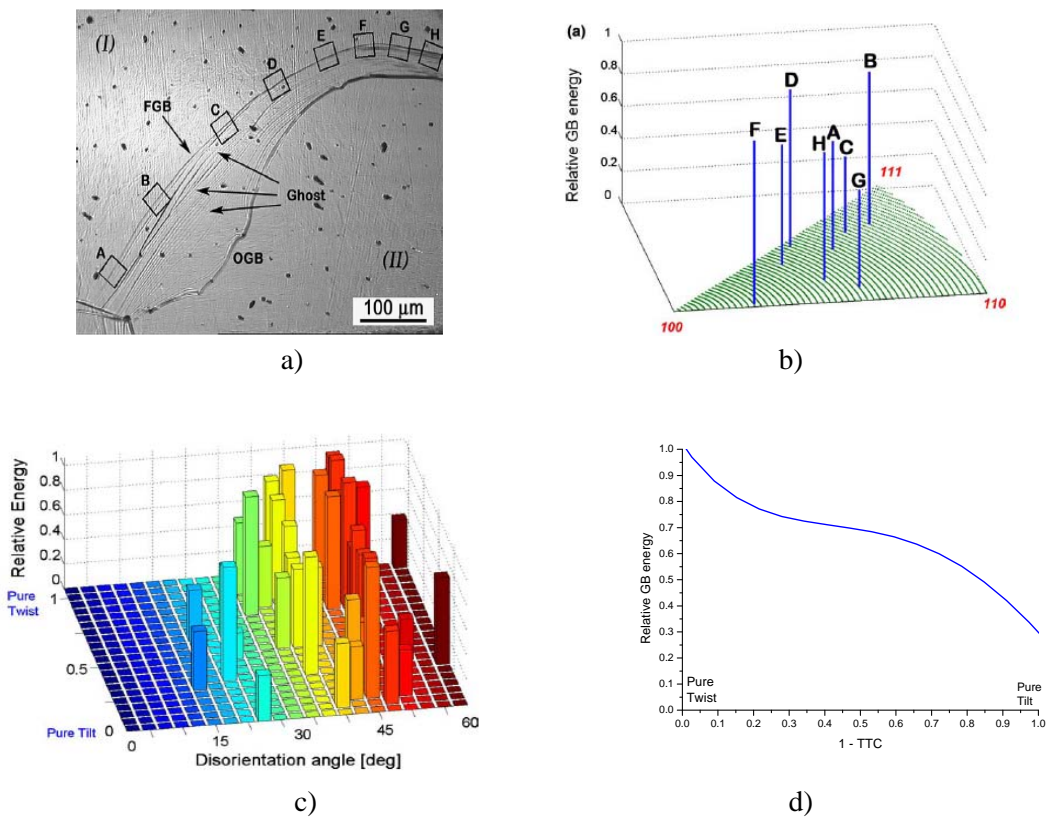


Fig.1.5. GB effective mobility v.s. GBI [3]: (a) Optical microscope image of GB; (b) Dependence of the relative GB energy on crystallographic parameters of the GB plane in two adjacent grains (I and II). The letters A–H refer to eight positions along GB and (c) Dependence of the relative GB energy on the tilt/twist component (TTC) and disorientation angle; d) averaged effective GB mobility as TTC function for 30–45 deg misorientation interval.

For convenience, we followed the tilt/twist component (TTC) definition, according to [3], $\text{TTC} \equiv [U, V, W] \cdot \vec{n}_2$, where both vectors were normalized to unity. Its value varied from 0 for pure tilt GBs to 1 for pure twist GBs. The general case of $0 < \text{TTC} < 1$ described a mixed type GB, with TTC representing the fraction of the twist component in the GB. GBM between grain and matrix was chosen to be between 30 and 45 deg (this value to be referred to fig.1.5c, from where averaged relative GB energy dependence on TTC was derived (Fig. 1.5d)). As expected, account of GBI resulted in different GB migration velocities for different TTC, as shown in Fig. 1.6.

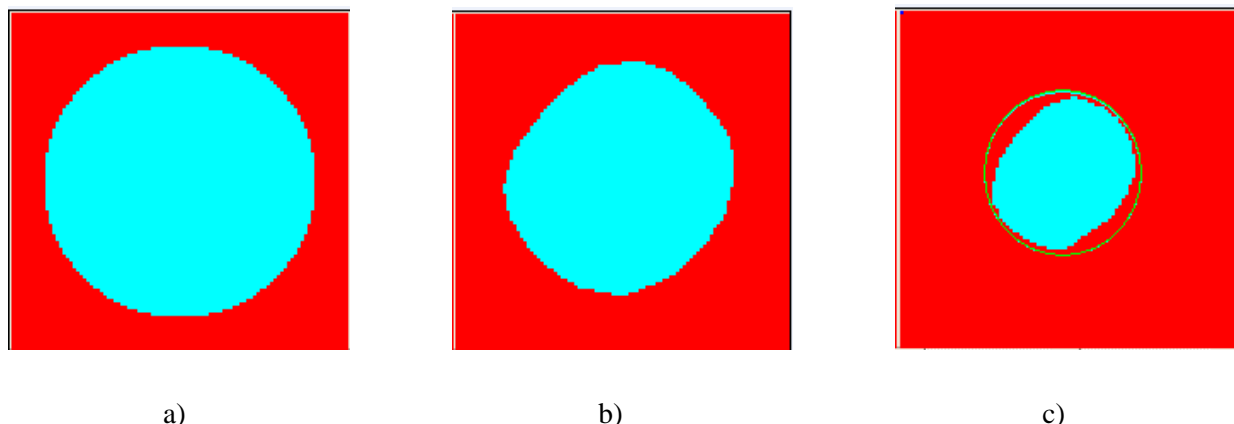


Fig.1.6. Cross-sections generated using test model which represent initially spherical grain shrinkage due to relative GB energy dependence on GBI (TTC): (a) initial state $R=100\text{MU}$; (b), (c) grain shape after 50 and 100MCS. Deviation from the spherical shape is evident.

1.3 Implementation of the GBI estimation procedures into 3D Monte Carlo modeling software

Procedure developed for GBI estimation cannot define correctly GBI for smaller grains and GB segments close to triple lines because the whole GB segment is smaller than working field. Hence, if M_0 point is located close to triple line or triple line junction, it is impossible to derive GBI from the MC Potts modeling volume due to low resolution of the discrete modeling volume grid. Figure 1.7b illustrates spatial limitations for the GBI determination procedure. Since the procedure for GBI determination needs at least 4 nearest to M_0 GB MUs to be present within each Cartesian cross-section it can not work with GB curvature radius less then 4 MU. Areas of triple lines or triple line junctions are shown in Fig. 1.7b by deep blue filling. The procedure was proposed that excludes triple line vicinity areas from the GBI estimation.

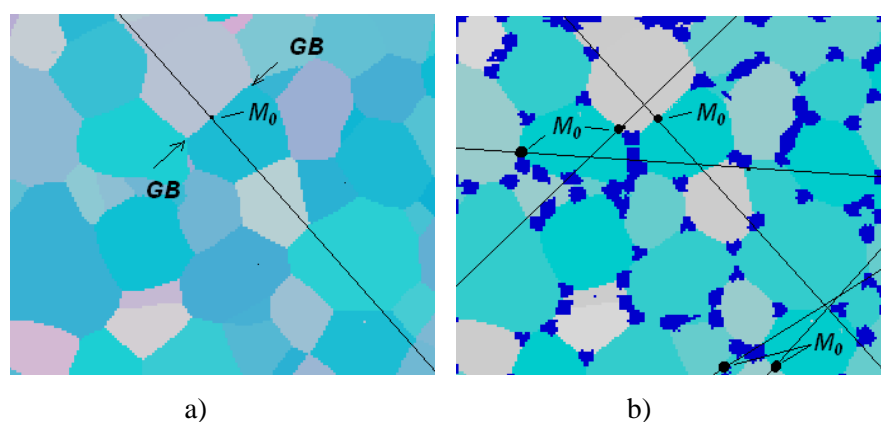


Fig.1.7. Modeling volume cross-sections: (a) cross section showing GB normal estimated at M_0 (projection within the section plane; and (b) the same cross-sections with several more GB normal lines projections, at which areas excluded from GB normal estimation are shown by deep blue color.

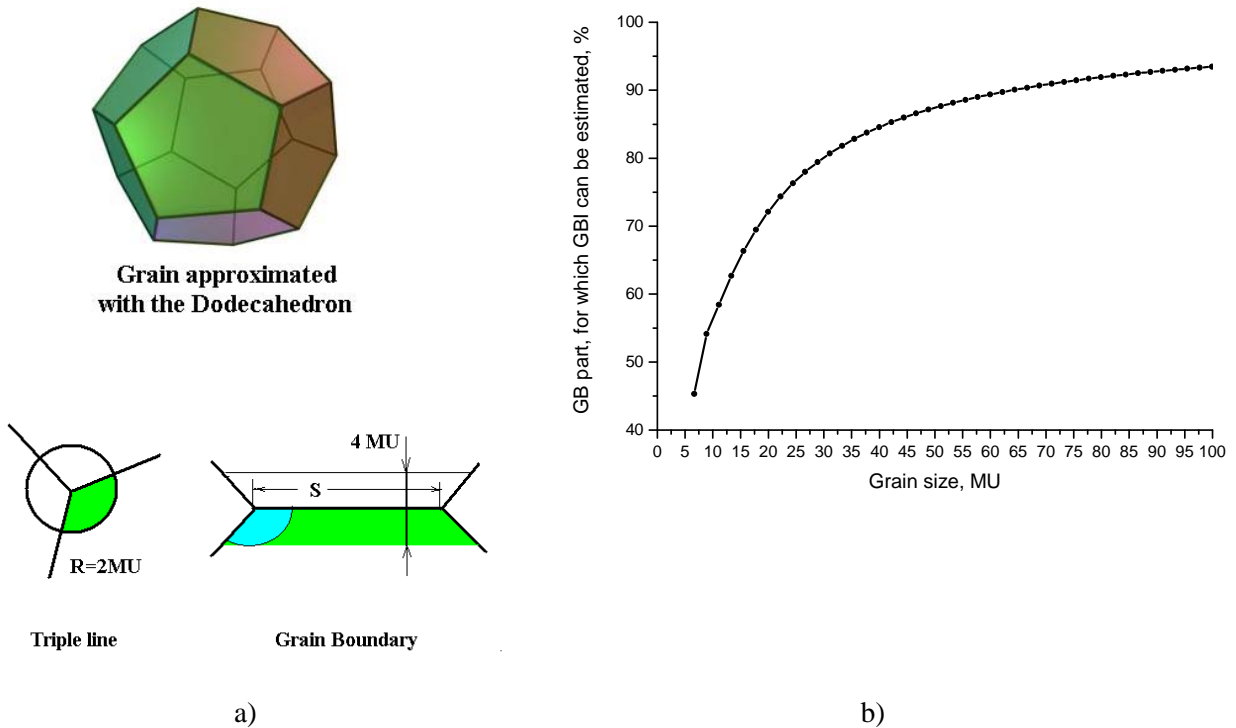


Fig.1.8. (a) Grain shape approximated with the Dodecahedron and (b) estimation of GB volume part for which GBI can be derived.

Excluded part of GB estimated by taking the Dodecahedron as the grain shape approximation and excluding the triple line volume from the GB volume is shown in Fig 1.8a. Taking into account that Dodecahedron internal radius (1/2 of grain size) is approximately 1.12 S (S is the edge of polyhedron), GB part for which GBI can be estimated was derived. As it seen from Fig. 1.8b, the whole algorithm works good starting from grain sizes of 20-25 MUs, when not less than 70% of GB volume for most microstructures can be accounted.

Figure 1.9 presents an implementation of the effective GB energy which depends on GBI as shown on Fig. 1.5d. Effect of GBI on microstructure is obvious, however, grain shapes look unrealistic due to absence of misorientational dependences of GB properties. Thus, effect of “pure” GBI influence on GB kinetics was illustrated. Modelling with accounting of both GBM and GBI dependencies will be described in section 1.5.

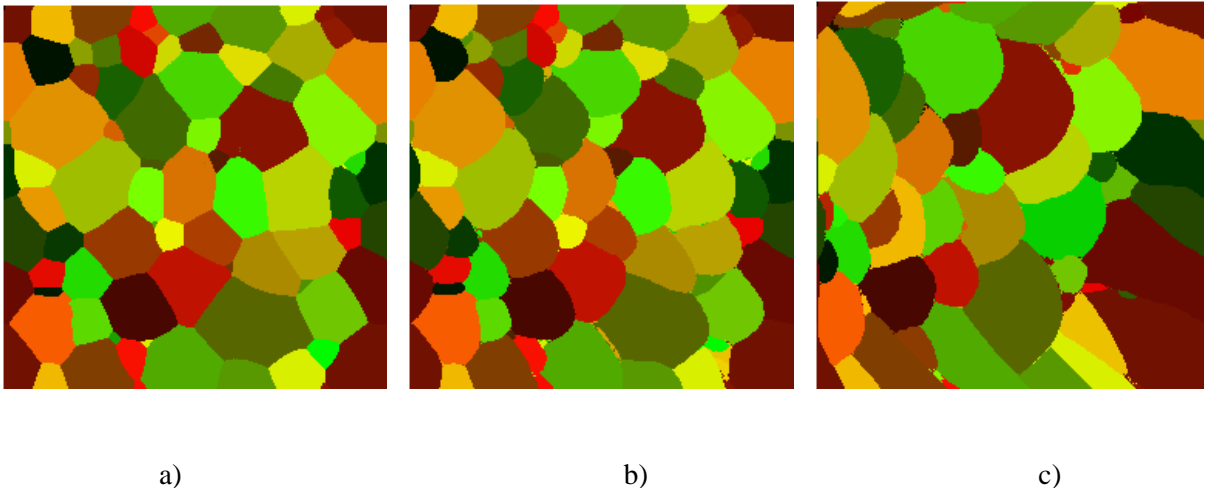


Fig. 1.9. Cross-sections generated using model of normal grain growth with only GBI dependence of GB effective energy: (a) initial microstructure; (b, c) after 20 and 200 MCS correspondingly.

1.4. Implementation of GBM in matrix form

The MC Potts software for recrystallization and grain growth was updated with the GBM presentation in the exact matrix form. Previously, the single parameter consisting of the lattice misorientation between neighboring grains was used to define the relative grain-boundary energy and mobility.

$$\varepsilon = \arccos\left(\frac{m_{11} + m_{22} + m_{33} - 1}{2}\right).$$

The present modeling routine uses the exact matrix misorientation \mathbf{M} between grains having orientations g_1 and g_2 :

$$\mathbf{M} = \mathbf{M}_{g_1} \times \mathbf{M}_{g_2}^{-1} = \begin{pmatrix} m_{11} & m_{12} & m_{13} \\ m_{21} & m_{22} & m_{23} \\ m_{31} & m_{32} & m_{33} \end{pmatrix},$$

where the rotation matrices \mathbf{M}_{g_1} , \mathbf{M}_{g_2} correspond to orientations g_1 and g_2 of the neighboring grains. If the lattice symmetry is higher than triclinic, one also needs to take into account the existence of equivalent rotations.

The evaluation of the matrix misorientation would require very long time if done for each MC trial, even using effective calculation schemes such as that based on quaternions [5]. Therefore, a database of \mathbf{M}

as a discrete function of g_1 and g_2 was calculated and loaded into the computer memory prior to modeling. Thus, only a single search operation should be performed for each MC trial. Because of lack of reliable information on characteristics of grain boundaries (misorientation dependent GB effective mobility), for present test simulations the schematic matrix form of GBM dependence has been developed, which is equivalent to scalar form of GBM dependence presented on Fig. 1.10b. Taking into account that scalar misorientation between neighboring grains is:

$$\varepsilon = \arccos\left(\frac{m_{11} + m_{22} + m_{33} - 1}{2}\right),$$

grain boundaries were classified as LABs if $|Sp(\mathbf{M})| = |m_{11} + m_{22} + m_{33}| > 2.96$, transition boundaries (from LAB to HAB) if $2.92 < |Sp(\mathbf{M})| < 2.96$ and HABs if $|Sp(\mathbf{M})| < 2.92$.

As it is shown in Chapter 2, GBM dependence can be derived from molecular dynamics modeling.

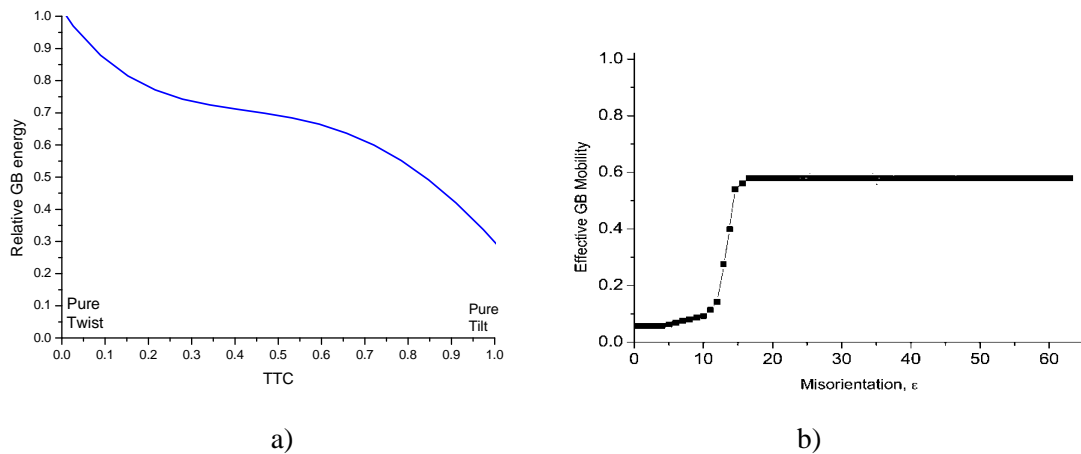


Fig.1.10. Effective GB mobility as function of TTC component (a) and of scalar GB misorientation (b).

Figure 1.11(a, b, c) presents evolution of microstructure modeled with the above assumption. As expected, more realistic final microstructures were obtained when both GBM and GBI dependencies were introduced to the MC routine in comparison with the case when only GBI dependence of effective GB mobility was accounted. Some lower grain growth rate was observed due to the decrease of the average GB effective mobility when GBM is accounted.

If initial microstructure (Fig. 1.11a) evolves only under GBI dependence, it changes as shown in Fig. 1.11 d, e.

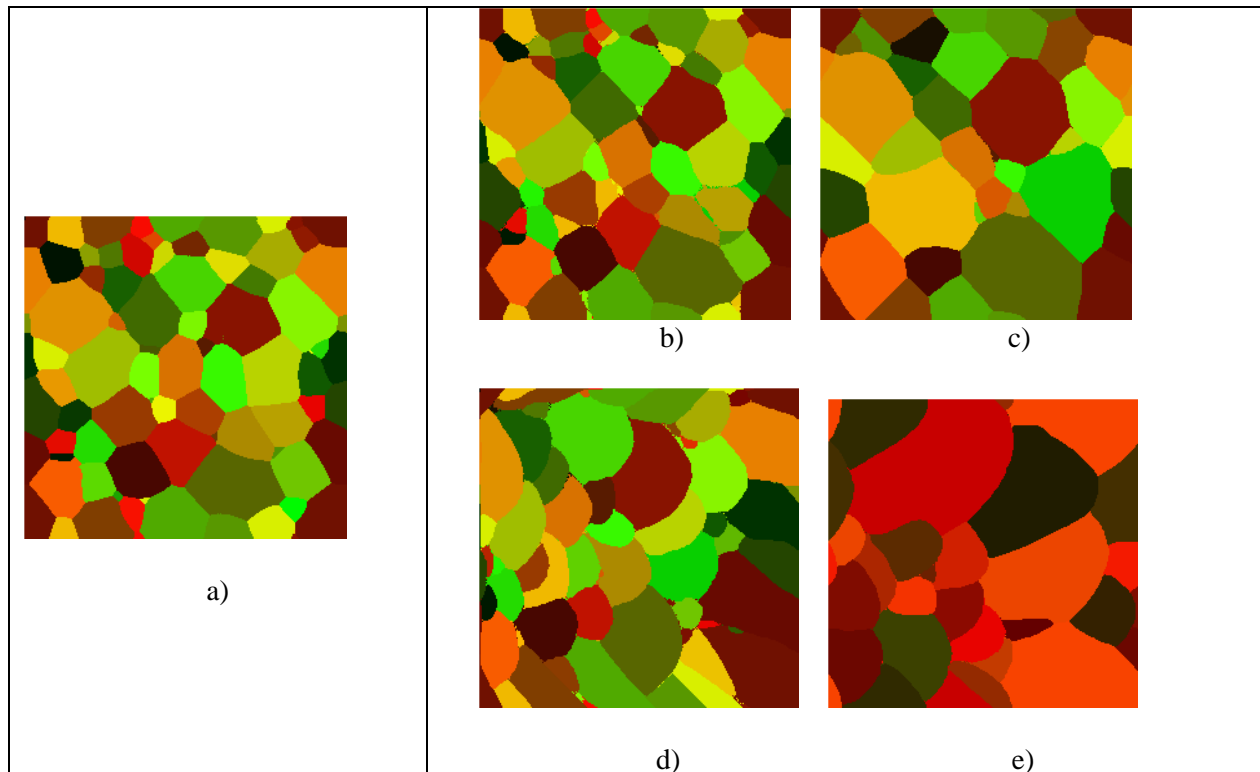


Fig.1.11. Cross-sections generated using model of normal grain growth: (a) initial microstructure; (b) with no misorientational but only GBI dependence of GB effective energy after 200MCS; and (c,d) with both misorientational and GBI dependence of GB effective energy after 200 and 800 MCS, correspondingly.

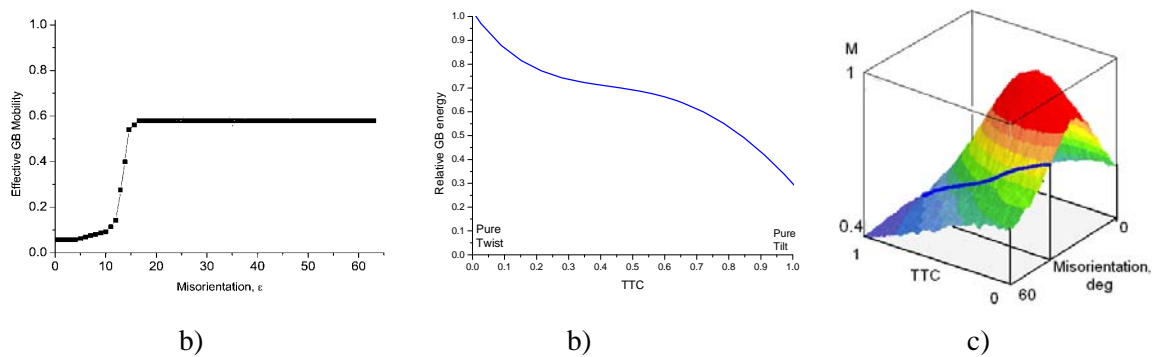


Fig.1.12. Effective GB mobility as function of scalar GB misorientation only (a); of TTC component (b) and both misorientation and TTC component (c).

1.5. MC modeling of Grain Growth with implemented GBM/GBI

To clarify the GBI effect on grain growth kinetics initial microstructure for three comparative cases (A – C) was taken as shown on Figure 1.13a. : Effective GB mobility for cases A to C was defined as:

Case **A** – GB mobility as function of GB misorientation only, no GBI influence was assumed - GBM usual assumption was used [4], i.e. low angle boundaries were assumed to perform low mobility in comparison with the high angle boundaries (Fig. 1.12a);

Case **B** – GB mobility $M = M_{GBM} * M_{GBI}$ as function of both GBM and GBI depending on tilt-twist component (TTC) averaged for 35-45 deg GB misorientation interval (Figure 1.12b).

Case **C** – the same as for the Case B, but GBI dependence of M_{GBI} was approximated with smooth

surface, presented in Figure 1.12c, based on experimental data [3].

Figure 1.13b presents grain size distribution of the modeling domain assumed for Cases A to C prior to grain growth start. The microstructure has the 1000 grains within the 250^3 MU domain; hence average initial grain size is 31MU. For nearly equiaxed grain shape dispersion of GBI distribution was relatively wide.

Modeling volumes were not textured initially; hence, the effect of GBM on GB motion for Cases A to C was the same.

As expected, predicted grain growth kinetics for the Case A is so called “normal grain growth” kinetics, for which average grain size is proportional to the square root of time (Fig. 1.14). For Cases B and C, at initial stage grain growth is slower than for Case A, due to the lower GB effective mobility.

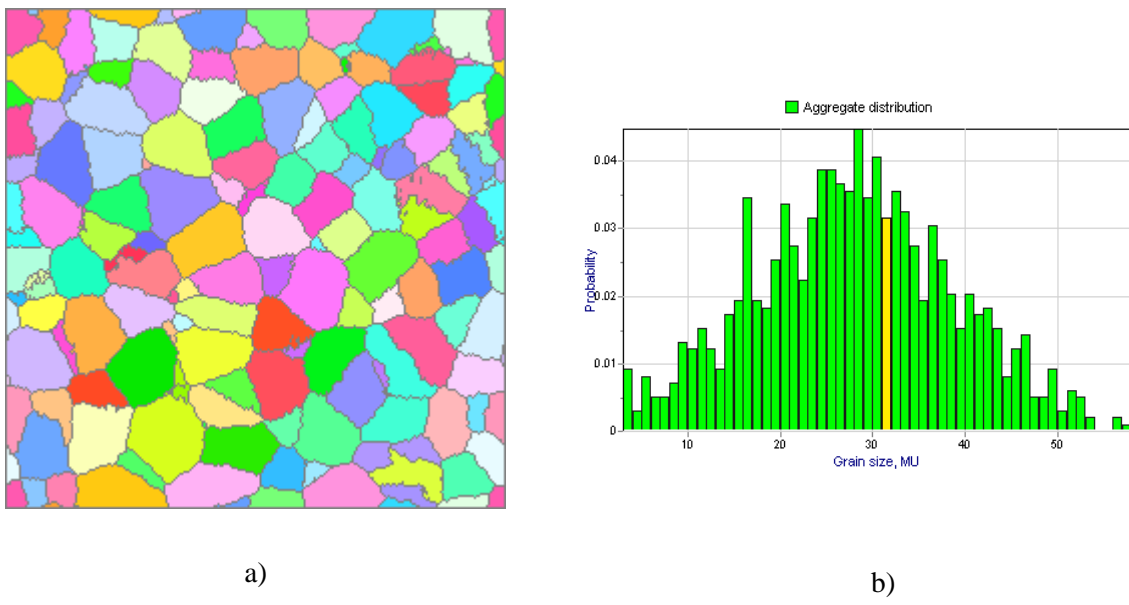


Fig.1.13. Initial microstructure (a) and initial grain size distribution (b) for Cases A to C.

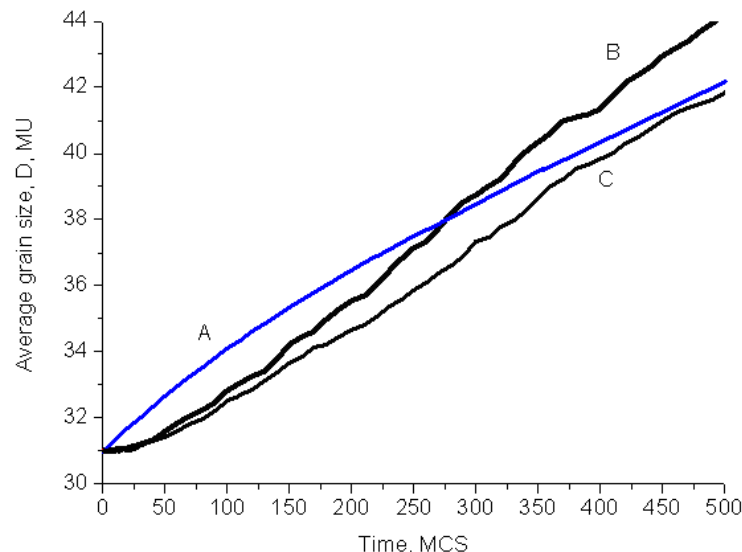


Fig. 1.14. Predicted grain growth kinetics for Cases A to C.

for boundaries with GBI varied mostly around pure tilt direction. Effect is more pronounced for the Case C. After about 100 MCS grain growth became faster for both Cases B and C due to selection of grain boundaries with high effective mobilities but then slowed again. Hence, the periodic alternating of faster and slower grain growth can be expected for longer times, as in strongly textured material [4]. It can also be seen that grain growth kinetics in the cases B and C are less “smooth”, as compared to the case A.

Initial microstructure for the Case D was formed with the same average grain size as for cases A to C, but having 1:3:3 aspect ratio (Figure 1.15a), hence it performed a relatively narrow GBI dispersion, as compared to the equiaxed microstructure (Figure 1.16). The microstructure was formed with nucleation and grain growth technique which produced initial grain size distribution as shown in Figure 4b. It takes essential time for the first several grains to vanish for the grain size distribution like on Fig. 3b. As the result, no growth of average grain size was observed for the case D (Figure 1.17). Other result was that for the material, with grain shape aspect ratio other than 1:1:1. Due to specific dispersion of GBI distribution, kinetics of grain growth in non equiaxed microstructure has proved to be much slower (Figure 1.17). It was observed that the microstructure gradually transformed into equiaxed (Figure 1.18). It can be expected that after reaching 1:1:1 aspect ratio, the kinetics of grain growth for both types of initial microstructure will follow the similar dependence, although the delay at the beginning stage of the growth will result in smaller average grain size. It should be also mentioned that some initial delay in grain growth in non-equiaxed microstructure was due to initial grain size distribution in which small grains were absent and therefore, it took some time for first grains to disappear.

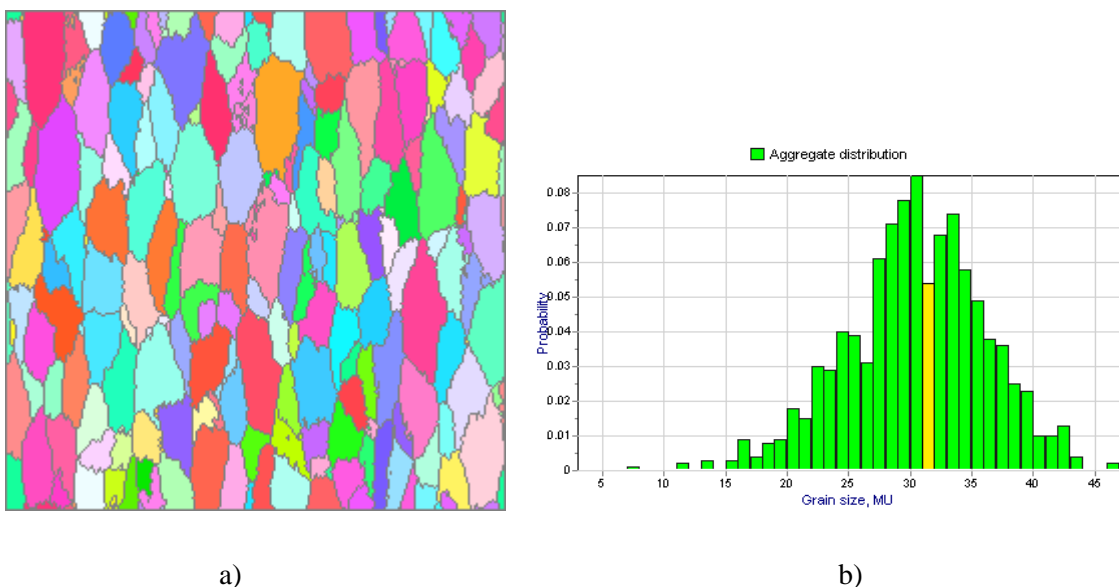


Fig.1.15. Initial microstructure (a) and grain size distribution (b) for Case D.

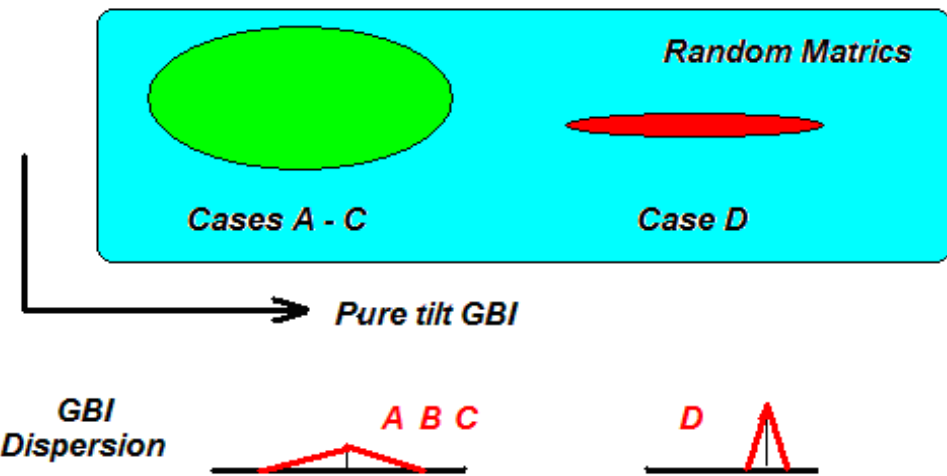


Fig. 1.16. Schematically: difference in GBI dispersion for Cases A to C and D.

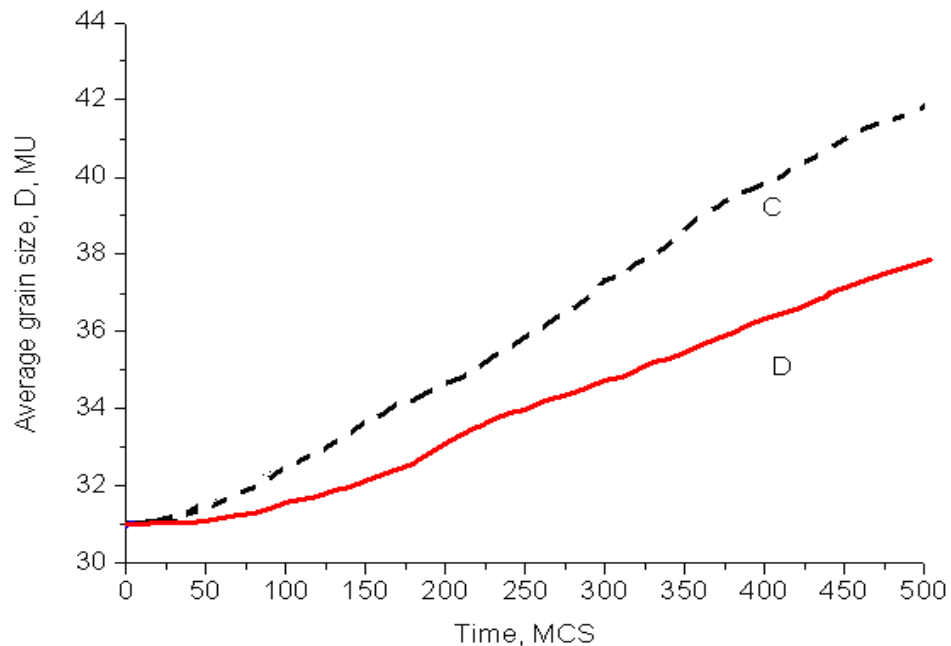


Fig. 1.17. Predicted grain growth kinetics for Case D in comparison with the Case C (dashed line).

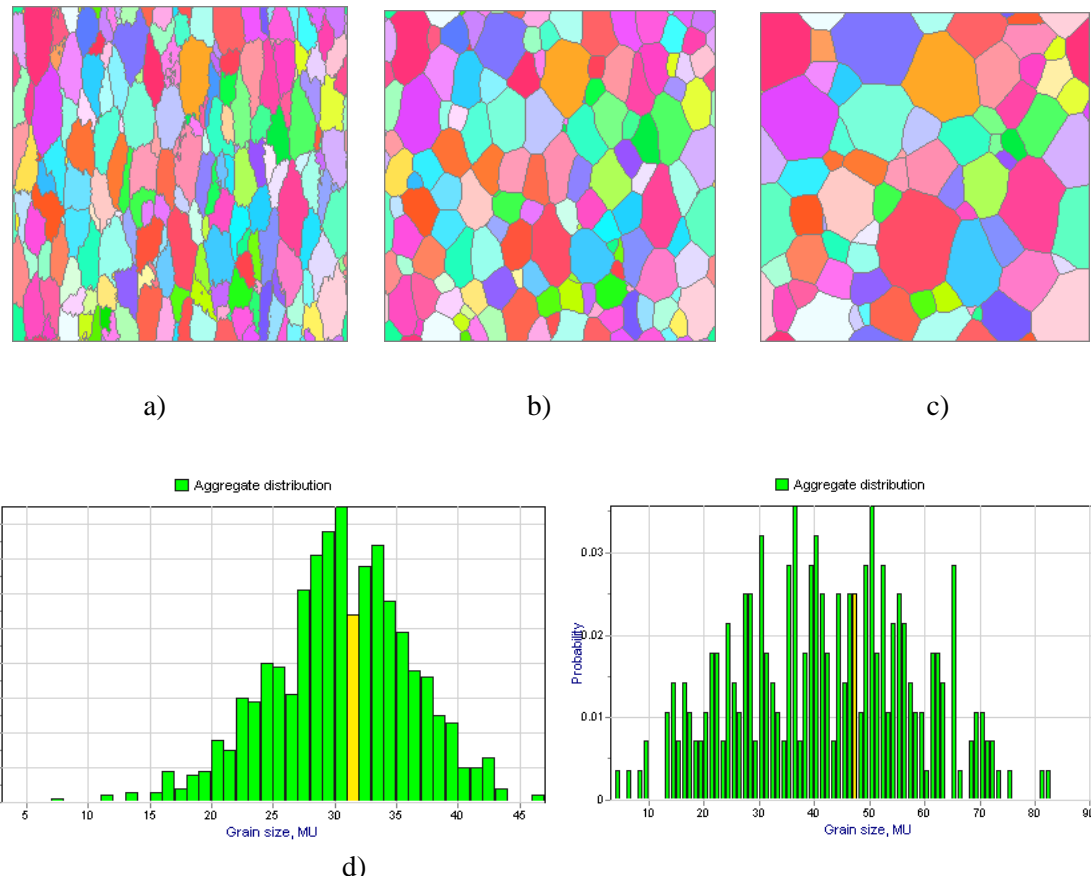


Fig. 1.18. Predicted microstructures for Case D (a) initial, after 150 MCS (b) and 500 MCS (c). (d, e). Initial (d) and predicted grain size distribution (500 MCS).

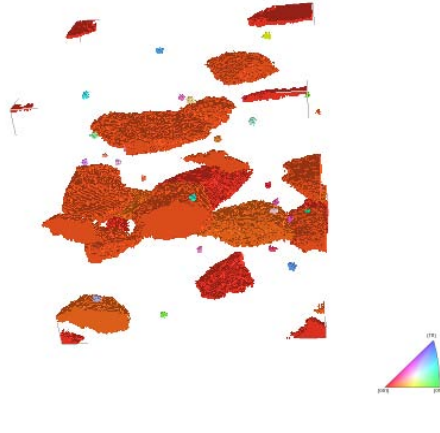
1.6. MC Modeling of Recrystallization with implemented GBM/GBI

Special modeling volume was constructed to study how implementation of GBI dependence of effective GB mobility affect recrystallization.

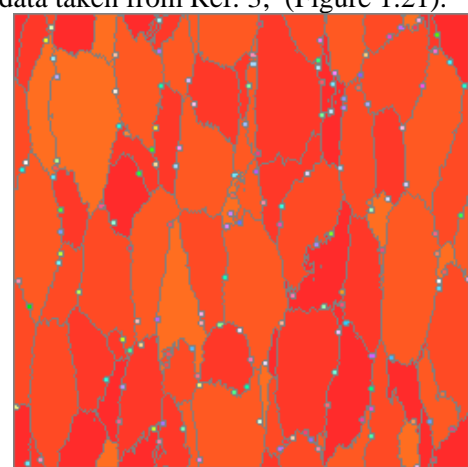
The initial as-deformed microstructure was formed with 1:3:3 aspect ratio (Figure 1.19) thus providing the narrow GBI dispersion. The model domain had a sharp, single component initial texture strong enough to obtain most grains similarly oriented. The oriented continuous nucleation of recrystallized grains was assumed. New grains were assumed to be misoriented 30 to 45 degrees to the deformed matrix, but rotation axes were randomly selected. Furthermore, it was assumed that grain boundaries were preferred sites for nucleation of recrystallized grains. The nucleation rate for each MCS within the unrecrystallized material was set as 10-4 nuclei per MU3. The recrystallization nuclei were assumed to be equiaxed with an average volume of 15 MU3.

Initial stored energy distribution is shown on Figure 1.20. Stored energy was assumed to be dense close to GBs descending to grain interior. Recrystallization front velocity was assumed to be proportional to the local stored energy density, as well as to the effective mobility. In the reference case A the GB mobility was assumed as function of GB misorientation only. Hence, GBM usual assumption was used, i.e. low angle boundaries (LABs) were assumed to perform low mobility in comparison with the high angle boundaries (HABs). In the case B, GB mobility was defined by GBM and GBI dependencies

approximated with smooth surface based on experimental data taken from Ref. 3; (Figure 1.21).



a)



b)

Fig.1.19. (a) 3D image of selected deformed grains and some rex. nuclei, and (b) cross-section (b) generated for simulation initial microstructure.

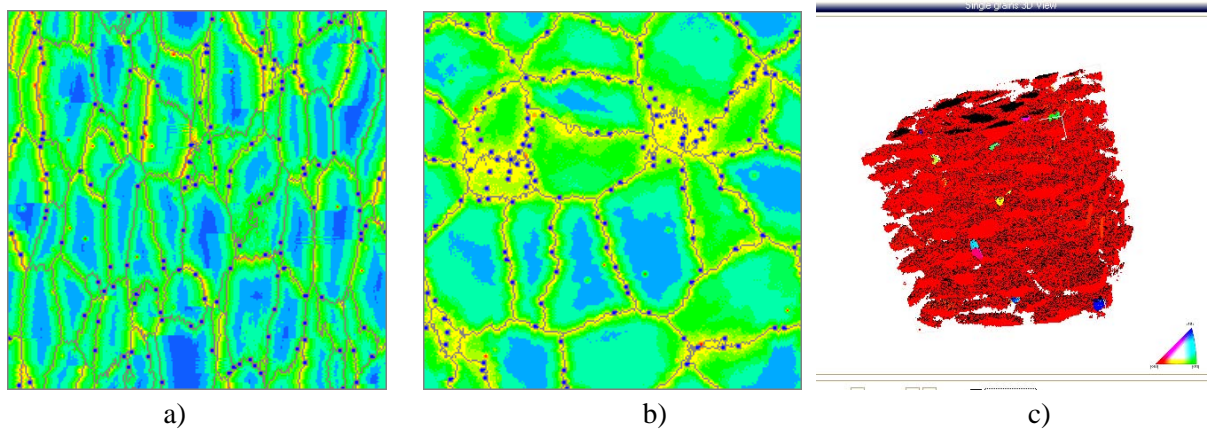


Fig.1.20. Stored energy distribution shown with color (blue to red scale) within the modeling domain. Cross-sections generated transverse plane (a) and rolling plane (b) and 3D image (c) showing some rex. nuclei and not recrystallized volume after 50 MCS (Case A).

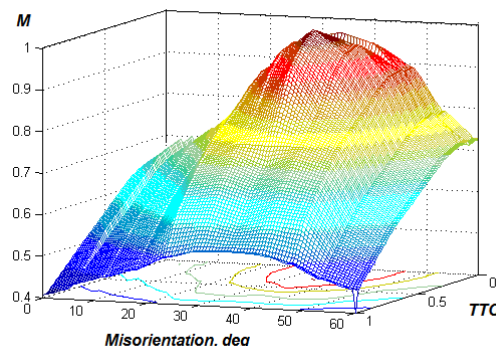


Fig.1.21. Effective GB mobility as function of both scalar GB misorientation TTC component.

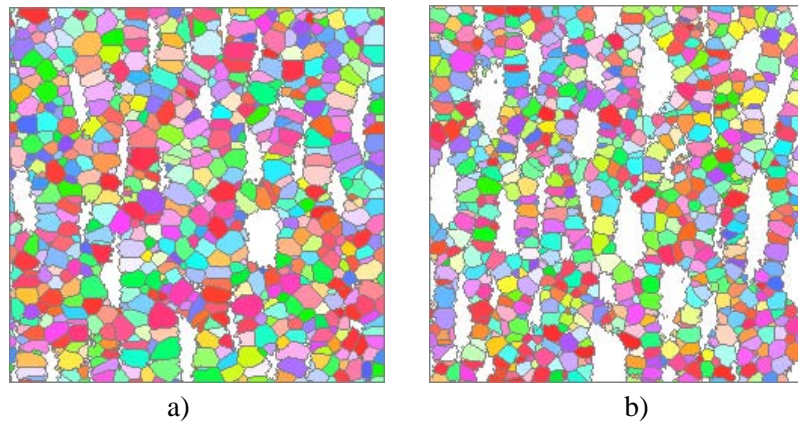


Fig. 1.22. MC predicted microstructures after 75 MCS: (a) Case A (90% rex.) and (b) Case B (80% rex.)

Microstructural changes during recrystallization for cases A and B after equal number of MCS are illustrated with Figure 1.22. For assumed recrystallization model (oriented nucleation at grain boundaries and stored energy descending from grain boundary to the centre of the deformed grain) average GBI for the recrystallization front is about the same as for the as deformed material (Figure 1.22b). The recrystallization kinetics depends on recrystallization front effective mobility. Hence it can be expected to be slower when GBI is accounted. In fact, it was shown, that taking into account GBI essentially changes recrystallization kinetics, and, in particular, time for recrystallization to complete (Figure 1.23). Figure 1.24 shows the microstructures for Cases A and B after recrystallization completes. It is clear seen that the average grain size for case B is about two times bigger than for case A (18 and 32MU correspondingly).

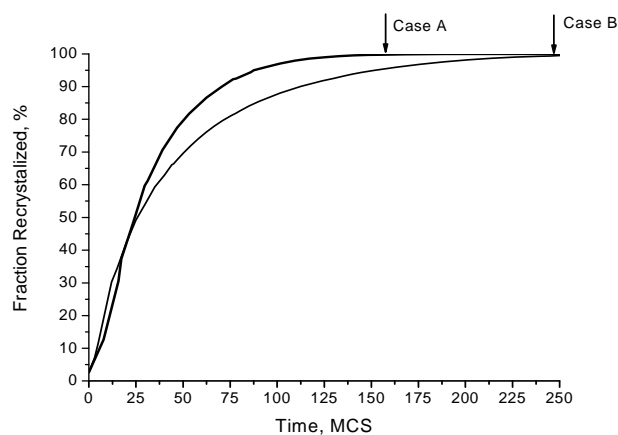


Fig. 1.23. Predicted recrystallization kinetics for Cases A and B.

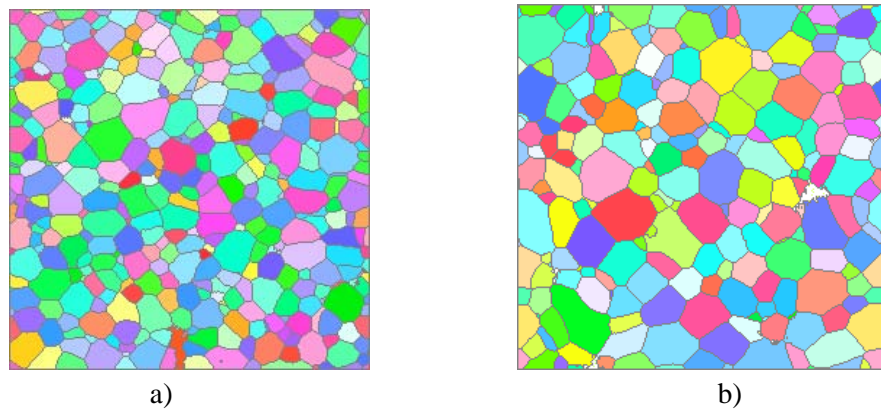


Fig. 1.24. Predicted microstructures for Cases A and B after recrystallization completes: a) Case A, 100 MCS b) Case B, 250 MCS.

2. MODELING OF INHOMOGENIOUSLY TEXTURED MATERIAL

Interface for introducing local textures into the modeling microstructure was developed. Test programs were created and run to show how the “pure” GB properties dependence on GBI affects the special model microstructure.

Basic software was the same as described in [1]. Applications described below were designed using Borland Delphi tools to run under MS Windows 2000/XP OS.

2.1 Introducing texture inhomogeneities into 3D modelling volume

Interface for introducing the spatial texture inhomogeneities was developed. Figure 2.1 illustrates the first compiled interface version; it is now possible to divide the whole modeling volume on to the number of local spatial regions, and different textures can be assigned for each spatial region. Certainly, the local textures have to match desired integral texture and GBM distribution function in the modeling volume.

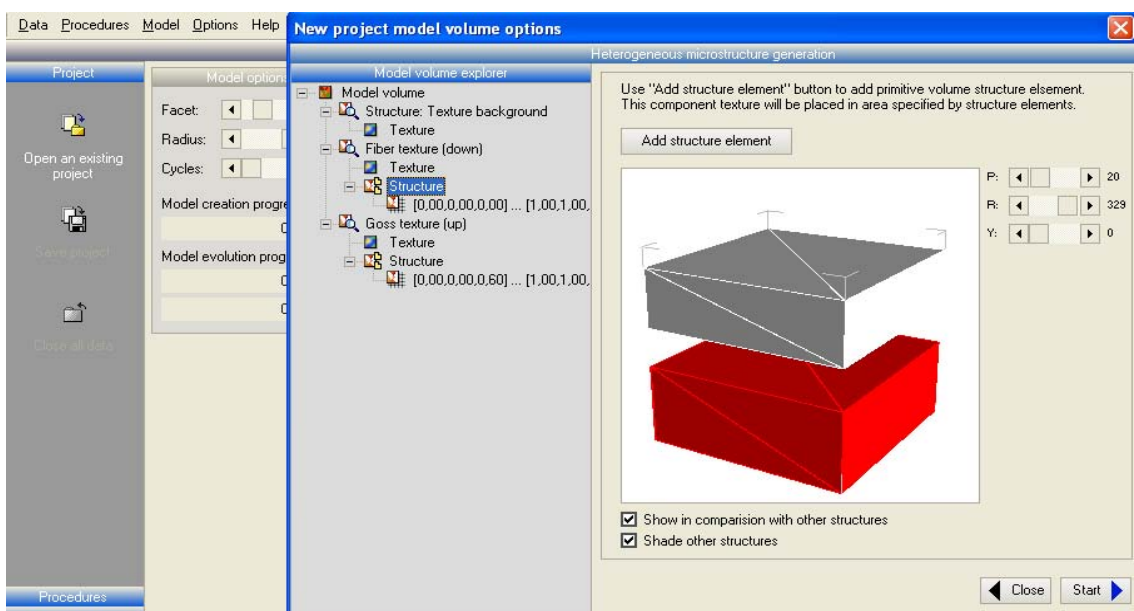


Fig.2.1. Interface for introducing the spatial texture inhomogeneities into the modeling volume.

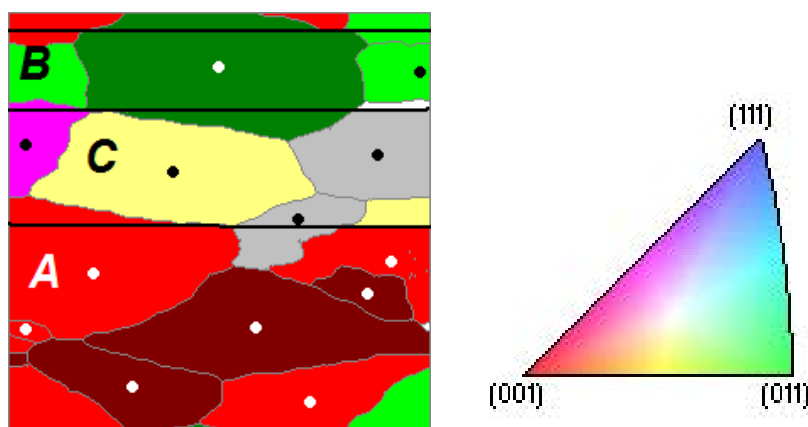


Fig. 2.2. Local textures implemented into the model of deformed material microstructure. Spatial region corresponds to the 001 fiber texture, region B is close to 011 texture component and region C random background (undefined).

To define the grain orientation with respect to the specimen (or model domain) axes, three Euler angles (φ_1 , Φ , and φ_2 in Bunge notation) were used. Specific values of the crystallographic orientation $g = \{\varphi_1, \Phi, \varphi_2\}$ ($0 \leq \varphi_1 < 360$, $0 \leq \Phi < 90$, $0 \leq \varphi_2 < 90$) were associated with each MU and presented as MU color according to color scheme as shown on Fig.2.2. The grain-boundary position was associated with the space between two sites having unlike orientations. Each grain was characterized by a volume equal to the number of MUs that comprised it. Hence, we can define the ‘grain’s center of gravity’ and, on the base of its position, make a decision which spatial region this particular grain belongs to.

A special procedure was used to create the initial textural state within each spatial region of the modeling volume (Fig. 2.2) and thus to replicate the specified ODF for each region as closely as possible. This procedure was based on the following probabilistic function:

$$P(\Omega_j) = \frac{1}{V_{MD}} \frac{1}{N_g(\Omega_j)} \sum_{MD} V(G_i) \chi(g(G_i))$$

$$\chi(g(G_i)) = \begin{cases} 1, & g(G_i) \in \Omega_j \\ 0, & g(G_i) \notin \Omega_j \end{cases},$$

in which $g(G_i)$ is the orientation of the i -th MU, $V(G_i)$ is the number of MUs oriented as $g(G_i)$, N_g is the total number of orientations g within the volume Ω_j , and V_{MD} is volume of the overall model domain. From tests on model textures, it was determined that this procedure did not work well when the number of grains in the local zone was less than 50, but gave very good results when there were 100 or more grains.

Interface for introducing the spatial texture inhomogeneities was used for creation of initial modelin volumes with several differently textured bands. To show that interface together with correspondind program code can be used to simulate the role of scale factors, such as local texture band width (BW) & subgrain size (SBG), in microstructure evolution, volumes with two essentially different subgrain sizes we created.

2.2. MC modeling with texture inhomogeneities in 3D (accounting GBM only).

Figure 2.3 illustrates the technique of initial modeling volume creation using the current interfac version; it is possible to divide the whole modeling volume on to the number of local spatial regions, an different textures can be assigned for each spatial region. Adjusting the volumes and shapes of the locall textured areas is the way to match desired integral texture and GBM distribution function in the modelin volume.

Cross sections of initial modeling volumes, having BW/SBG ratio 10 and 4, are presented on figure 2. Figures 2.5 and 2.6 presents the temporal evolution predicted by MC simulation for both cases, the GBI and GBI dependencies were the same as used for normal grain growth simulation.

On figures 2.3 to 2.6 different colors/grayscale levels were used for different grain orientations, henc spatial texturing is clearly seen.

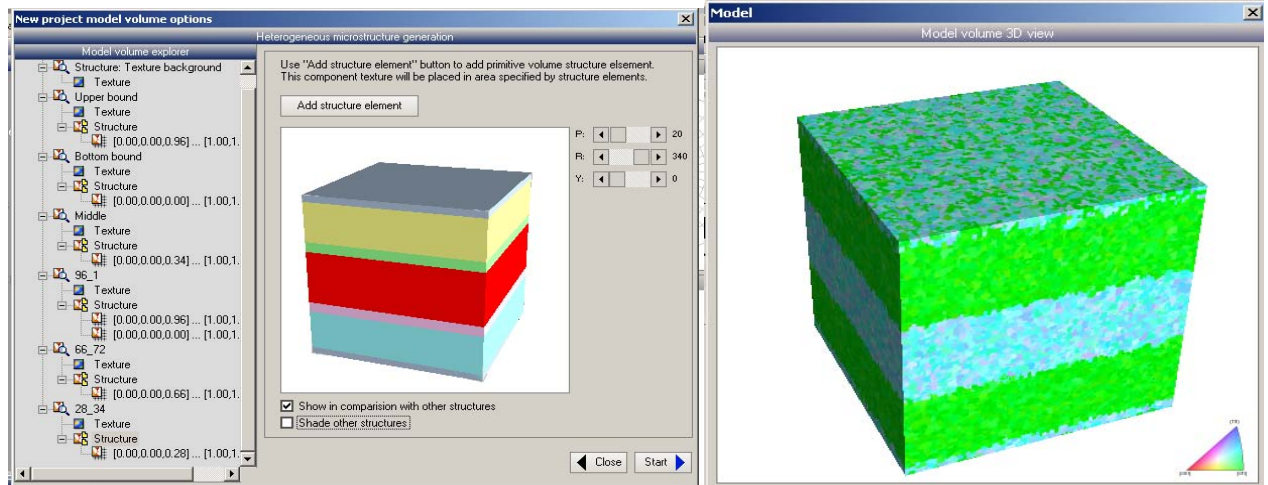


Fig. 2.3. Local textures implemented into the model of material microstructure, with bands consisting from small subgrains of low misorientation.

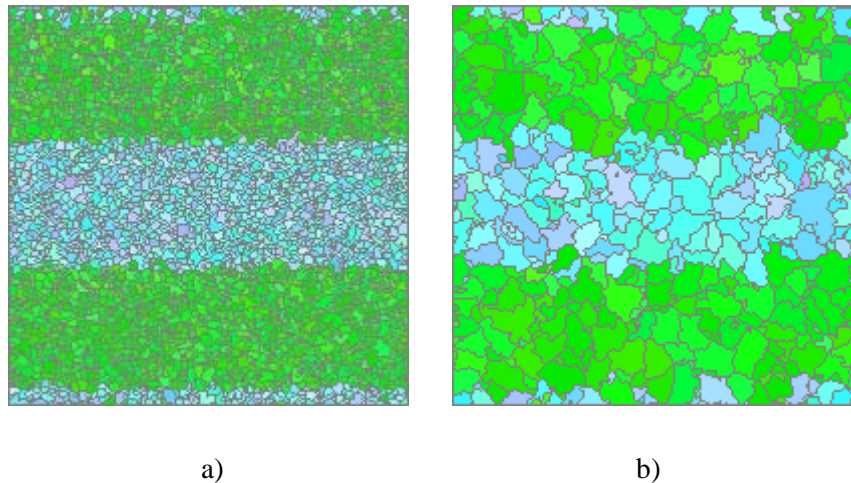


Fig. 2.4. Cross sections of locally textured initial modeling volumes: (a) and (b) BW/SBG ratio is 10 and 4 respectively.

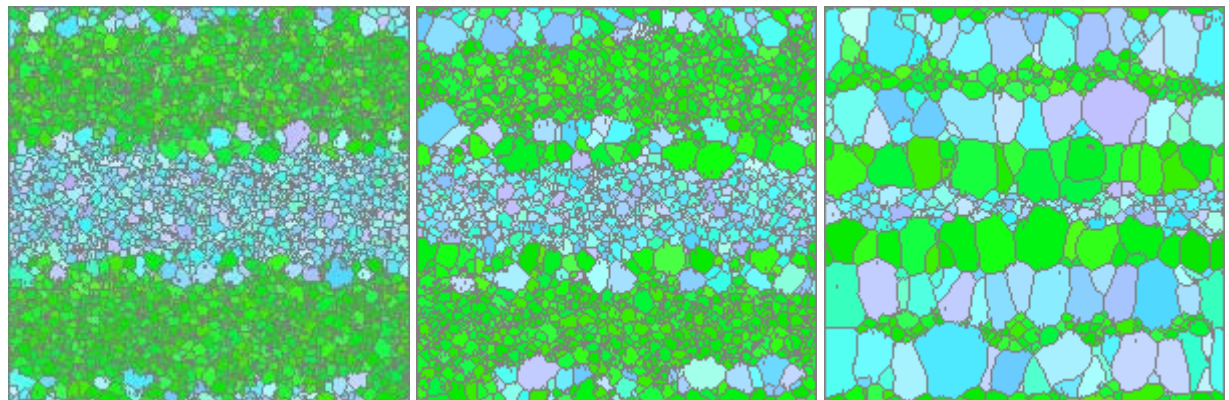


Fig. 2.5. Growth of large grains at textured band boundaries, as predicted by MC modeling for BW/SBG = 10 case, after: (a) 10 MCS; (b) 20 MCS; (c) 50 MCS. Slow growth of subgrains within the bands also occurs.

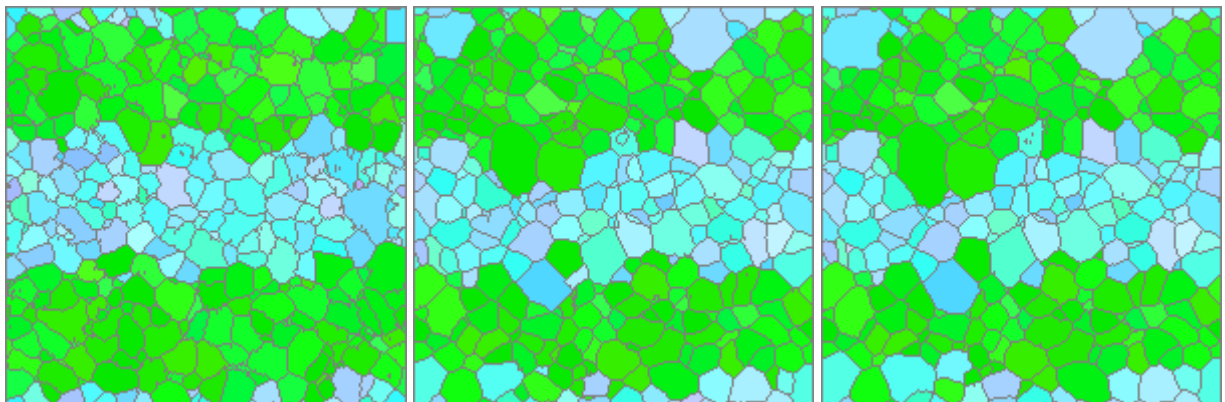


Fig. 2.6. Growth of grains as predicted by MC modeling for $BW/SBG = 4$ case, after: (a) 30 MCS; (b) 100 MCS; (c) 150 MCS.

Essential differences in grain growth rate and final microstructures were predicted for these two cases. Hence, it can be concluded that program code for MC simulation of recrystallization and grain growth is a suitable tool for studying how scale factors, such as local texture band width to subgrain size ratio, affect final microstructures.

2.3. MC Modeling with implemented GBM/GBI (Grain Growth, spatially inhomogeneous texture)

The effect of grain boundary mobility anisotropy, caused by GBI, on grain growth kinetics was shown by comparison of grain structure evolution within two parts of the modeling volume having different sharp one component textures in the initial condition. For such modeling volume each part initially was characterized with narrow GBI distributions around two different GB inclinations.

The initial microstructure was formed with 1:5:5 aspect ratio (Figure 2.7b) thus providing the narrow GBI dispersion, around the plane, indicated on Fig. 2.7a. The model domain had a sharp, double component initial texture (Fig. 2.8) strong enough to obtain most grains similarly oriented. Microstructure of modeling domain was uniform, but texture components were spatially separated and form locally textured zones (A) and (B). GB mobility was defined by GBM and GBI dependence approximated with smooth surface based on experimental data taken from Ref. 3 (Figure 2.9). Figure 2.9 also demonstrates how different GBI in A and B zones result in different effective mobilities for nearly flat LABs within the zones. The interface between A and B zones formed by HABs with relatively high effective mobility.

Predicted evolution of the modeling volume is presented on Fig. 2.10. It is obvious, that due to lower effective mobility within the B zone, grains within this area are growing slower than within the A zone. Grains aspect ratio decreases with time in both zones (but slower in zone B). As the result, the GBI dispersion increases, i.e. the difference between effective GB mobilities within the A and B zones decreases. After 200 MCS both zones perform grain growth kinetics close to normal grain growth. However, grains within the A zone are bigger; as a result, grains of zone B are gradually consumed by zone A grains and, finally, zone B vanishes.

Hence, it was demonstrated essentially different grain growth kinetics for the differently textured

areas within the modeling volume being originated due to GBI effect.

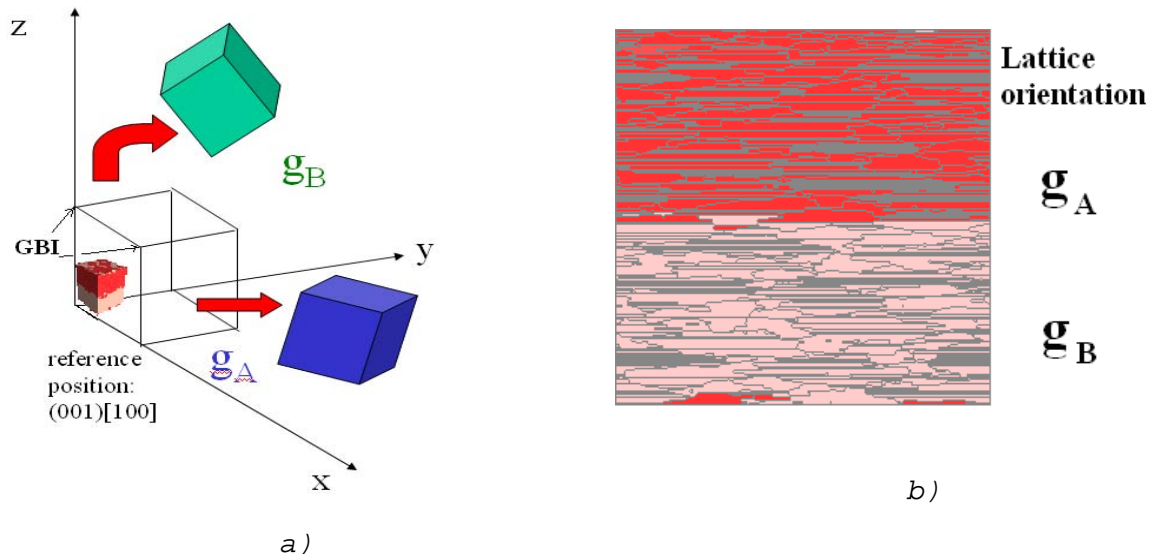


Fig.2.7. Two bcc lattice orientations within the modeling volume and major GB orientation within the modeling volume (most probable GBI) (a), and (b) initial microstructure (cross-section) for modeling volume.

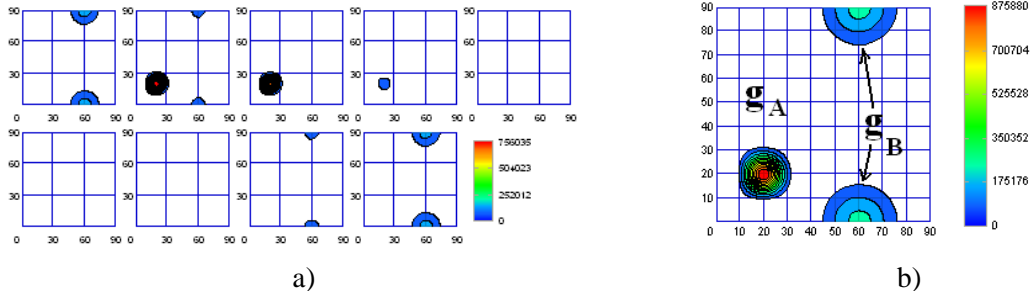


Fig.2.8. Modeling domain initial texture ODF; (a) (intensities in MU per angular unit) and (b) ODF projection indicating texture components.

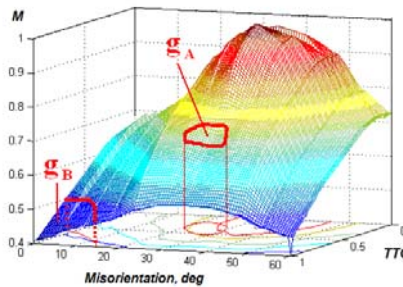


Fig.2.9. Effective GB mobility as function of both scalar GB misorientation TTC component and its relation with modeling volume texture components (A) and (B) (schematically).

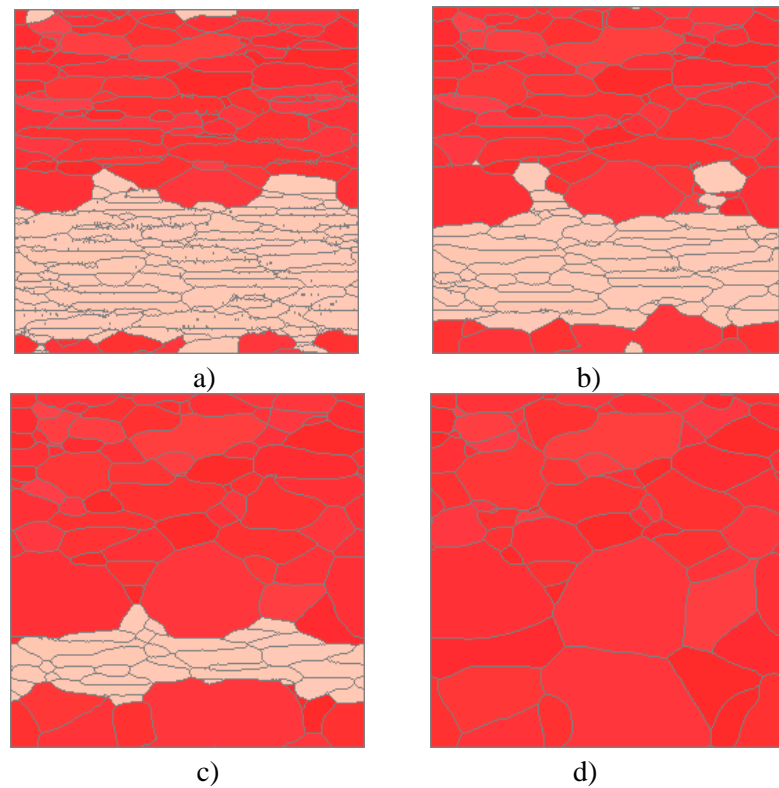


Fig. 2.10. MC predicted microstructures after (a) 75 MCS; (b) 200 MCS; c) 400 MCS; and d) 800 MCS

3. MD ESTIMATION OF RELATIVE GB ENERGIES

It was proposed in the project to use advanced MD simulation as a source of the data on grain boundary energy. A MD simulation includes selection of numerical integration scheme and employment of appropriate boundary conditions. The modeling domain in 3D with periodic boundary conditions and max. total number of atoms of about 10^5 - 10^6 was utilized. Usage of a large modeling domain makes the cell shape restriction less important compared to a small systems with a few hundred atoms.

Starting from the simple cases of tilt and rotation boundaries for which similar calculations have already been done by other authors, a number of grain boundaries with arbitrary GBI and GBM were studied.

MD applications and code developed were designed using Borland Delphi tools to run under MS Windows 2000/XP OS. MD simulation utilizes Born-Myer and Lennard-Jones type potentials with rigid boundary conditions, to reproduce differently misoriented bicrystal with different GBIs. GB relaxation was assumed to occur in two stages – sliding (lattice translation in GB plane and along GB plane normal direction) and, finally, relaxation process for each individual atom.

For lattice visualization the VMD code [6] was used (as a freeware).

3.1. Testing of cubic and spherical modeling domains.

First runs of molecular dynamic routines were aimed at forming of bicrystals of desired GMB and GBI in both cubic and spherical modeling domains. As the first step, stable lattices were obtained with using the simple Born-Mayer potential. Figure 3.1 illustrates the modeled bicrystals with GB misorientation 0, 10 and 20 degrees obtained by simple tilt.

Figure 3.2 shows bicrystals with two different GBI (0 and 90 deg tilt) and modeled by using the spherical modeling domain. Utilizing the spherical modeling domain insures that domain boundary conditions affect GB energy in the same manner (not depending on GBI) – what is essential for the GB energy calculating routines.

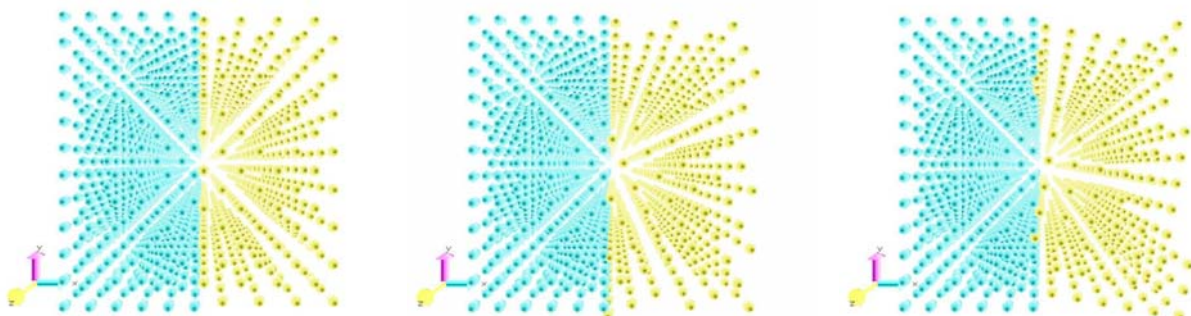


Fig. 3.1. Cubic MD modeling domain of 2300 atoms with two lattices in different misorientations.

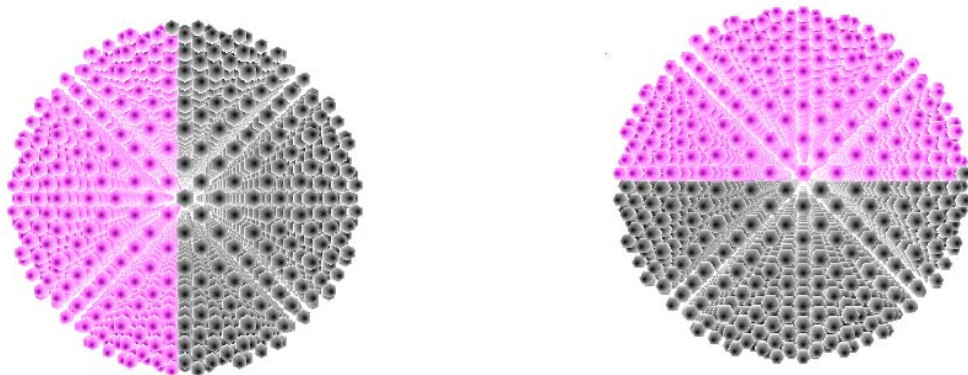


Fig. 3.2. Spherical MD modeling domain of 1650 atoms with two lattices in different misorientations and inclinations.

First test run of the MD model for GB energy estimation was performed using 3D atomistic model for GB (Fig. 3.2). The potential energy for the i -th atom was calculated using Lennard-Jones potential:

$$\phi_i = 4\epsilon \sum_{j \neq i} \{(\sigma/r_{ij})^{12} - (\sigma/r_{ij})^6\},$$

where ϵ and σ are the material parameters, and r_{ij} is the distance between the i -th and the j -th atoms. The GB bulk energy is defined as

$$\phi_{gb} = \sum_{i \in V} (\phi_i - \phi_0) / S_{gb},$$

where S_{gb} is the area of the GB, and the summation is done for all atoms in the domain V . Domain V is chosen around the GB, excluding the outer surfaces of the modeling volume.

Next parameters were used for test simulation: $\sigma = 0.22$ nm, $\epsilon = 0.08$ eV, which correspond to lattice parameter $a = 0.28665$ nm and elastic modules $C_{11} = 230$ GPa, $C_{12} = 135$ GPa and $C_{44} = 117$ GPa [7] to mimic interatomic potential used in [8] for bcc iron (Figure 3.3).

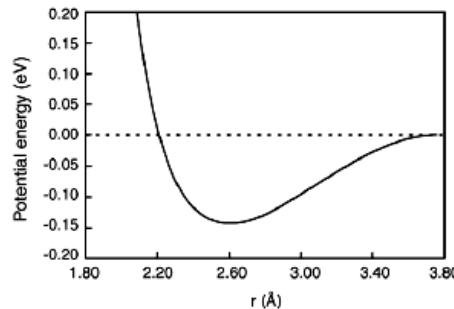


Fig. 3.3. Simple pair interatomic potential and STGB geometry assumed for test MD run.

GB energy estimation was done for symmetric tilt [100] GB (STGB) (Figure 3.4) with misorientation from 0 to 90 deg, with angular step of 2 deg. GB estimation was done for “relaxed” grain boundaries, i.e. GBs with minimal free energy for given crystallographic parameters. Relaxation procedure included 3 stages: a) generating two lattices in given misorientation within the same modeling volume; b) rigid relaxation, i.e. mutual shift of lattices to find the position with minimal GB energy, and c) individual atom relaxation which form stable GB structure (Figure 3.5). Last stage was realized with usual MC procedure – randomly selected atom was allowed to move for small finite distance towards energetically preferred position; then procedure repeated until GB energy reached its minimum.

Calculated relaxed STGB energies are presented on Fig 3.6. using the relative values between 0 (monocrystal) and 1.

As it seen, calculated energies of special boundaries are generally lower what can accepted as a proof the adequacy of the calculation procedure, developed in this project. The results for this particular case well correspond to the results of Ref. [9] (Figures 3.6 and 3.7). But contrary Ref. [8] and other similar publications, our approach allows to calculate energy of not only tilt or twist boundaries but as we suppose, it can be used for any type of the boundary.

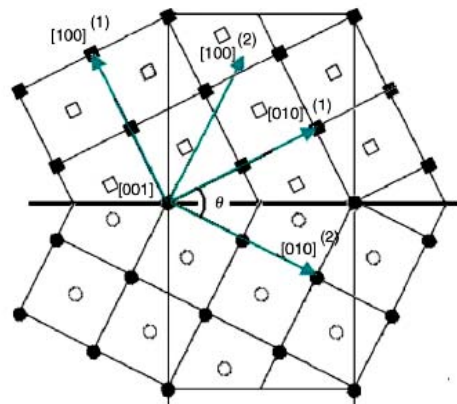


Fig. 3.4. Geometry of the [100] STGB, projection on (001) plane (not relaxed).

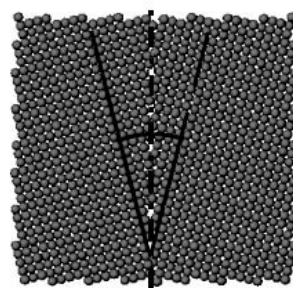


Fig. 3.5. [100] STGB model (relaxed).

Additionally, GB energies of special grain boundaries (Table 3.1) were calculated.

Table 3.1.

GB plane	Misorientation, deg	Σ	Minimum relative GB energy
210	53.13	5	0.242
310	36.87	5	0.250
320	67.38	13	0.382
510	22.69	13	0.653
530	61.93	17	0.425
410	28.07	17	0.651

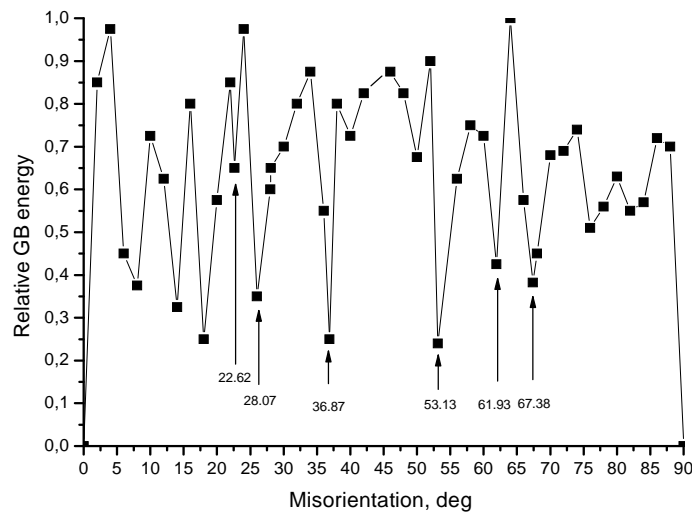


Fig. 3.6. Relative STGB [100] energy as function of misorientation, MD simulation.

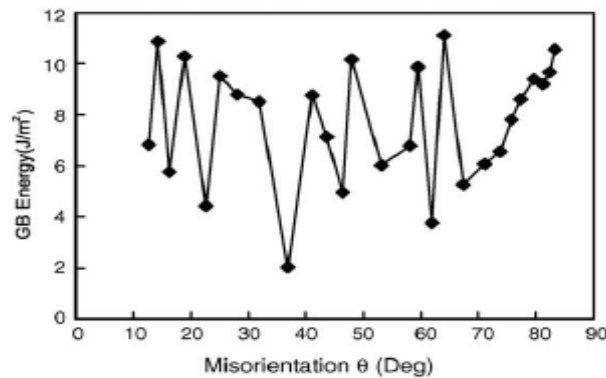


Fig. 3.7. Result for bcc STGB [100] obtained in [8].

Good correspondence obtained with previous results for bcc STGB [100], obtained with analytical embedded atom method [8], in particular, low relative energies for several special GBs.

3.2. Grain boundary energy as function of GBM.

Using preliminary results on MD modeling (see above 3.1 section) two runs of the MD model for GB energy estimation were performed using 3D spherical atomistic model for GB. Significantly bigger than previously modeling volume was used (200^3 atoms). The first run was the case of generally misoriented GB and the second one was to estimate GBI dependence for GB of certain misorientantstion.

GB energy estimation was done for general non symmetric GB (Figure 3.8) with misorientation $(30, \Theta, 30)$ when Θ is changing from 0 to 90 deg, with angular step of 1 deg (another grain has $(0, 0, 0)$ orientation). GB estimation was done for “relaxed” grain boundaries, i.e. GBs with minimal free energy for given crystallographic parameters.

As it is seen, calculated energies of special boundaries are generally lower what can be accepted as a proof the adequacy of the calculation procedure. Although, relatively high modeling volume was used in simulation, there was no correlation between the coincide lattice period Σ and minimums depth in GB energy (Figure 3.9). This might be because of the rather big angular step of 1 deg, which special boundaries are not correctly defined.

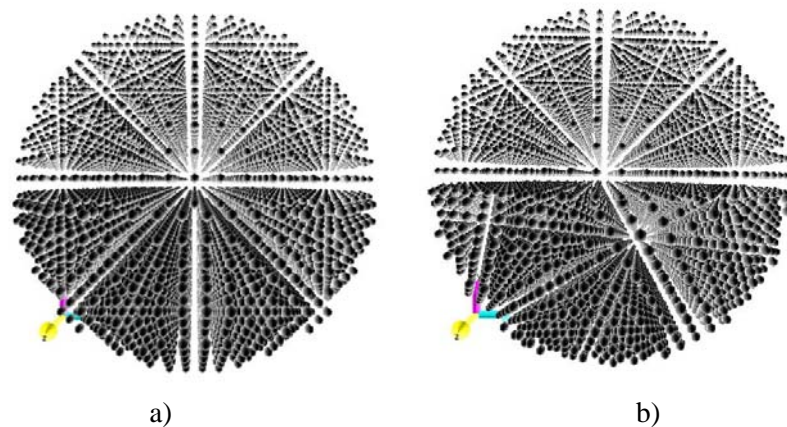


Fig. 3.8. Geometry of the simulated GB (central horizontal plane) with misorientation (a) $(30, 90, 30)$ and, (b) $(30, 19, 30)$, central part of the modeling volume.

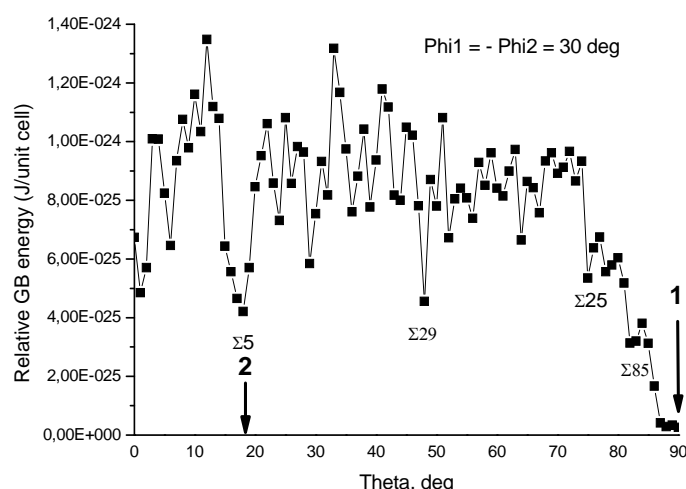


Fig. 3.9. GB energy for $(30, \Theta, 30)$, $\Theta = [0, 90]$ boundary. Positions 1 and 2 correspond to atomic structures (a) and (b), respectively, Fig. 3.8.

3.3. Grain boundary energy as function of GBI.

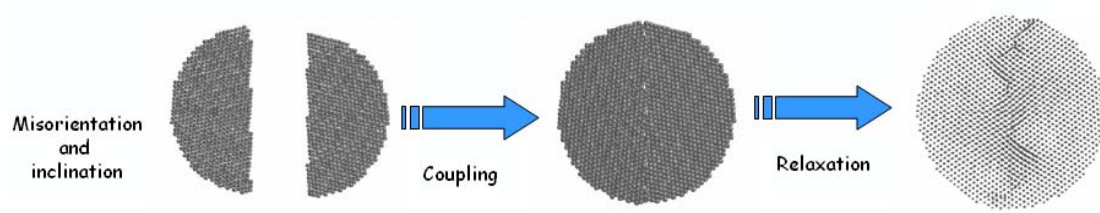


Fig. 3.10. Introducing GBI into GB energy estimation procedure.

Proposed 3D MD approach allows calculating the GBI dependence of GB energy at certain GBM. Schematically the routine is presented on Fig. 3.10. As an example, the calculation was performed for bcc lattice with (30, 0, 30) (0,0,0) misorientation.

Much higher GB energies for GBI oriented along the high symmetry lattice directions and as compared to other GBIs was demonstrated (Figure 3.11a). If this special GBI value is excluded, the variation of GB energy for a given GBM was found to be not very significant (Figure 3.11b). This result is in good correlation with data on effective interplanar spacing vs GBI dependencies [7, 9].

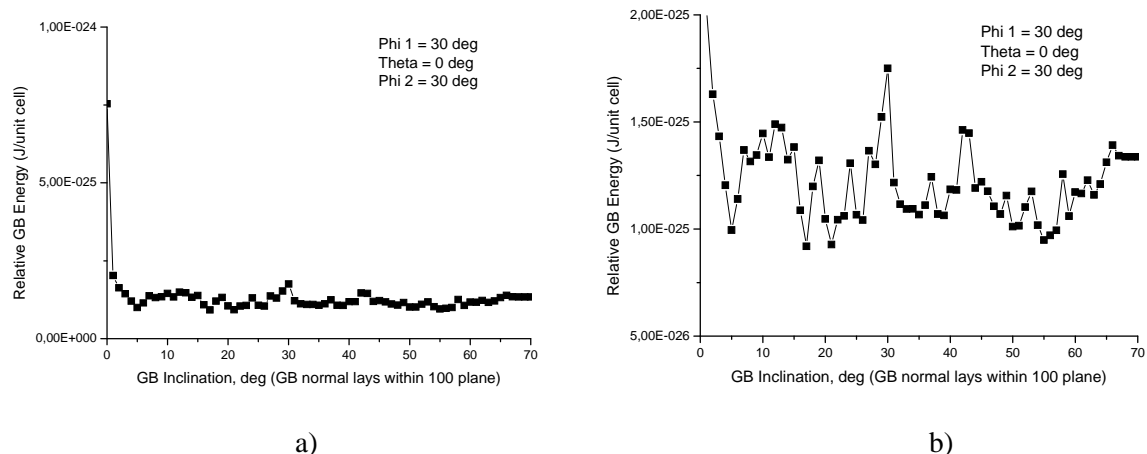


Fig. 3.11. GB energy for (30, 0, 30) (0,0,0) misorientation; GBI = [0 to 70] deg. (a) all data and (b) – points for 0 and 1 deg GBI are excluded.

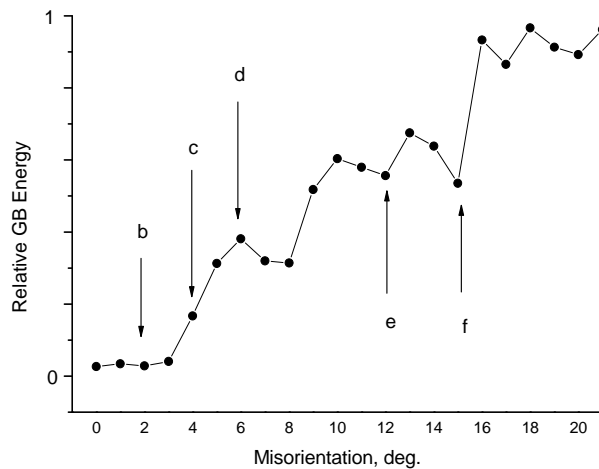


Fig. 3.12. Relative GB energy for (45, Theta, 45), Theta = [0, 20] boundary. Marked positions correspond to CLS patterns presented on Fig.3.14

Figure 3.12 presents GB energy estimation for general type type non symmetric GB, for (45, Θ , 45) (0, 0, 0) misorientation and GBI parallel to 100 plane of bottom part of bicrystal, when Θ is changing from 0 to 20 deg, with angular step of 1 deg. It is clearly seen, by comparison with corresponding CLS patterns (Fig. 3.14) that transition from LABs to HABs occurs through decreasing an area of nearly coherent patterns. This results in more dislocations and, finally, in forming HAB within the relaxed GB.

Full symmetric twist sequence of this GBs family is presented on Figure 3.13.

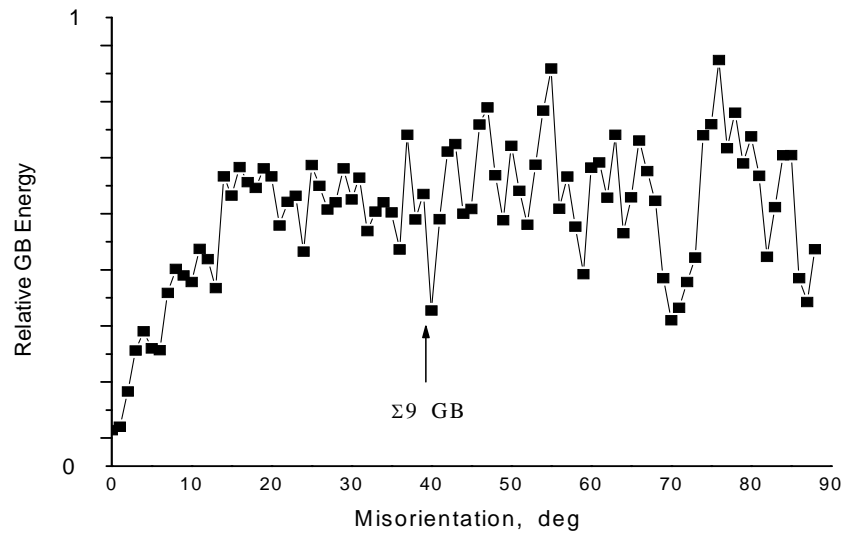


Fig. 3.13. Relative GB energy for (45, Theta, 45), Theta = [0, 90] boundary. Marked position corresponds to $\Sigma 9$ CLS GB.

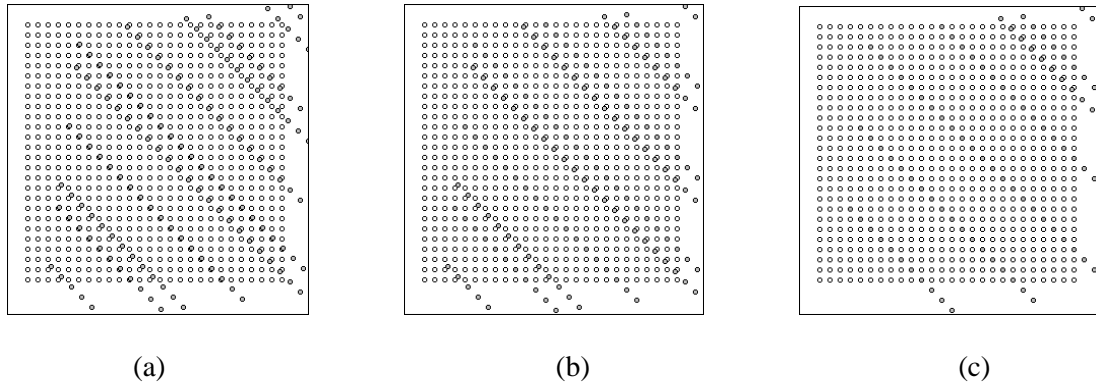


Fig.3.14. GB for (45, Theta, 45) (0, 0, 0) CLS visualization: Theta = (a) 34.6 (b) 38.6 and 38.8 (c) deg.

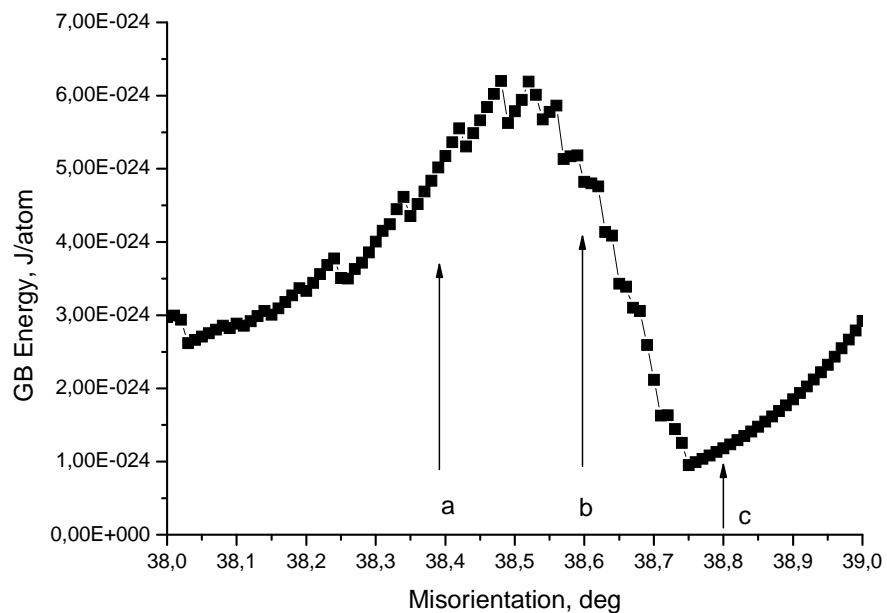
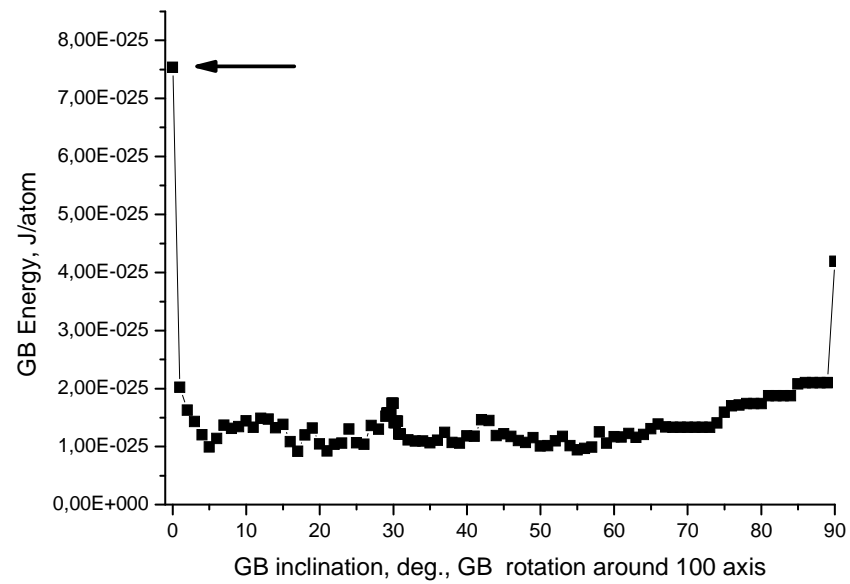


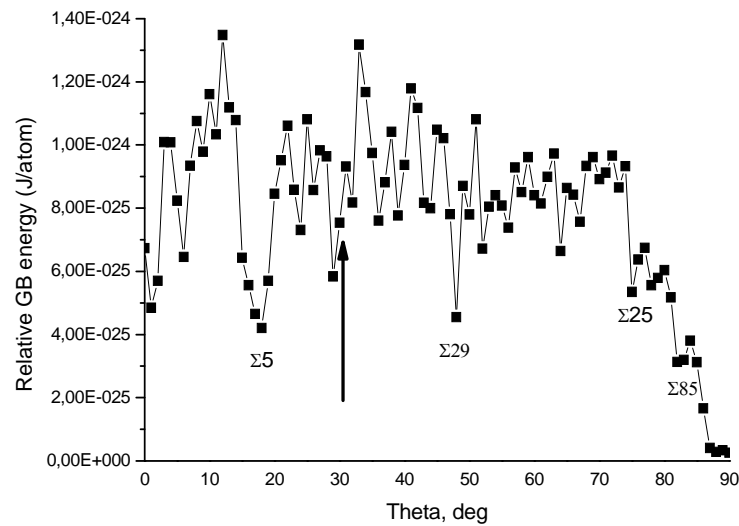
Fig 3.15. GB energy for (45, Theta, 45), Theta = [38, 39] boundary. Position. (c) corresponds to $\Sigma 9$ CLS GB.

As it is seen from Figures 3.13 and 3.15, according to MD simulations, the closest to $\Sigma 9$ CLS grain boundary lays between 38.7 and 38.8 degrees. It should be noted here, than when we were trying to examine smaller angular steps, no father details were seen on graph (Fig. 3.15), obviously due to the finite size of the modeling volume.

Additionally, it was demonstrated how relative GB energy is changing with variation of GBI (Figure 3.16). It was concluded from results presented on Figure 3.16 that almost all inclined GBs had 3 to 7 times less energies, that not inclined ones, i.e. inclined GBs are “better relaxed”. However, difference in GB energy for different inclinations isn’t so essential. It was shown also that in the case of special misorientations like that presented on Fig. 3.17, inclination does not change the boundary energy as compared to that noticed.



(a)



(b)

Fig. 3.16. GB energy as function of GBI. GB misorientation (30, 30, 30) (0,0,0) (a). Not inclined GB position is shown by bold arrow on the GB energy misorientation dependence (b).

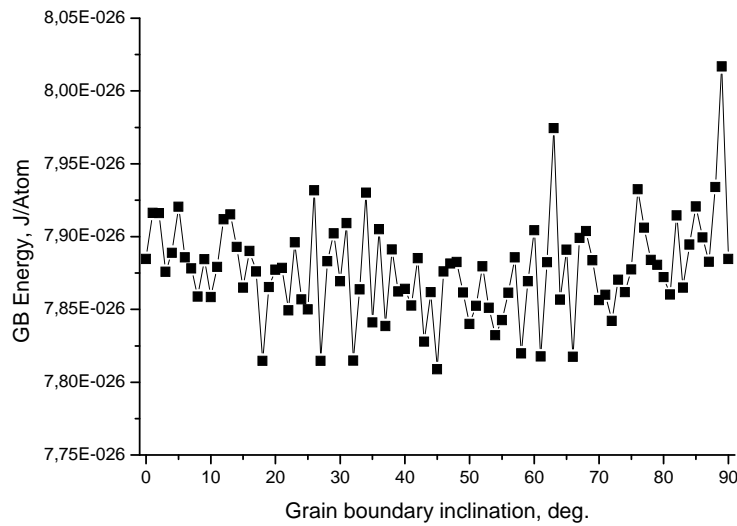


Fig. 3.17. GB energy as function of GBI. GB misorientation (45, 0, 0) (0,0,0), rotation around 100 axis.

3.4. Relative GB energy dependencies on GBI and GBM. 2D maps.

Using advanced MD modeling software (see above sections 3.1-3.3) investigation of GB energies as functions of GBM and GBI was being continued for bcc bicrystal *for general case of not special GB geometry*. For further MD and MC simulations unified notification considered introduced, based on the Cartesian axis, coincided with 100, 010, and 001 directions in one the neighboring grains (the only exception will be global texture, based on the sample's or modeling domain coordinate system). GBI was defined with GB normal's angles ω and ϕ (see Fig.3.18).

As starting point, GB energy was calculated for (0, 0, 0) (20, 20, 20) GBM and GBI parallel to 100 plane of part of bicrystal with orientation (0,0,0).

Using above misorientation, map for relative grain boundary energy as function of GBI, (normal to GBI direction defined with ϕ and ω angles) using angular step of 2 deg both for ϕ and ω (about 2000 points) was built (Fig.3.19).

Figure 3.19 presents relative GB energy estimation for general type HAB, for $\phi \in [0, 90]$ and $\omega \in [0, 90]$ angular intervals. For comparison of 2D map with actual data relative GB energy along A-B and C-D sections were plotted (Figure 3.20).

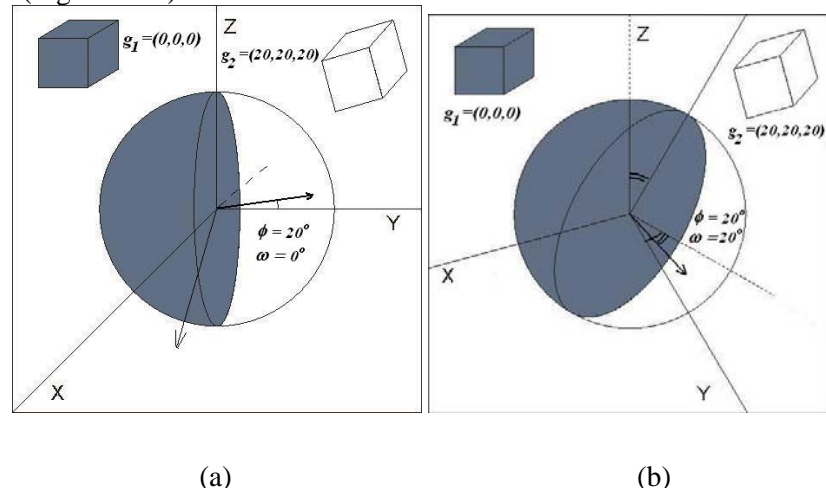


Fig.3.18 GB inclination for (0,0,0)(20,20,20): GBM (a) $\omega = 0$ deg, $\phi = 20$ deg; (b) $\omega = 20$ deg, $\phi = 20$ deg.

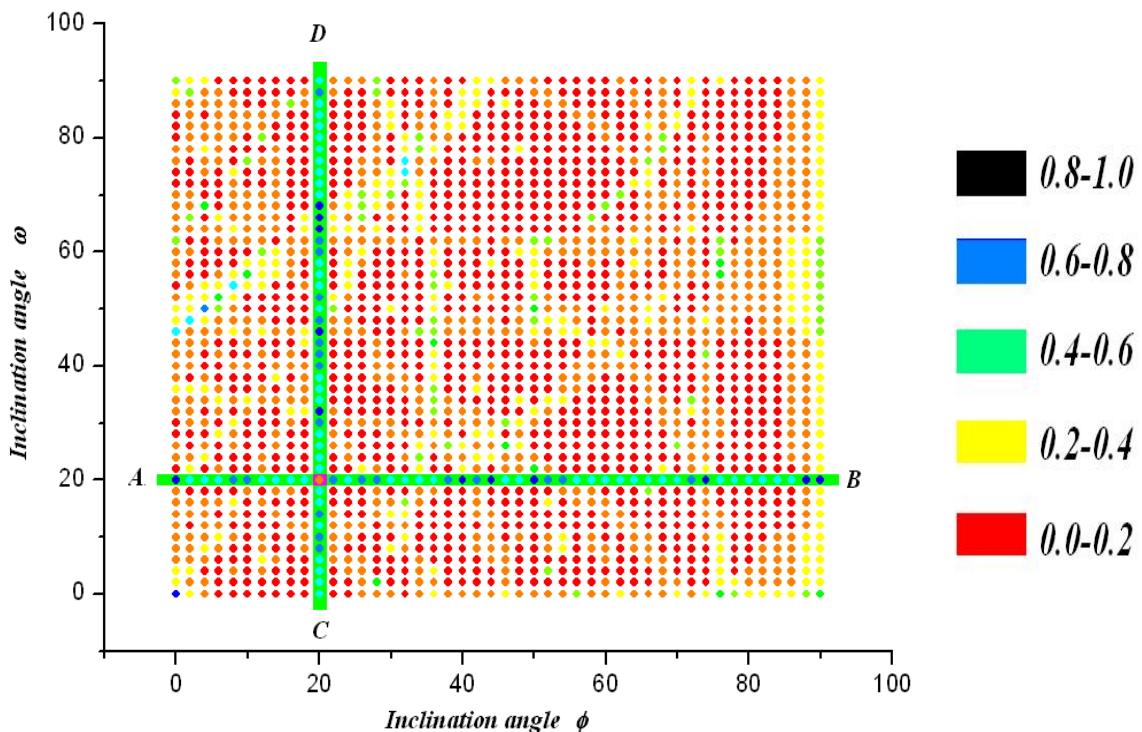


Fig. 3.19. Relative GB energy for GBI (0, 0, 0) (20,20,20). Inverted color scheme used for points on lines AB and CD.

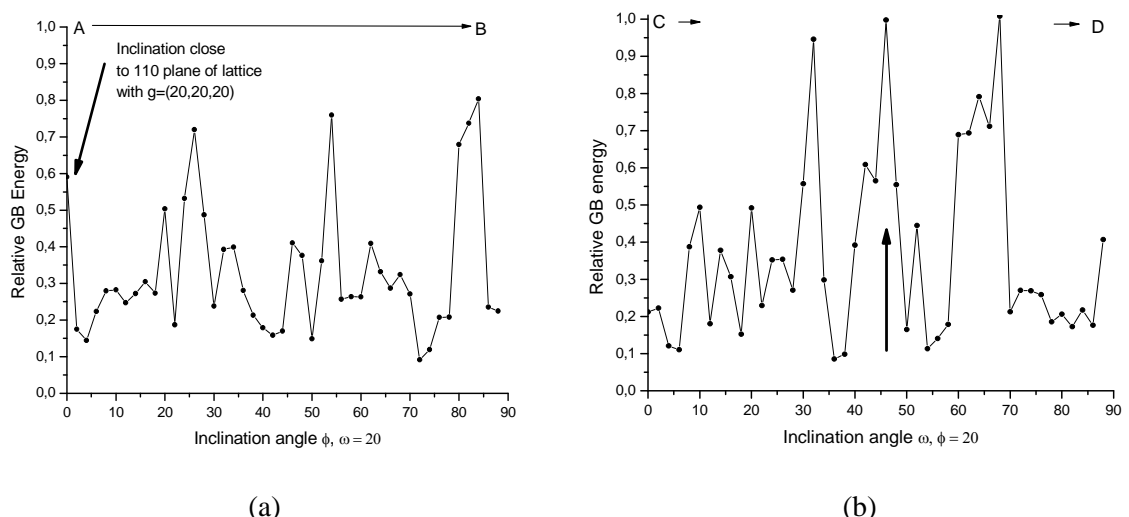


Fig. 3.20. Relative GB energy for sections A-B (a) and C-D (b) (see Fig. 2). Marked position (bold arrows) correspond to geometry, for which GB normal orientation is close to 110 direction of (20,20,20) oriented part of bicrystal.

Figure 3.21 presents actual data points (Fig. 3.19) as slightly smoothed (adjusted-averaging) color map. As it is well seen from the 2D map – peaks for GB energy corresponds (are close to) positions of low-indexed directions. Hence, it can be concluded, that GB energy has its maximum values when GBI normals are within the certain crystallographic zone of one of the bicrystals.

To form full database of GB as function of GBM+GBI with misorientation step of 2 degrees for one particular metal or alloy we need about $45*45*28 \approx 58\,000$ of such maps to be generated (See Fig. 3.23). However, when result is verified for few of them, calculations can be completed automatically. Then, when both databases for relative GB energy and mobility will be created, it can be used in 3D MC simulation of recrystallization or grain growth without any previously used simplifications, such as Tilt-Twist Component (Fig 1.21).

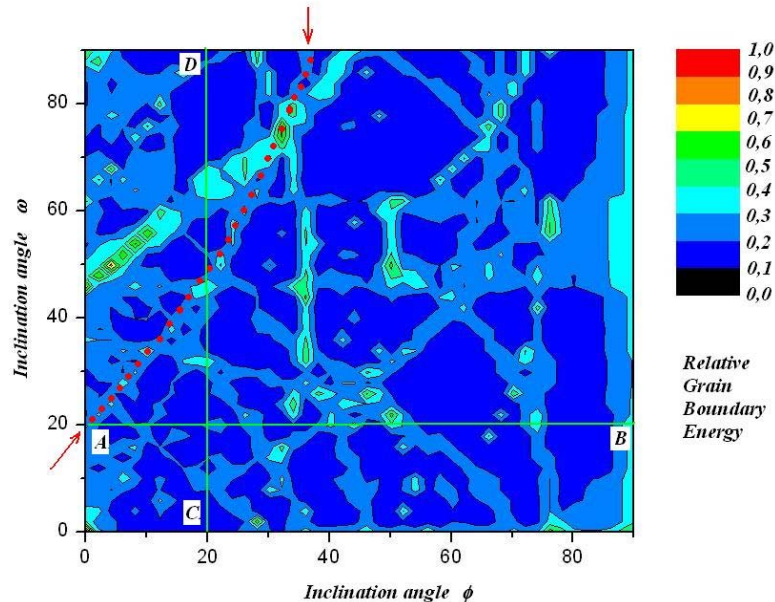


Fig.3.21. Relative GB energy smoothed (adjusted-averaging) color map for GBI (0, 0, 0) (20,20,20), $\phi \in [0, 90]$ and $\omega \in [0, 90]$.

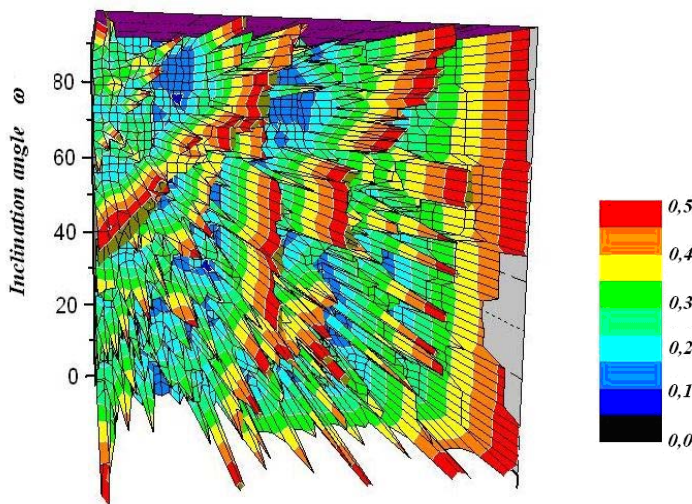
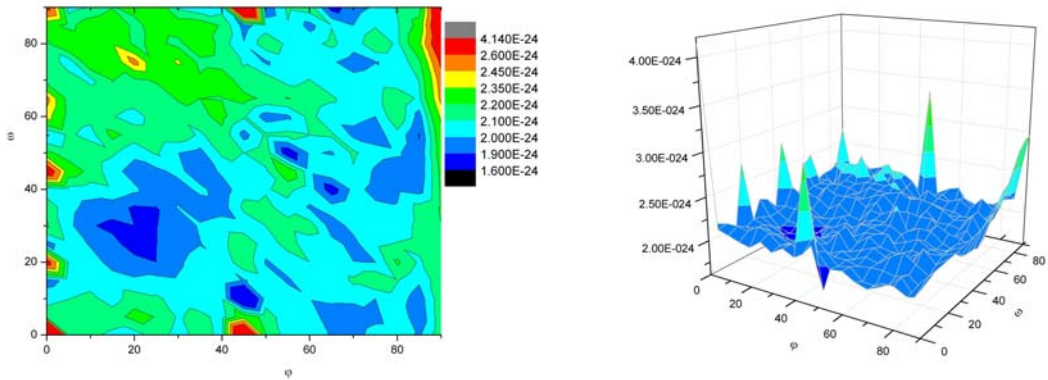
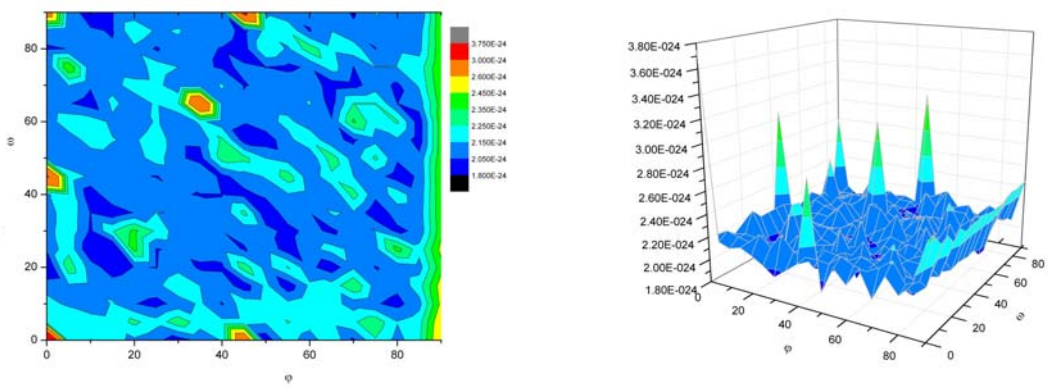


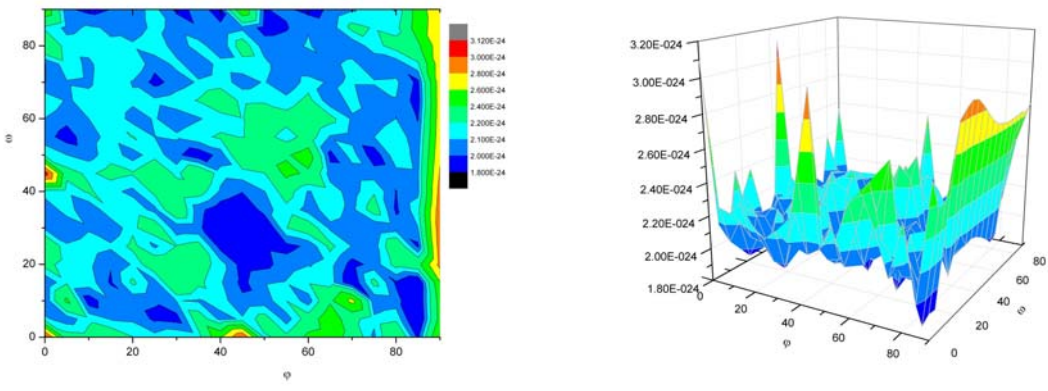
Fig. 3.22. Relative GB energy 3D plot, scale divided by factor 2 is used for best imaging.



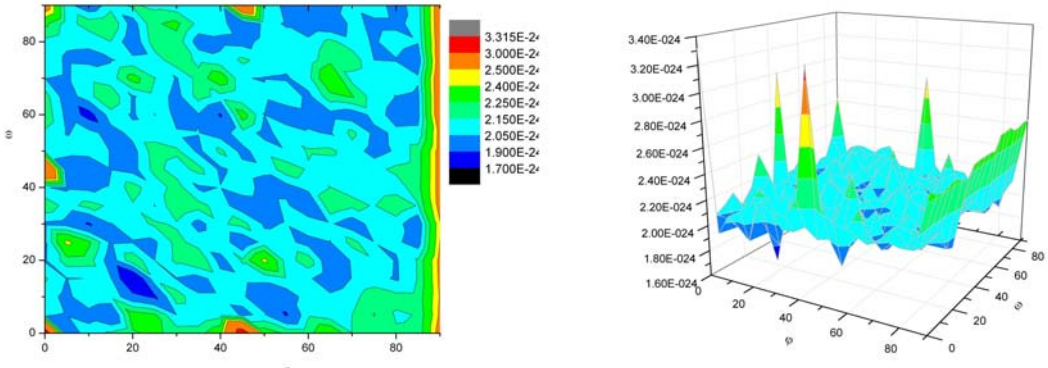
a)



b)



c)



d)

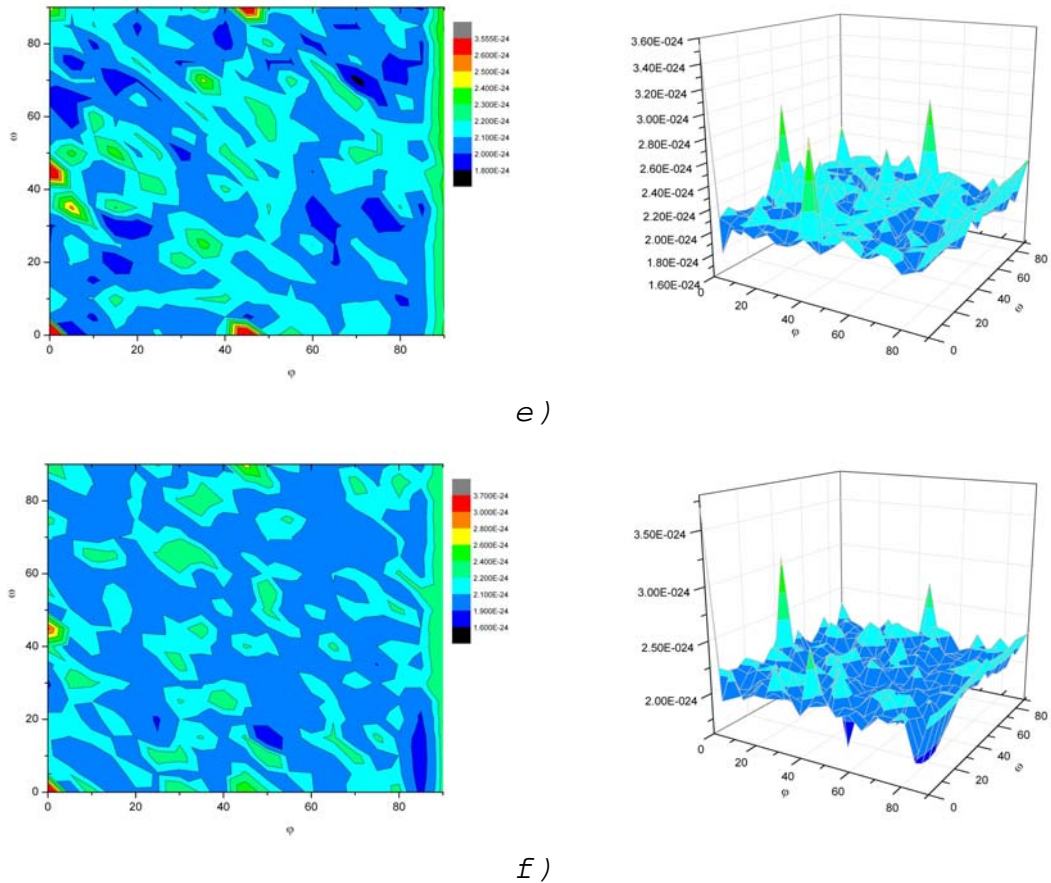


Fig. 3.23 GB Energy maps (J/Unit Cell) as function of GBI for series of GBM (0,0,0 – x,y,z) :
a) x,y,z = 1,3,7; b) 6,15,55 c) 8,2,6 d) 25,20,60 e) 40,15,10 f) 50, 0, 10

4. MC MODELING WITH IMPLEMENTED GBI AND MD DATA (STEADY STATE GB MIGRATION)

Steady state GB migration (GB misorientation (30, 30, 30) (0,0,0)) for half-loop GB geometry (Figure 4.1) was studied in 3D with MC approach for two cases:

- a) inclination independent GB effective mobility and
- b) locally GB inclination dependent effective mobility.

Effective mobility was assumed to be proportional to relative GB energy as determined early with MD approach (Figure 4.2).

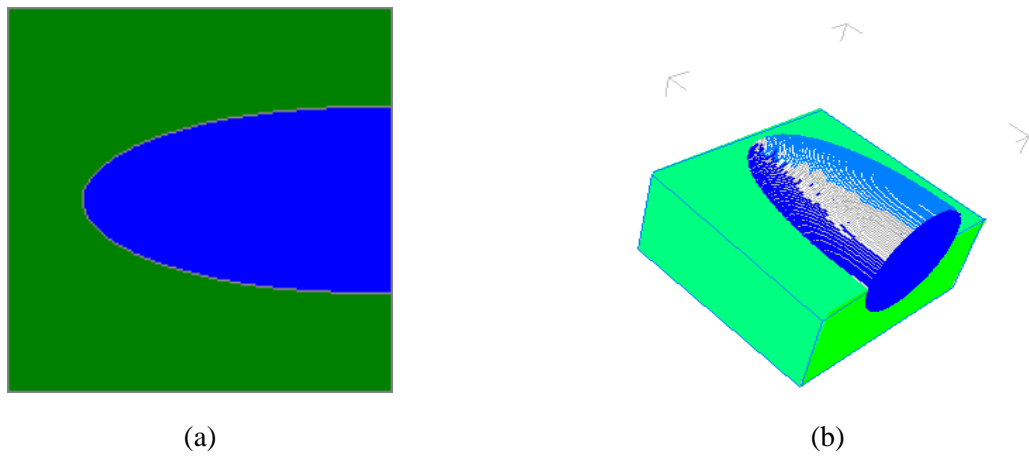


Fig. 4.1 Initial GB geometry for 3D MC and MD simulation (a) cross-section and (b) 3D view.

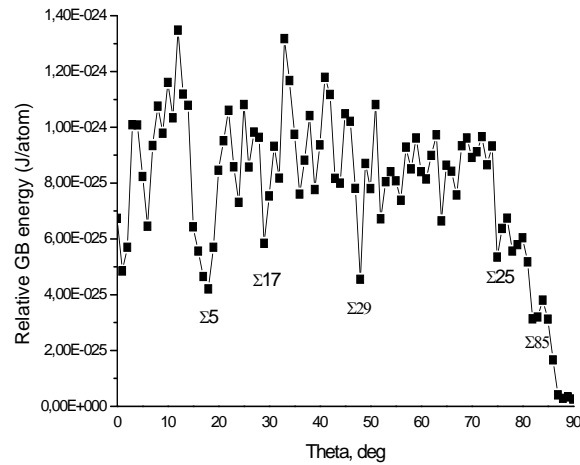


Fig. 4.2. GB energy as function of GBI (used as GB effective mobility in 3D MC runs). GB misorientation (30, 30, 30) (0,0,0).

It was shown that GBI dependent effective GB mobility assumed on the base of MD GB energy calculations when applied to MC simulated GB migration results in GB faceting in 3D (Figure 4.3). Some tendency for GB with GBI dependent effective mobility faceting can be already seen after the 10th MCS. Faceting becomes more pronounced during GB migration, although the number of facets decreases with time. No evidence of faceting was found for the case (a).

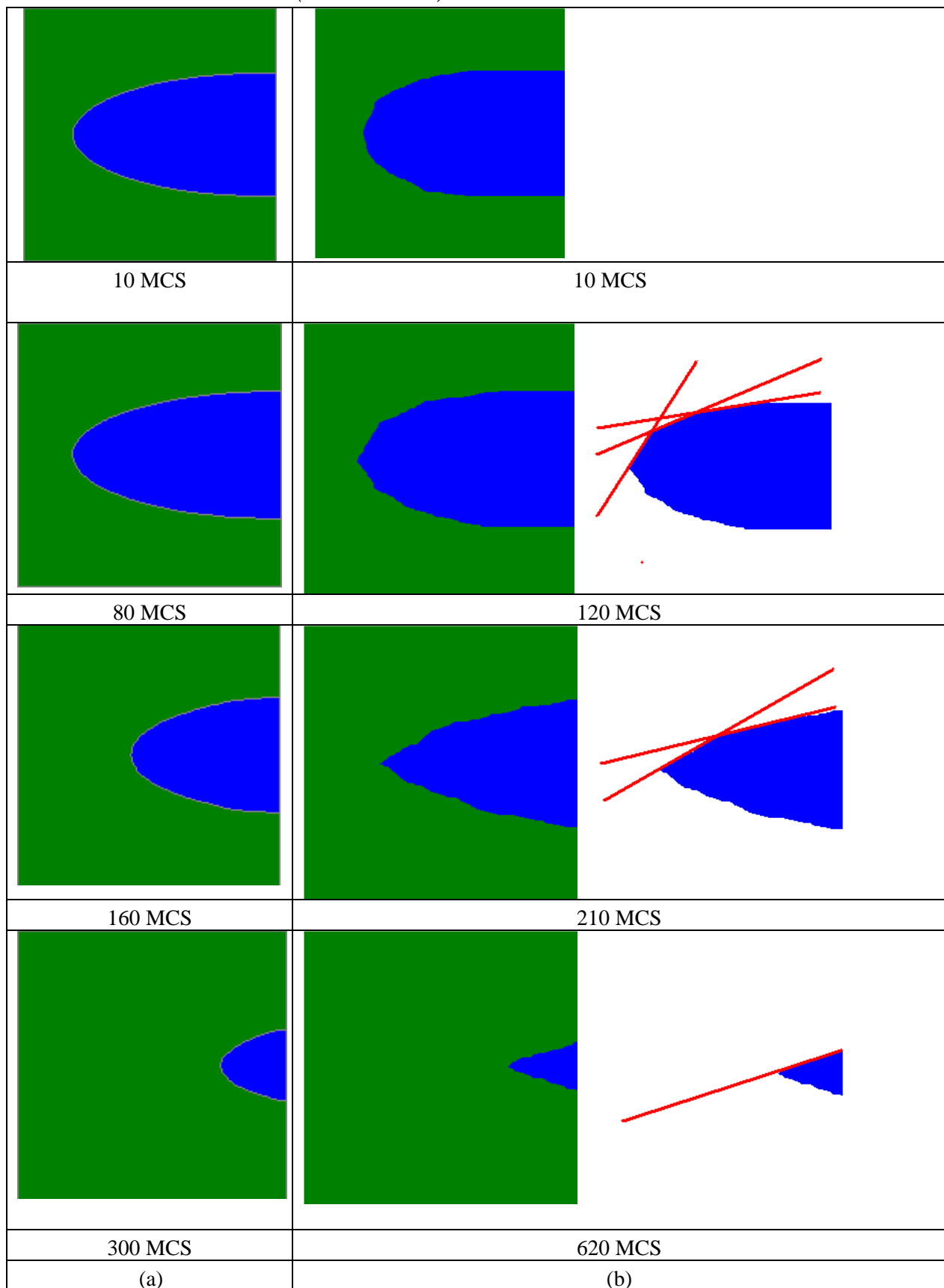


Fig. 4.3. MC simulated GB migration in bicrystal (3D half-loop geometry) with inclination independent GB effective mobility (a) and locally GB inclination dependent effective mobility (b).

Three dimensional analysis of GB shape evolution from the initial one to the steady state migration condition was performed. Initial GB configuration 0 MCS (light-grey), Figure. 4.4. Map for effective GB mobility (Fig. 4.5) for (0, 0, 0 20, 20, 20) misorientation is proportional to the GB relative energy GBI dependence. GBI normal/plane (0, 0) is parallel to 001 direction for “external” lattice (vertical direction/horizontal plane) on Fig. 4.4a).

GB configuration after 4000 MCS (dense-grey) and orthogonal cross sections analyzed, schematically at Table 4.1 and Figure 4.6.

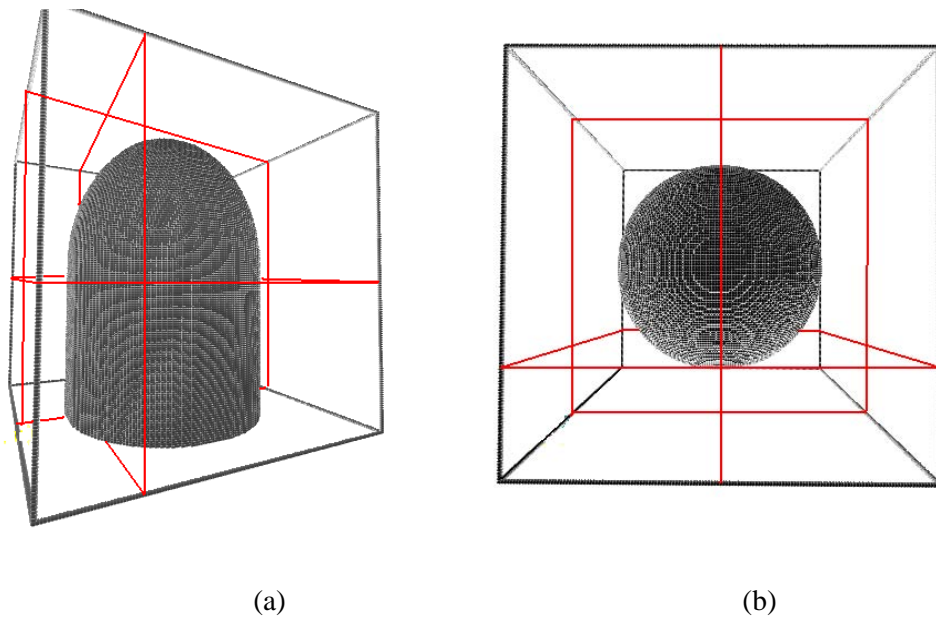


Fig. 4.4. Cross sections are parallel to the 001 planes of the “external” lattice.

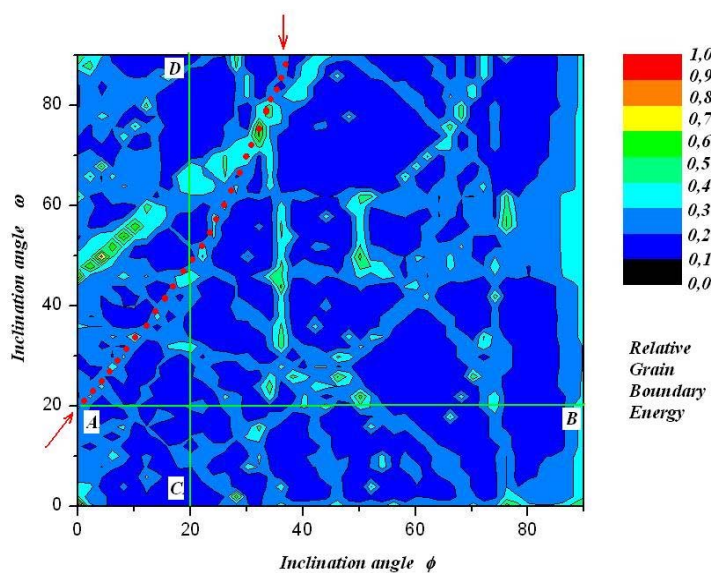
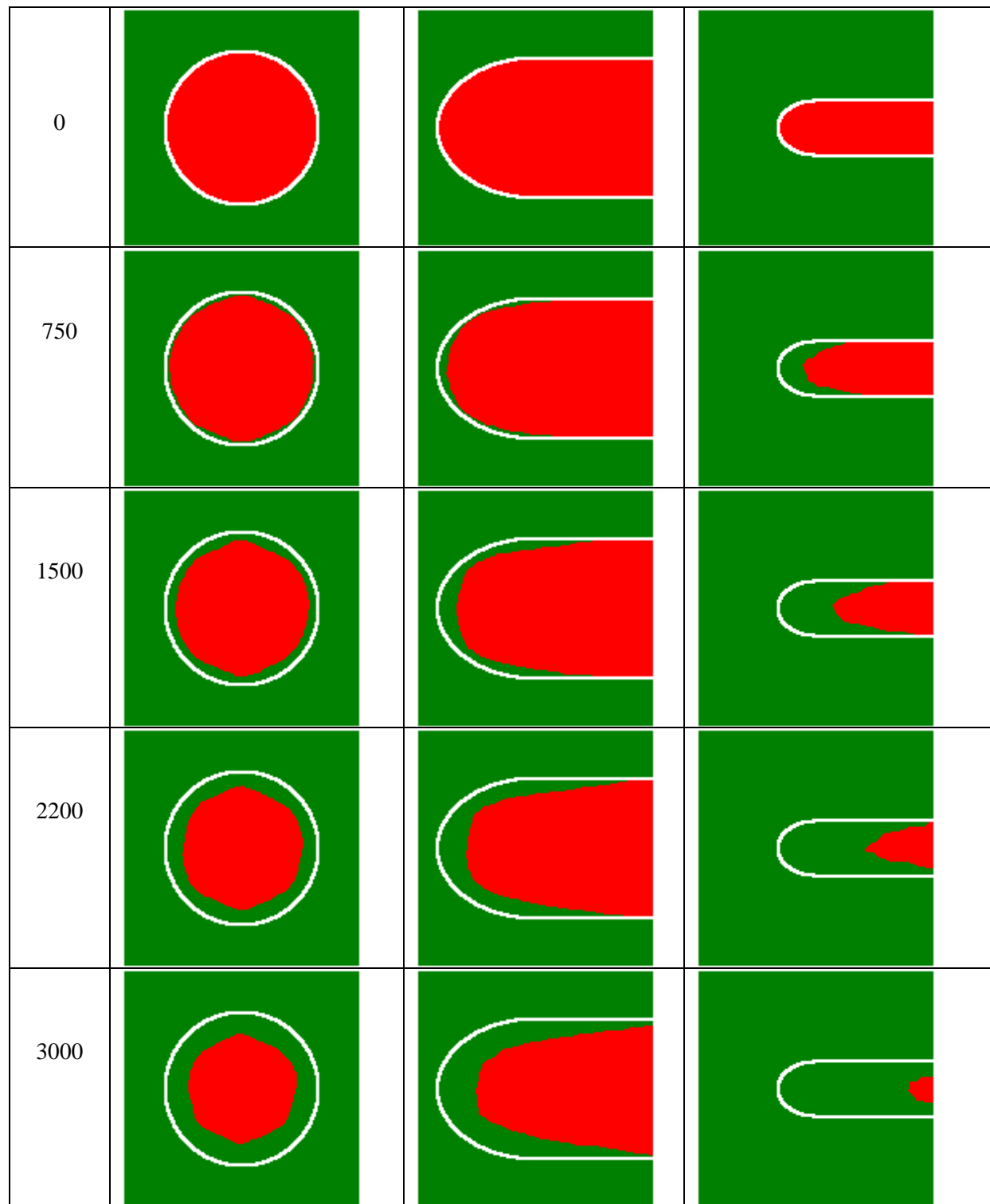


Fig. 4.5. Effective GB mobility (Fig. 1.33) for (0, 0, 0 20, 20, 20) misorientation - proportional to the GB relative energy GBI dependence.

Table 4.1. The sequences of migrating GB orthogonal cross sections.

White lines represent initial configuration.

MCS



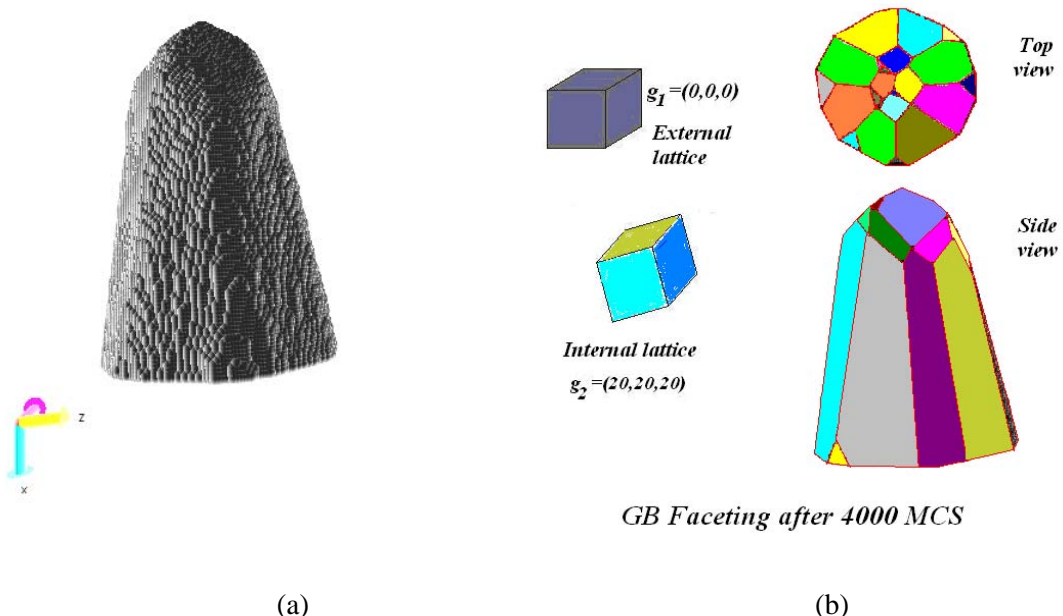
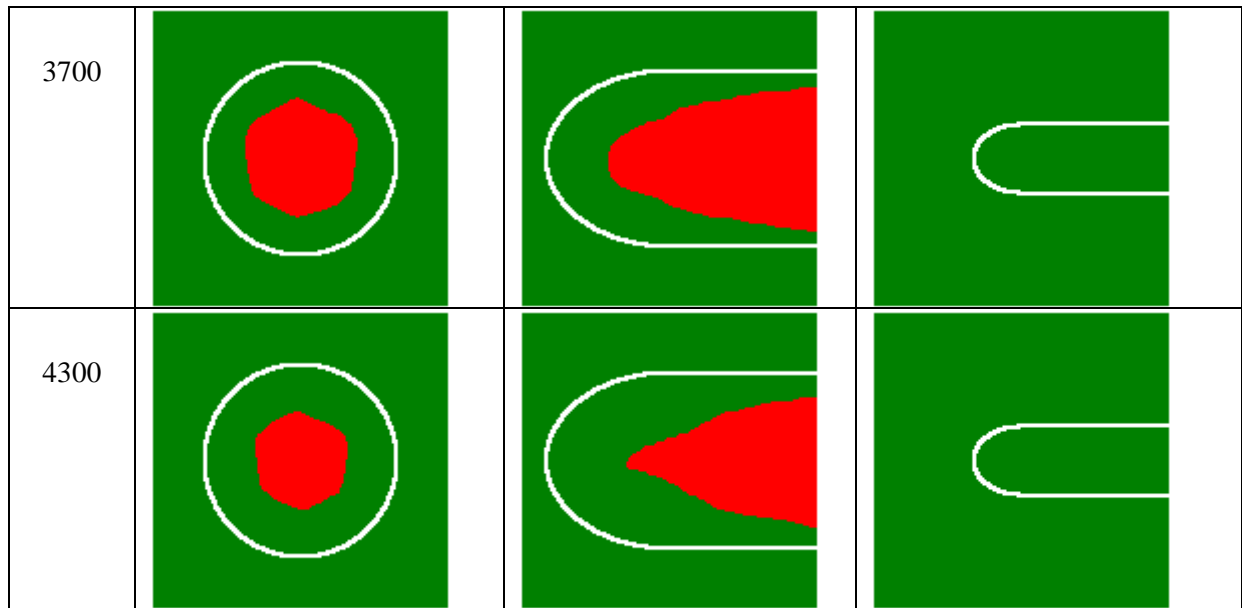


Fig. 4.6. Analysis of GB faceting in 3D after 4000 MCS. Reconstruction by voxels in gray light (a) and colored facets (b).

5. FORMATION AND ANALYSIS OF GB PROPERTIES DATABASE

Database for GB energy as function of exact GB geometry was created, partially filled with MD data and integrated to the MC Potts modeling software.

Database was developed in a form of electronic table for β -Ti GB properties data, namely GB energy and GB relative energy. Energy values are presented as function of three GB misorientation and two GB inclination parameters and allow data filling with angular step 1 degree.

Structure of GB energy database and calculated values ranges up to date are presented on Table 5.1. Angular step is given in brackets next to the angular range.

“Calculated” value – indicates that position in database filled by MD simulation procedure, developed in the frames of the project. However, available computational resources were not enough to complete all database – not yet completed GBs marked as “In Progress”

Table 2.1.

GBM Euler (1)	GBM Euler (2)	GMB Euler (3)	GBI (1)	GBI (2)	Energy value
0..10(1)	0..10(1)	0..10(1)	0.90(5)	0.90(5)	Calculated
		15..65(5)	0.90(5)	0.90(5)	
	15	0..10(1)	0.90(5)	0.90(5)	
		15..65(5)	0.90(5)	0.90(5)	
	20..65(5)	0..10(1)	0.90(5)	0.90(5)	In progress
		15..65(5)	0.90(5)	0.90(5)	
15..65(5)	0..10(1)	0..10(1)	0.90(5)	0.90(5)	Calculated
		15..65(5)	0.90(5)	0.90(5)	
	15	0..10(1)	0.90(5)	0.90(5)	
		15..65(5)	0.90(5)	0.90(5)	
	20..65(5)	0..10(1)	0.90(5)	0.90(5)	In progress
		15..65(5)	0.90(5)	0.90(5)	

5.1. Relative GB energy for specified GBM averaged on possible GBIs

Grain boundary energies were systematically calculated for various sets of lattice rotations (exact misorientations) corresponding to given scalar misorientations. Database for all Bunge angle combinations for scalar GBMs from 1 to 64 degrees was created. For each integer value of scalar misorientation all combinations that gives ε value in $\pm 0,02$ degree interval $(0,0,0)$ (φ, χ, θ) were derived. It was found that, for each scalar GBM, arrange of three corresponding Bunge angles consists from 250 to 830 variants. Examples of such arranges presented as tables 5.2 and 5.3.

Table 5.2 ($\varepsilon = 3 \text{ deg}$)

N	φ	χ	θ
1	0	3	0
2	1	1	3
3	1	4	0
4	2	2	3
5	2	5	0
6	3	3	3
.....
249	90	87	0
250	90	90	3

Table 5.3 ($\varepsilon = 29 \text{ deg}$)

N	φ	χ	θ
1	0	0	29
2	0	19	22
3	0	22	19
4	0	29	0
5	1	1	29
6	1	20	22
7	1	23	19
.....
829	90	71	22
830	90	90	29

Then, for all Bunge GBMs from particular arrange, GB energies were estimated, using software developed in the frames of the project. Two variants of GBI were used with above misorientation arranges, namely (20, 20) and (30, 30). Some results for (20, 20) GBI are presented on Figure 5.1.

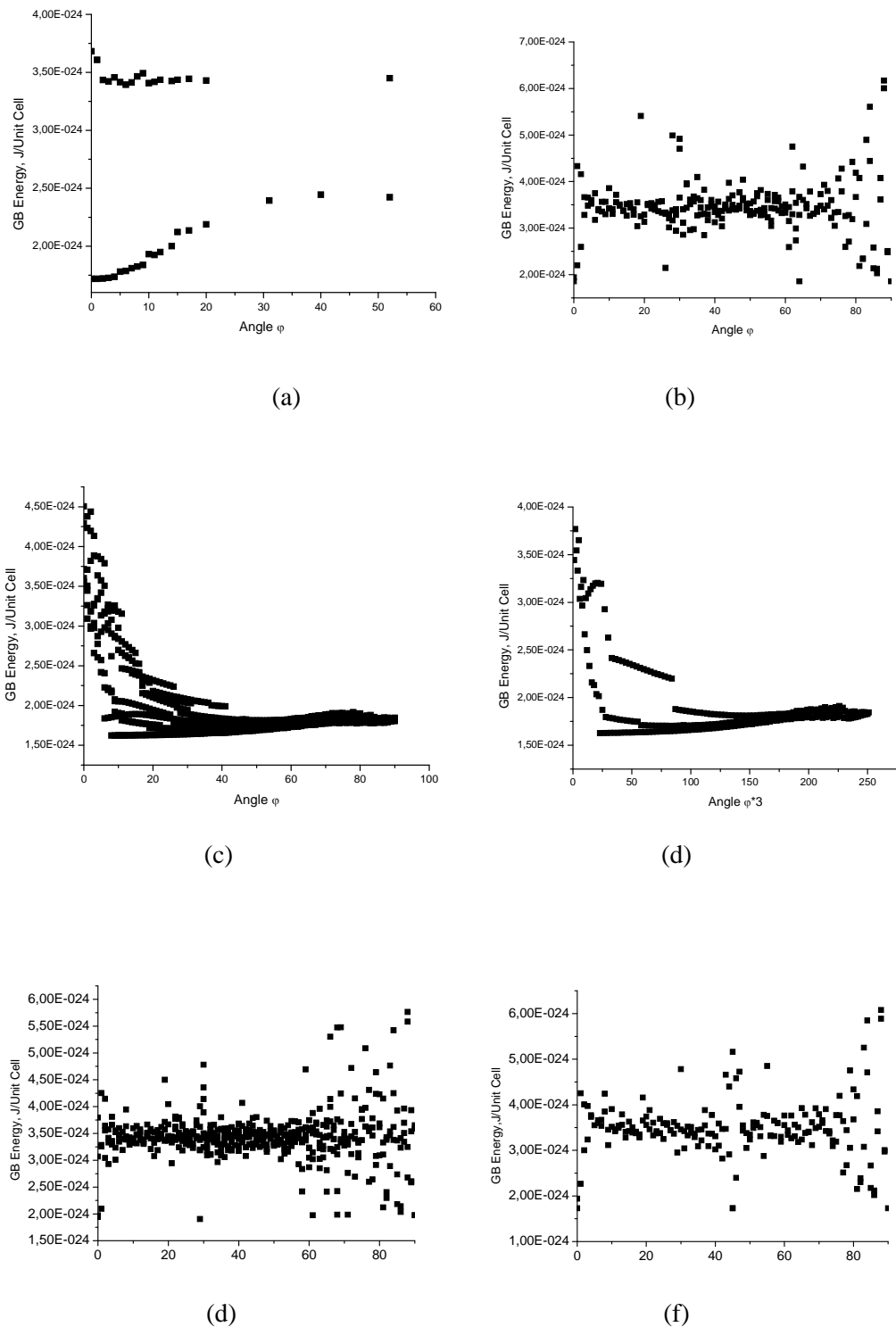


Fig. 5.1. GB energies for misorientations of: (a) 2 deg.; (b) 3 deg.; (c) 10 deg.; (d) 13 deg.; (e) 29 deg and (f) 45 deg presented as dependence on Bunge angles variant number in corresponding dataset (proportional to first rotation angle, for GBI (20, 20)

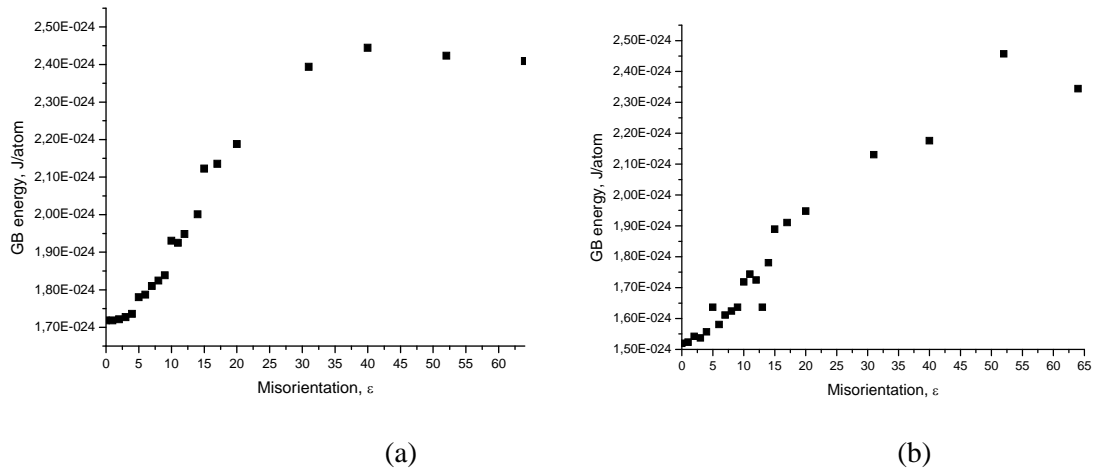


Fig. 5.2. Averaged for all orientation variants GB energy as function of misorientation (a) GB Inclination = (20, 20); (b) GB Inclination = (30, 30).

It is clearly seen, that for a given particular scalar misorientation number GB energy may differ up to 3 times (Fig. 5.1). The calculated for GBI (20,20) and (30,30) values of GB energies were averaged for all misorientations. It is interesting to note that the averaged energy dependence on misorientation looks similar to that usually used effective GB energies/mobilities [10] Figure 5.2.

5.2. Database validation on available experimental data

For specific GB geometry (non-symmetric tilt GB equivalent to recent experimental study [5] (Fig. 5.3)) GB energy was estimated as function of GBI, to compare MD simulation results with available experimental data (Fig. 5.4).

It can be concluded, that averaged experimental and MD simulated dependences are not in contradiction.

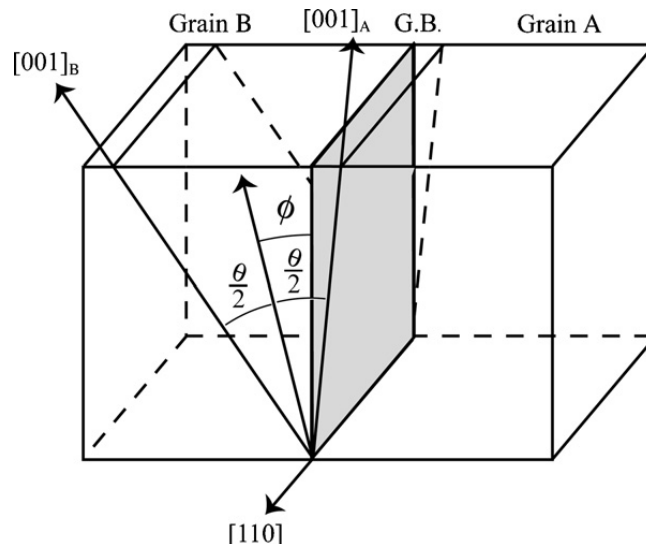


Fig. 5.3. Bicrystal with a [1 1 0] asymmetric tilt boundary [15]. The misorientation is defined as the angle θ (= 38,9 deg) between the [0 0 1] directions of two single-crystal grains, and the inclination is defined as the angle ϕ between the boundary plane and the bisector of the misorientation

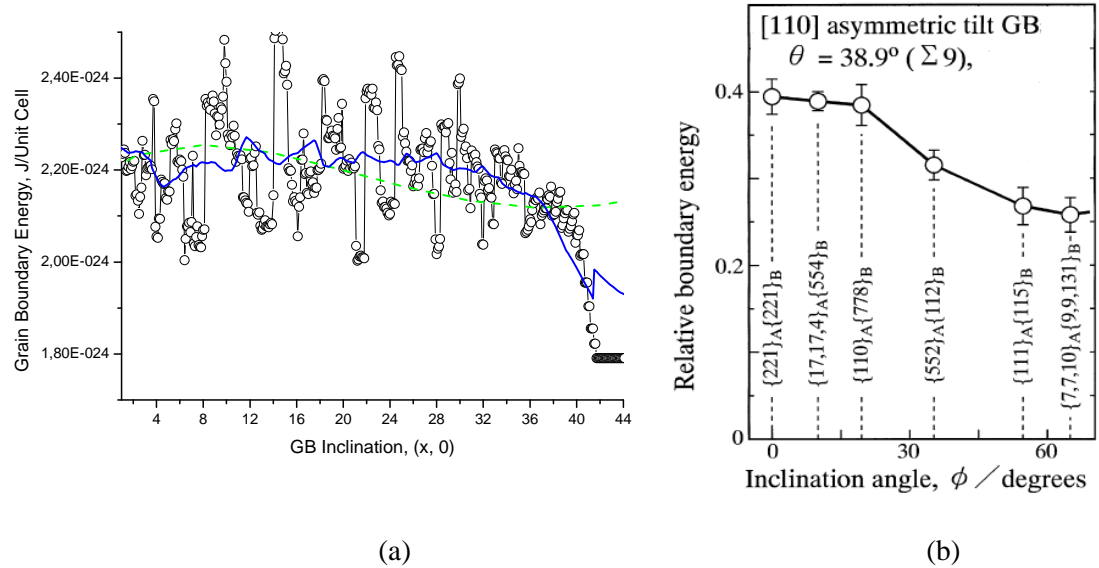


Fig. 5.4. Dependence of the tilt grain boundary energy on inclination ϕ : (a) MD estimated, lines correspond to deep spline averaging (dash green) and bin (20) averaging (solid blue) and, (b) experimentally measured in [15].

5.3. Comparison of different potential usage effect on relative GB energy.

Using advanced MD modeling software GB energies as functions of GBM and GBI was being continued for bcc bicrystal or general case of not special GB geometry were compared for cases, which utilizes essentially different interatomic potentials. Calculations done with simple Born-Mayer potential were compared with MD modeling runs with Lennard-Jones potential:

$$\phi_i = 4\epsilon \sum_{j \neq i} \left\{ (\sigma / r_{ij})^{12} - (\sigma / r_{ij})^6 \right\}, \quad \phi_{gb} = \sum_{j \in V} (\phi_i - \phi_0) / S_{gb}$$

($\sigma = 0.22$ nm, $\epsilon = 0.08$ eV, i.e. $a = 0.28665$ nm). GBI was defined with GB normal's angles ω and ϕ (see Fig.3.18).

At first, GB energy was calculated for (0, 0, 0) (20, 20, 20) GBM and GBI parallel to 100 plane of part of bicrystal with orientation (0,0,0).

Using above misorientation, map for relative grain boundary energy as function of GBI, (normal to GBI direction defined with ϕ and ω angles) using angular step of 2 deg for both ϕ and ω (about 2000 points) was built and compared with the same map for Born-Mayer potential (Fig. 5.5). Also for comparison of actual data GB energy section for one particular ϕ (30 deg) angle was plotted (Figure 5.6).

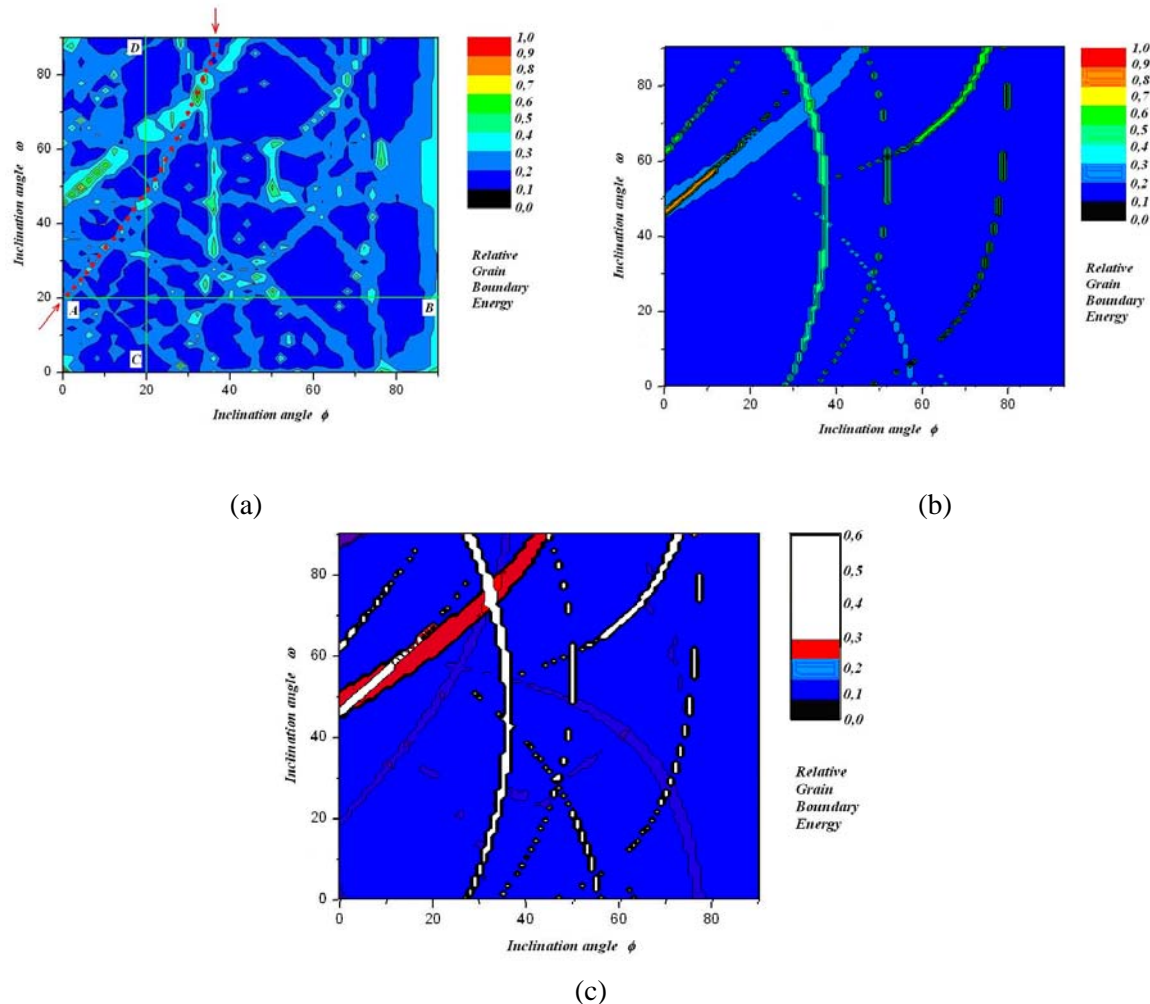


Fig. 5.5. Relative GB energy for GBI (0, 0, 0) (20,20,20). (a) Born-Mayer map (b) – Lennard-Jones map and (c) Lennard-Jones map rescaled for 4 levels.

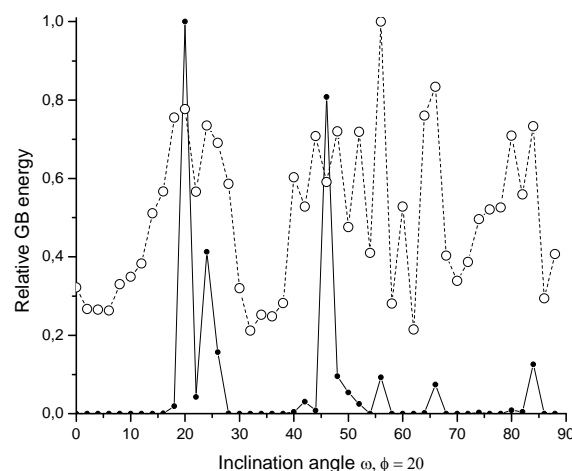


Fig. 5.6. Relative GB energy for GBI (0, 0, 0) (20,20,20) calculated with Lennard-Jones (solid line) and Born-Mayer (dashed line) potentials.

It is well seen from the Fig. 5.5 maps and Fig. 5.6 that peaks for GB energy calculated with different potentials are very close in positions, and these positions correspond to low-indexed directions. It is obvious that usage of the Lennard-Jones potential results in much sharper GB energy maximums, however there are no essential differences in their angular positions as compared to Born-Mayer potential.

Hence, it can be concluded, that GB energy has its maximum values when GBI normals are within the certain crystallographic zone of one of the bicrystals mainly due to GB geometry properties, and potential selection affects the shape and sharpness of the extrema.

For the MC Potts modeling of GB migration implementation of any “sharp” dependence of effective GB mobility, looks unreasonable. Difference in effective GB mobilities which exceeds 1:100 results in maximum velocity for low mobile GB less than 0,005 MU per MCS. Typical times for grain growth modeling are 500-1000 MCS, for recrystallization modeling 80-250MCS. Hence, just fixing of low-mobile GB will occur within the modeling volume. Therefore, usage of Born-Mayer approach looks preferable. It is also evident that calculations with Born-Mayer potential provide more detailed information on GB energy dependence on GBI and GBM.

6. β -Ti RECRYSTALLIZATION EXPERIMENT AND ADVANCED MC MODELING.

Commercial β -titanium alloy having actual composition Ti - 1.5 (wt.%) Al – 6.8 %Mo – 4.5%Fe – 0.2%O, (TIMETAL-LCB) was selected for analysis of recrystallization.

The initial microstructure, texture (ODF), spatial distribution of the stored energy of deformation are accounted when modeling to compare how differences in nucleation mechanisms and kinetics affect recrystallization.

6.1. Recrystallization in cold drawn LCB alloy

Experimental. The thermomechanical treatment route of LCB rods included solid-solutioning at temperature of single-phase β -field at 850°C during 1 hour with subsequent water quenching. As a result single-phase metastable β -condition with average β -grain size of about 180 μm was obtained.

Quenched specimens were cold drawn with 70% reduction to the final diameter 8 mm, then cut into specimens of 60 mm for subsequent bulk (RHT) performed with direct electric current resistant heating, 20 C/s to different peak temperatures within the recrystallization interval (Figure 6.1).

Two comparative Cases A and B were run to estimate how accounting of exact GB geometry affects recrystallization in microstructures similar to those observed experimentally in LCB titanium alloy.

Modeling. Modeling volume was constructed to mimic cold drawn condition including texture and microstructure. In both Cases 3 and 4 nuclei were allowed to form only in misorientations, selected from Table 6.1. Proper selection of nuclei orientations allowed recrystallization front motion be traced by using exact GBM+GBI approach (Case B) while in Case A effective grain boundary mobility followed commonly used dependence on scalar misorientation. All other initial parameters and conditions were the same in both cases A and B.

As expected, predicted recrystallization kinetics are different due to the slower migration of unfavorably inclined parts of RX front in Case B (Figure 6.2). Some difference in recrystallized microstructures are seen from Fig 6.3. For Case 4 at 50MCS (80% Rex.) it is clearly seen preferred GB inclinations and grains arranged in vertical lines (along the long axes of the deformed grains).

Similar regular grain arrangements are seen on the experimental LCB grain boundary maps for 95% recrystallized material (Fig 6.4).

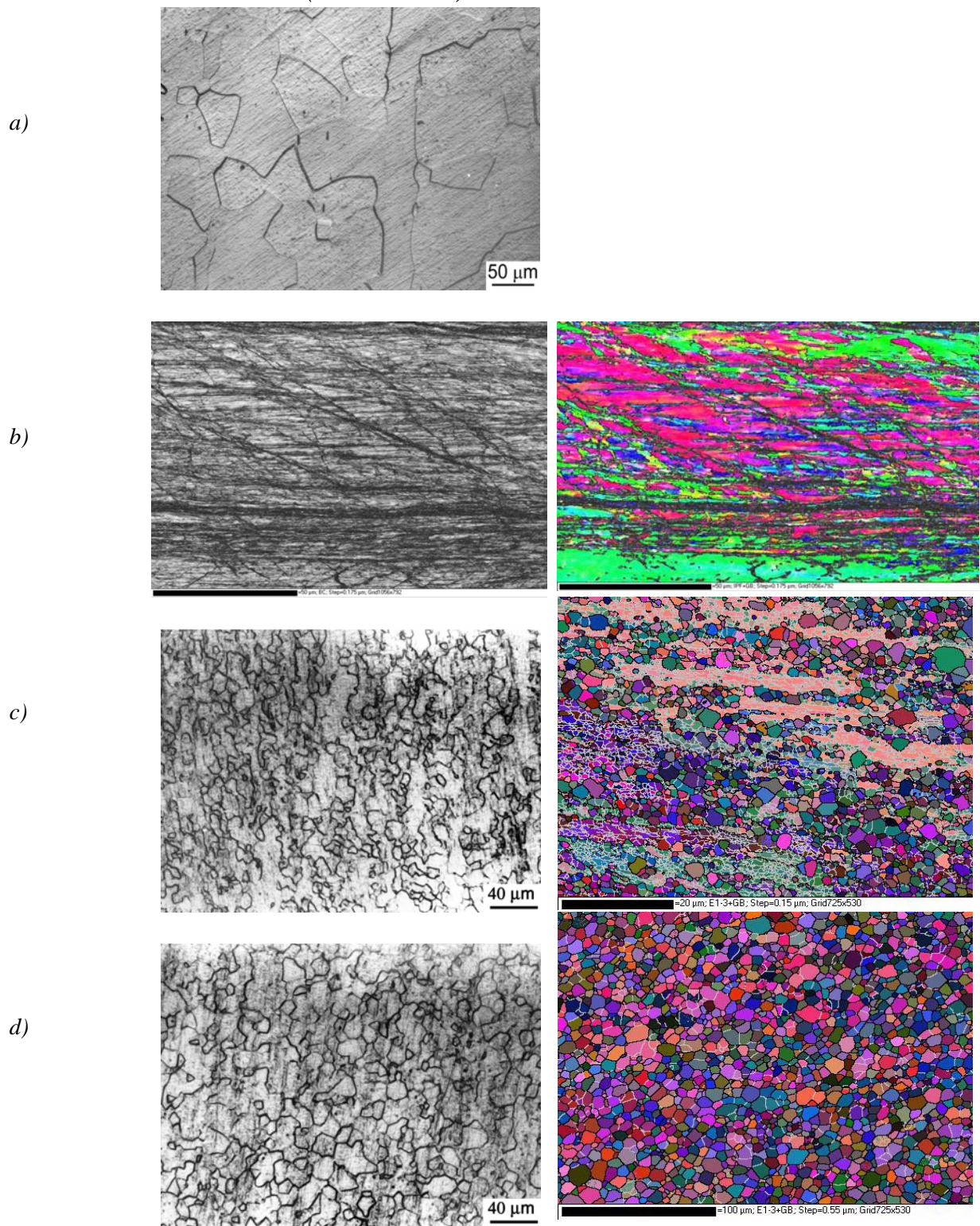


Fig. 6.1. Optical (left) and EBSD (right) images of a) solid solutioned; b) cold drawn; c) 50% Recrystallized and d) 100% recrystallized material.

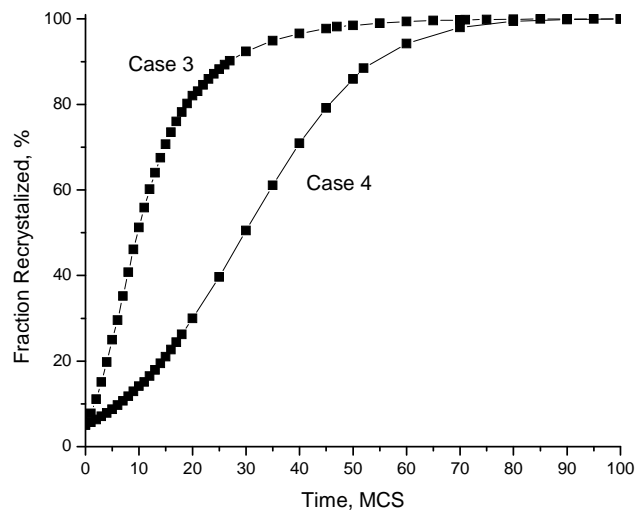
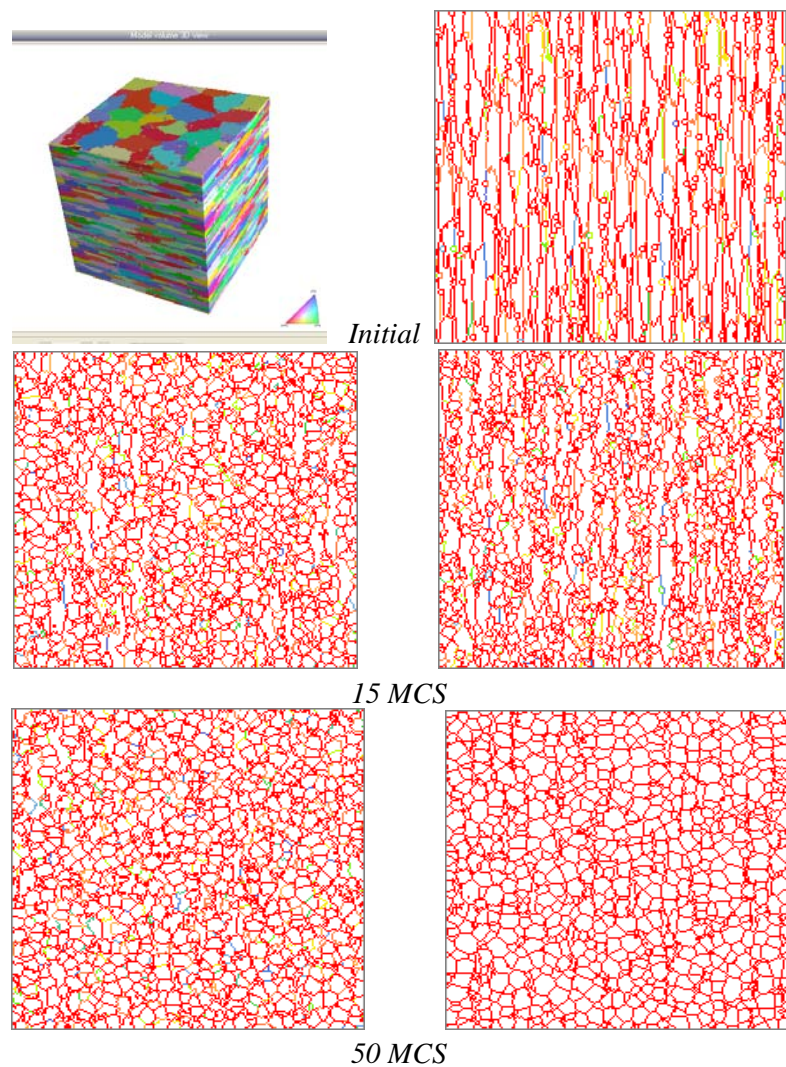


Fig. 6.2. Predicted recrystallization kinetics for Cases A and B.



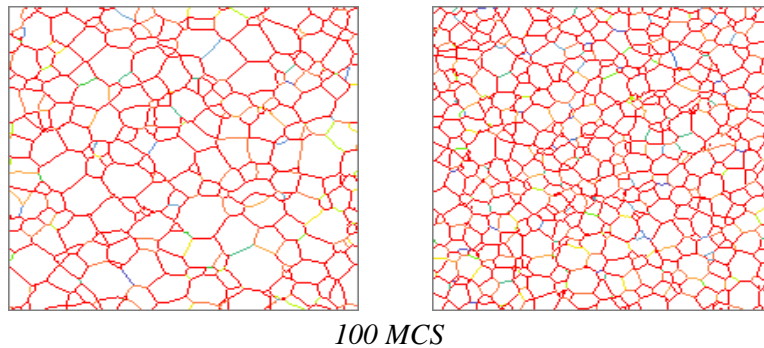


Fig. 6.3. Simulated microstructures for Cases 1 (left) and 2 (right). GB color is proportional (red GBs > 15 deg mis, other < 15 , blue < 2 deg)

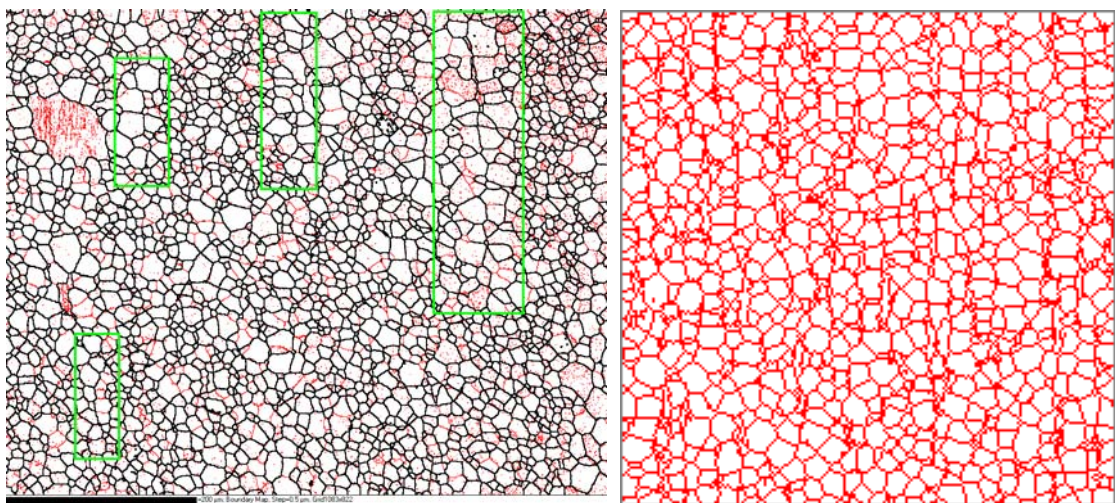


Fig. 6.4. LCB 95% Rex. EBSD Grain Boundary Map (400*500 μm) shows grain arrangements (marked with green color) which looks similar to Case 4 simulated patterns (right).

6.2. Recrystallization in specially textured 3D MC volume

For 15 selected grain orientations GB energies were calculated as those depending on GBI: full maps of GBI dependant GB energy were built for grain misorientations listed below (Table 6.1) with one grain in (0,0,0) position, as well as for possible pair misorientations from the list. Calculated maps are shown on Figs. 6.6 and 6.7. Using these orientations, an artificial as-deformed microstructure was constructed, which was used for MC simulation with taking into account exact grain boundary geometry (GBM+GBI). Such method of construction for initial as-deformed 3D modeling volume guarantees presence of the finite set of possible misorientations in modeling volume, with known GBI dependencies for GB energy. Effective GB mobilities were assumed to be proportional to corresponding GB energy.

Table 6.1.

N	φ, deg	χ, deg	θ, deg
1	21	21	3
2	30	30	3
3	0	0	3
4	3	2	15
5	0	0	15
6	31	22	12
7	32	44	9
8	45	45	0
9	10	35	0
10	12	37	0
11	14	39	0
12	0	0	30
13	18	48	0
14	37	7	0
15	45	45	45

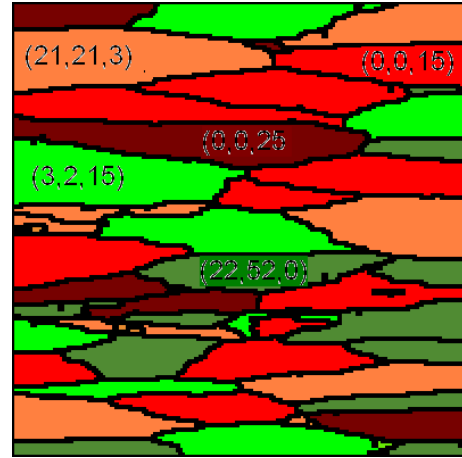
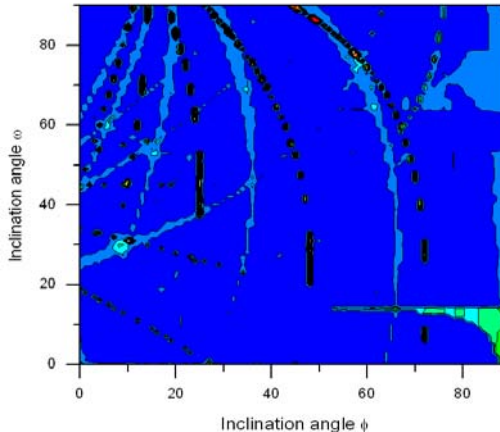
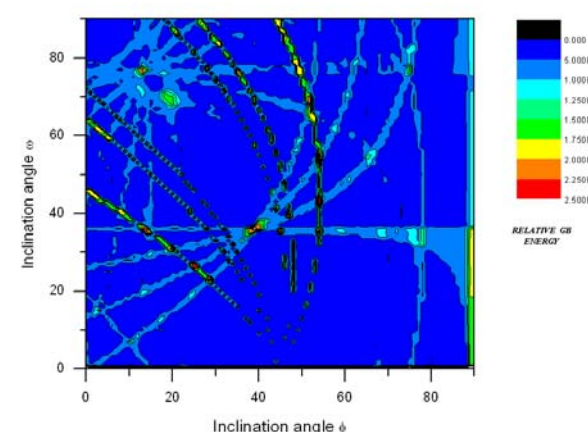


Fig. 6.5. Initial (as-deformed) microstructure.



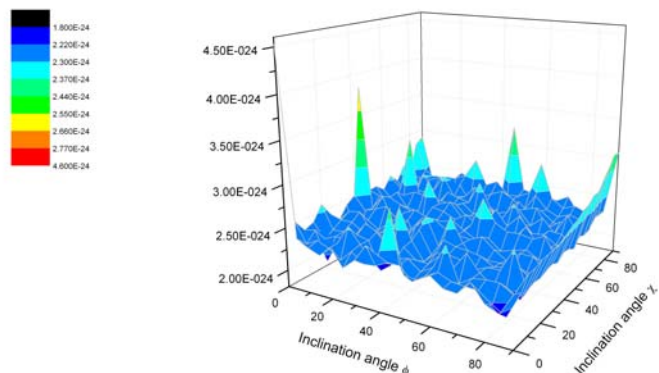
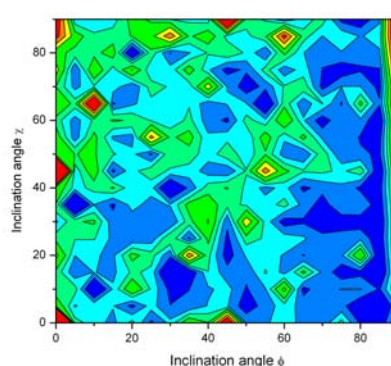
(a)



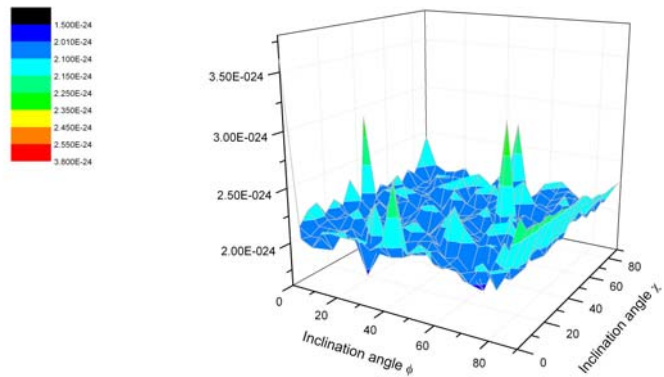
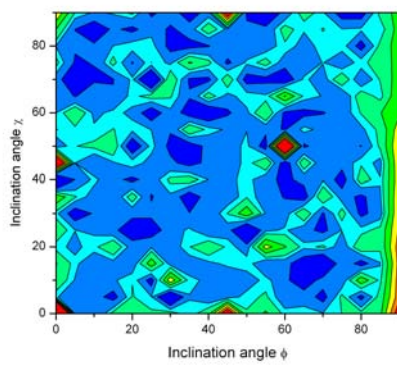
(b)

Fig. 6.6. Dependence of relative GB energy on GBI for high symmetric GBMs: (a) (45,45,45) and (b) (45,45,0).

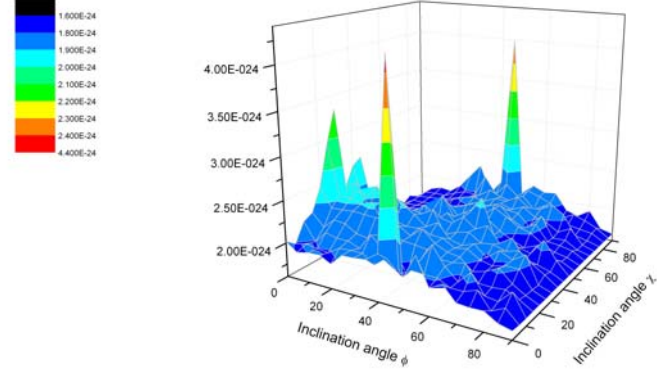
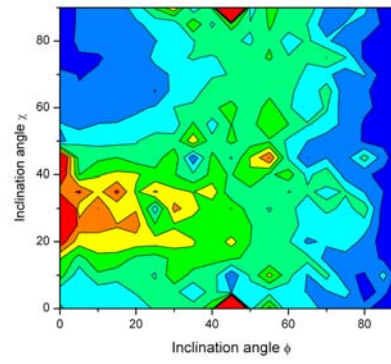
Two MC Recrystallization simulation runs were completed, with (case 2) and without (Case 1) accounting energy GBI dependencies. Starting from the same as-deformed microstructure presented on Fig. 6.5 recrystallization starts with 300 nuclei. Orientations of nuclei were selected randomly from Table 6.1. As expected, due to the reduced average mobility when GBI dependencies are accounted, Case 2 performs slower kinetics of recrystallization (Figure 6.8). Microstructure evolution for Cases 1 and 2 is presented on Fig. 6.9.



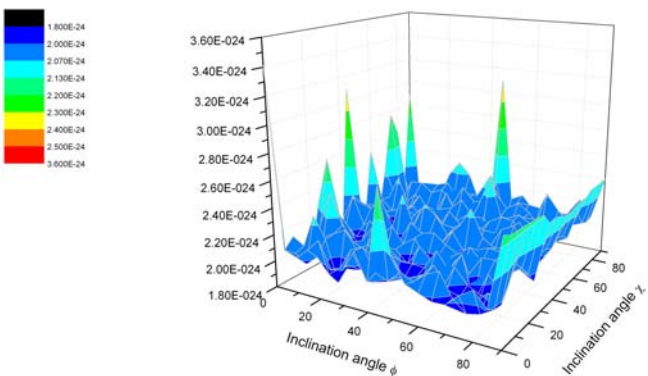
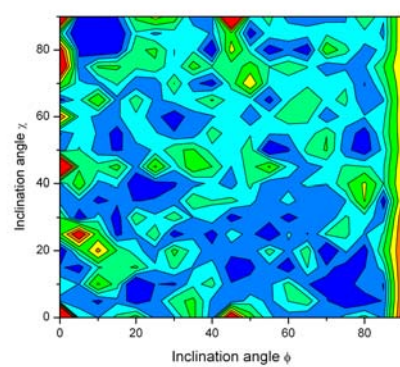
(21,21,3)



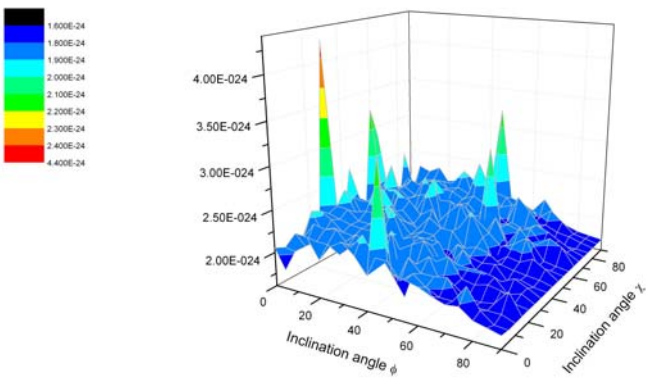
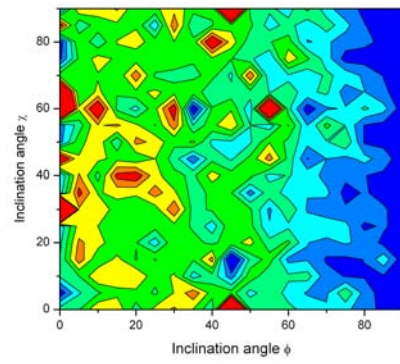
(30,30,3)



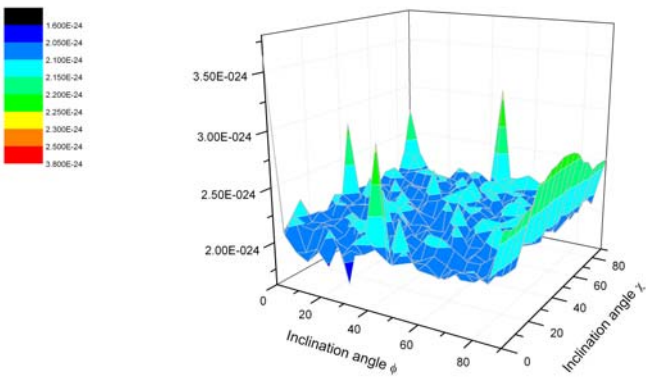
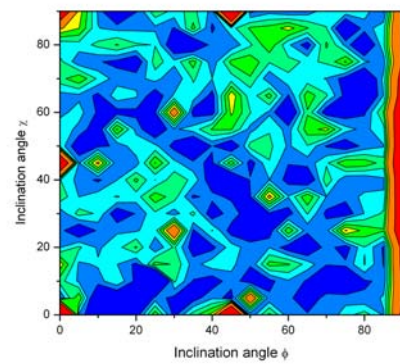
(0,0,3)



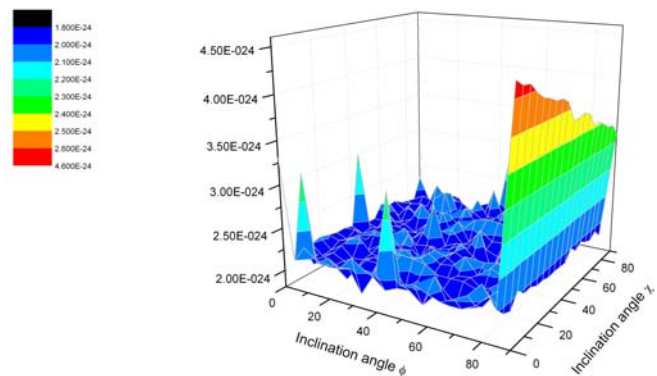
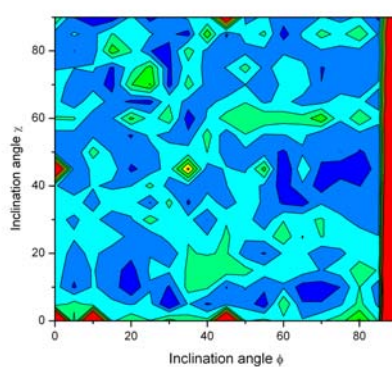
(3,2,15)



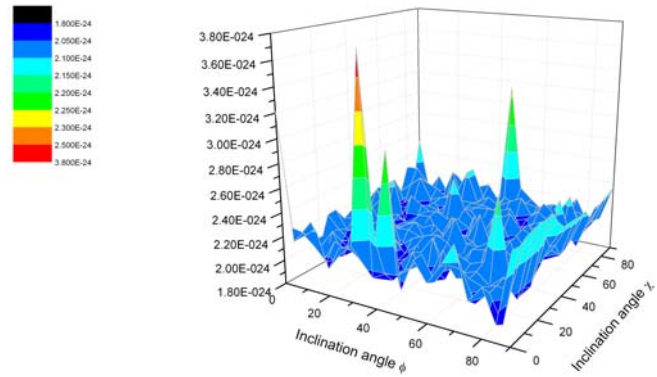
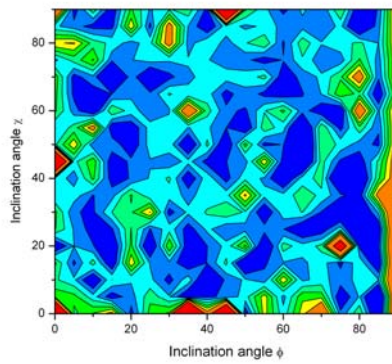
(0,0,15)



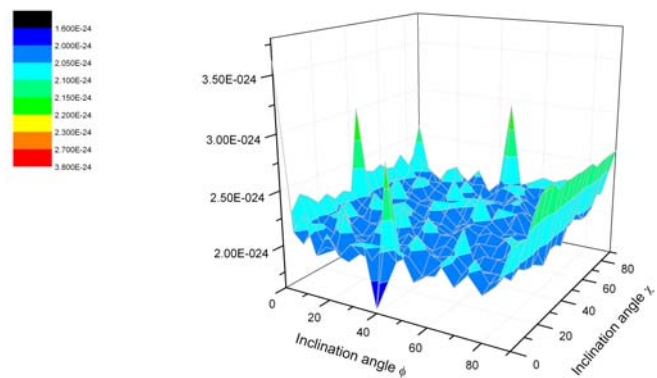
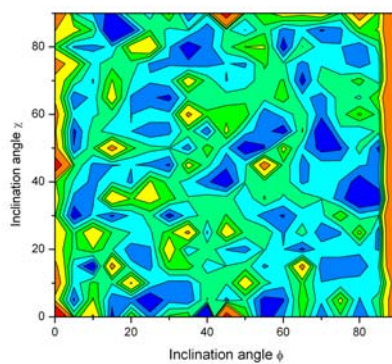
(31,22,12)



(10,35,0)



(12,37,0)



(14,39,0)

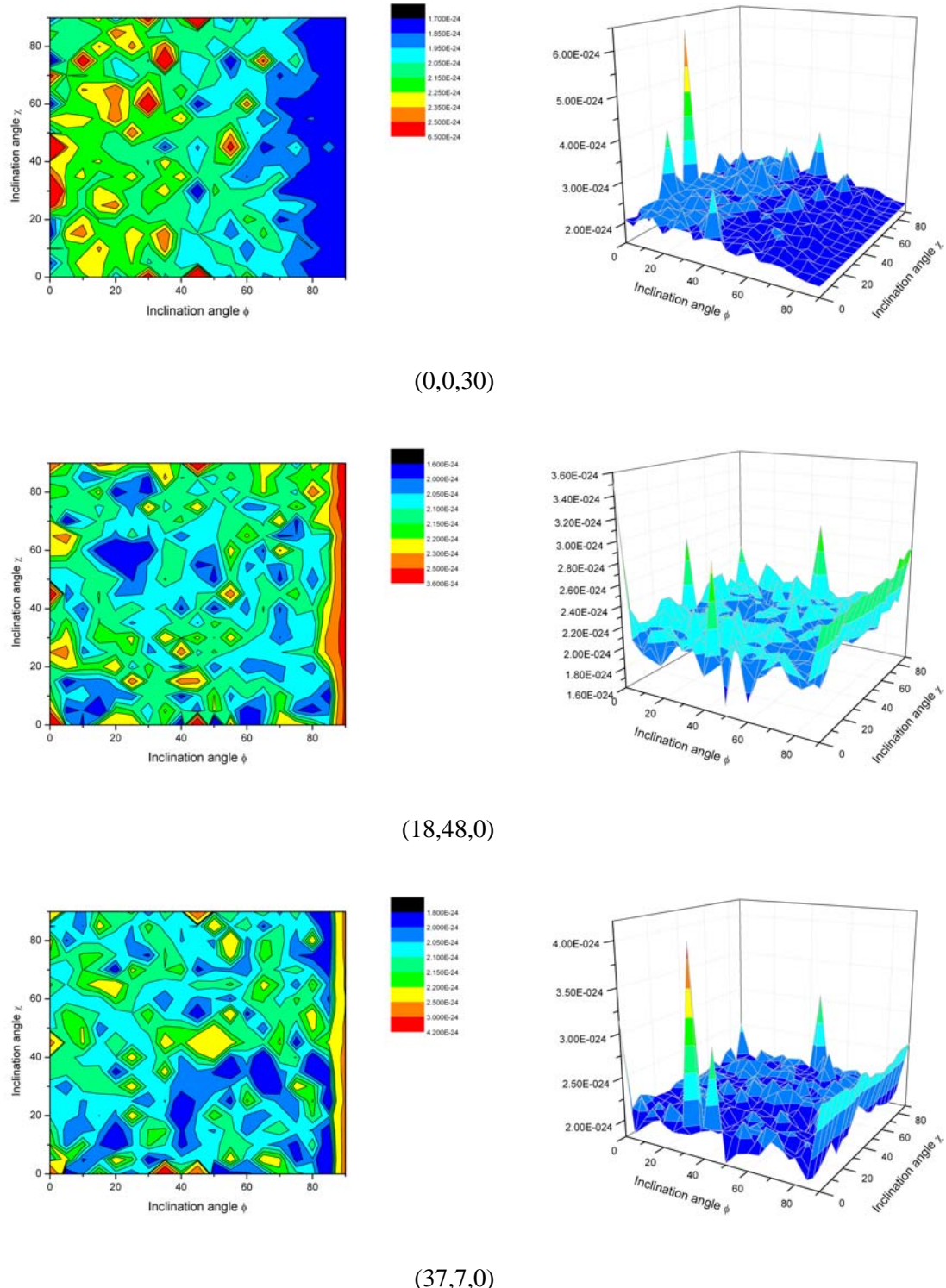


Fig. 6.7. Dependence of relative GB energy on GBI for general GBMs from table 6.1.

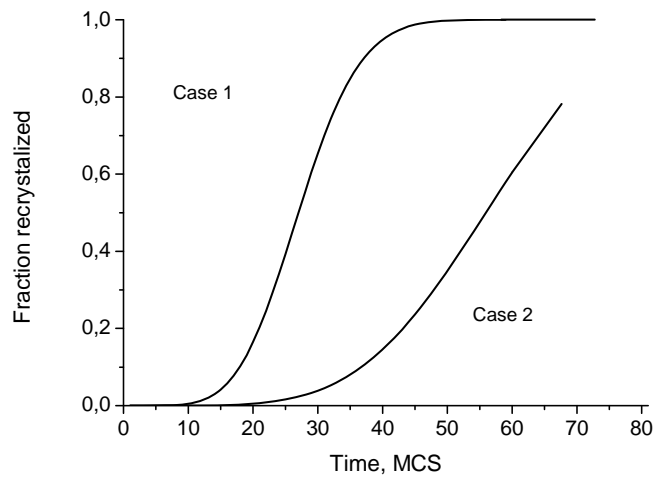
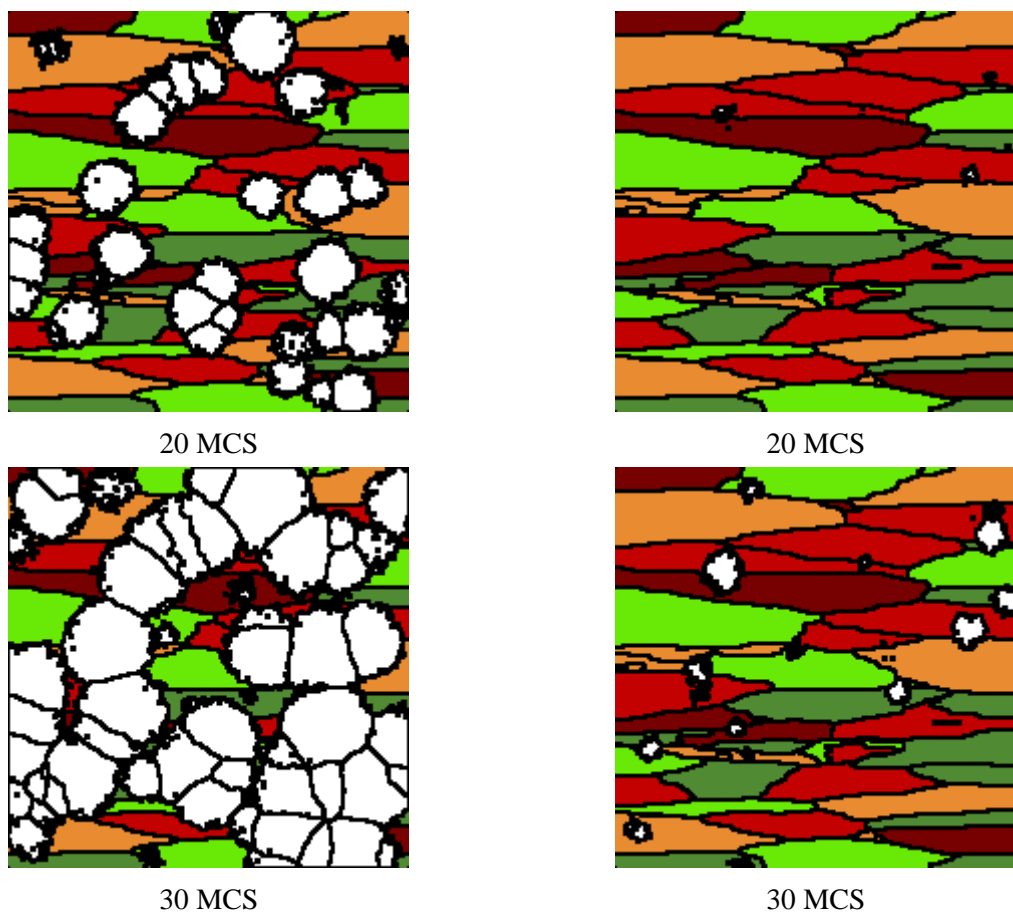


Fig. 6.8. Recrystallization kinetics for Cases 1 and 2.



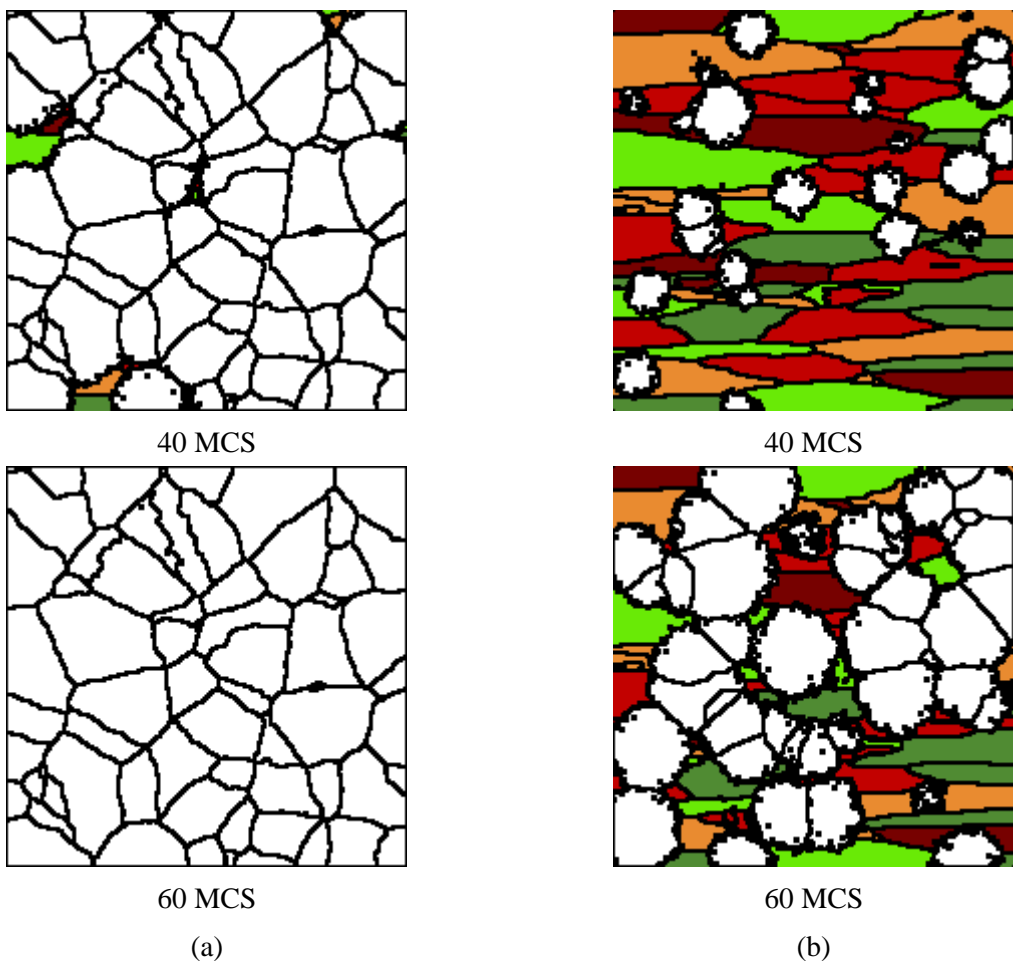


Fig. 6.9. Microstructural evolution: (a) Case 1; and (b) Case 2.

Microstructures at 60 MCS for Cases 1 and 2 show some difference in GBI population, which is random for Case 1 and partially follows some definite planes for Case 2. (Figure 1.39).

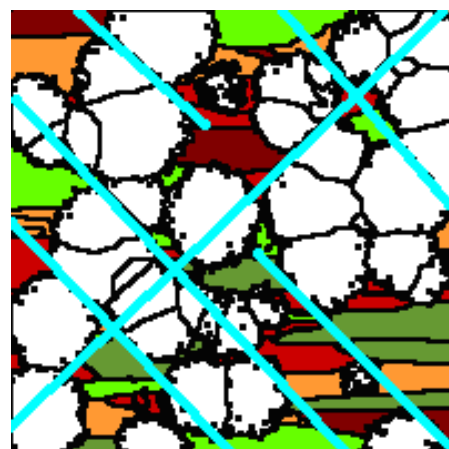


Fig. 6.10. Some favorite GB planes for Case 2, 60 MCS.

6.3. MC Recrystallization Software development.

New program for MC Potts modeling of microstructural and textural evolution within the 3D modeling volume was tested and installation package on CD was generated. Project software CD was send to partners (Dr. Wynn Sanders, EOARD and Dr. Lee Semiatin, WPAFB).

Two screenshots are presented on Fig 6.11. Installation package is included with project CD.

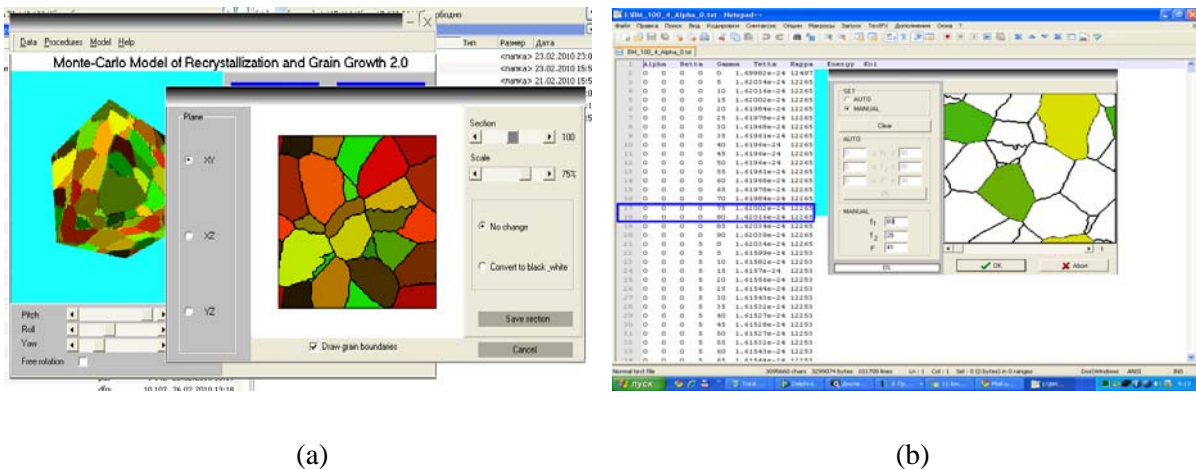


Fig. 6.11. MC Potts Rex. and GG software: (a) modeling volume analysis; (b) searching for GB energy value within included database.

Distinguishing features of the software are:

- Exact GB description into the 3D MC code was implemented. Now usage of an exact GB misorientation (five fold GBM+GBI), instead of the usual scalar approximation, is possible;
- Procedure for local GBI estimation according to developed procedures (see section 1);
- Software allows including of the GB properties database, generated by GB MD simulation routine for instant usage during MC Potts modeling run;
- Manual setup for grain orientations in the “as deformed” state now is possible.

7. RELATIVE GB EFFECTIVE MOBILITY.

To estimate GB effective mobility for 3D MC simulation technique, it is also needed to determine the mobility of a single GB as function of both GBI and GBM, and then calculate relative GB mobilities as functions of GBI for each particular GBM.

Two GB geometries were selected for MD simulation of GB mobility as function of GMB+GBI. The first one is traditional bicrystal half-loop geometry. This geometry allows to investigate the shape of a moving grain boundary and use it as a source of data with regard to the GBI dependence of GB mobility both experimentally and with MD simulations.

For given misorientation (Figure 7.1a) half-loop geometry allows to estimate GB effective mobility for all possible GB inclinations. When GB migrates, its shape is changing towards the polygon, with sides close to the inclination of the slowest GB segments. In modeling experiment with GBI dependent GB velocities of local GB segments will differ from reference V_1 and V_2 velocities for GBI 1 and GBI 2, correspondingly (Fig. 7.1a).

By using quite similar (quarter-loop, Figure 7.1b) geometry the above was shown experimentally for various metals, for instance, Al [11] (Figure 7.2). On figure 6a grain boundary segmentation due to the differences in GBI dependent mobility is clearly seen.

However, such approach requires a huge amount of computational time. As a result, in [3] simplified ‘molecular statistic’ approach was used instead of MD, and just for 2D case. Hence, we plan to study only several key misorientations with this approach.

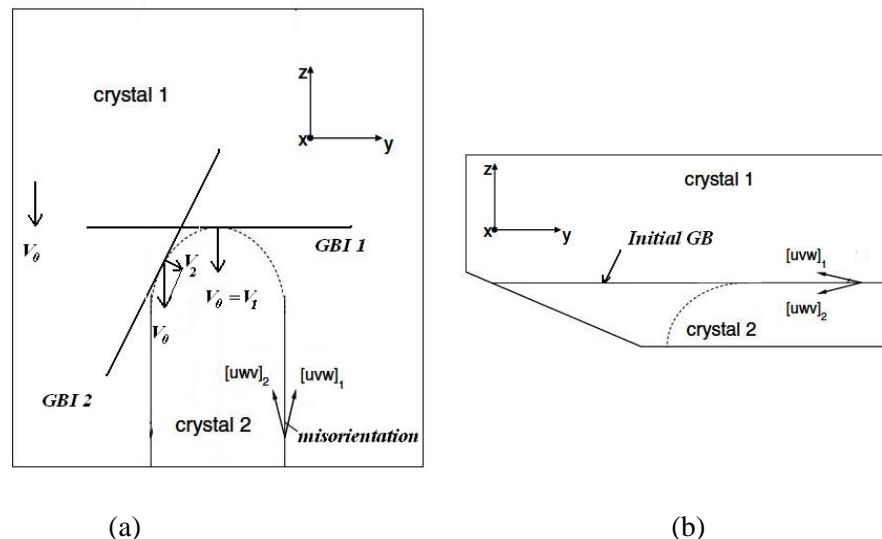


Fig 7.1. Steady state GB migration (half-loop) geometry as proposed for MD estimation of GB mobility (a) and (b) – geometry, often used for experimental GB mobility estimation.

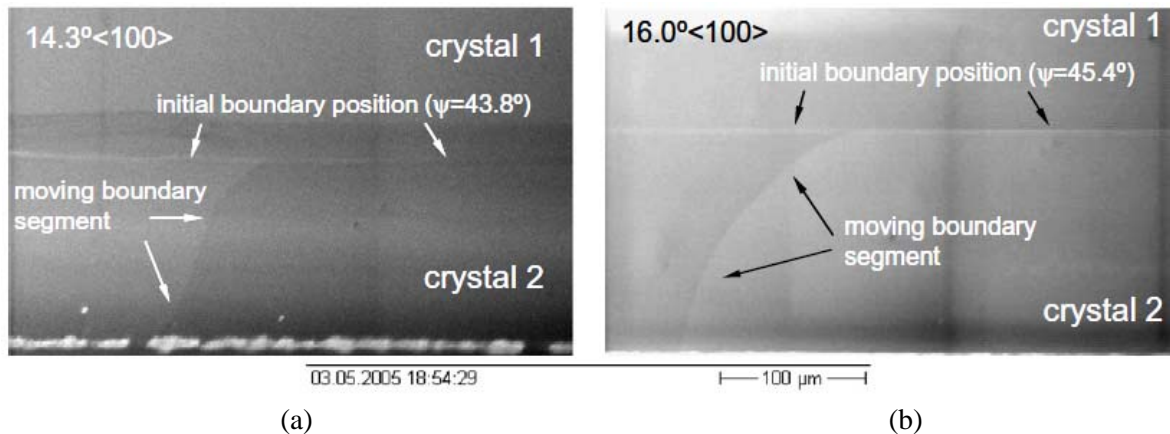


Fig. 7.2. Experimental GB mobility estimation for Al alloy [11]. (a) low temperature, essential GBI dependence (three nearly flat segments), (b) high temperature, almost no GBI dependence.

Generally, the driving force for grain growth is the reduction of the free energy; this reduction is accomplished by the migration of the grain boundary. For half-loop geometry the source for the driving force is **the area of the boundary**, however other sources can contribute to the driving force and hence to grain boundary motion. Such sources can be given by a gradient of any intensive thermodynamic variable, for example, a gradient of temperature, pressure, a magnetic field (Figure 7.3) [12-14], etc.

Hence, by introducing the external driving force of any nature, not depending on GB curvature, it is possible to study GB effective mobility for a simple flat GB, having the same GBI in each point. For modeling purposes no matter what is the driving force nature. It just can be introduced as constant vector adding to the interatomic interaction potential.

Initial calculations were started to show, that energy effect both from additional driving force and GBI can characterize the GBI effect on GB effective mobility.

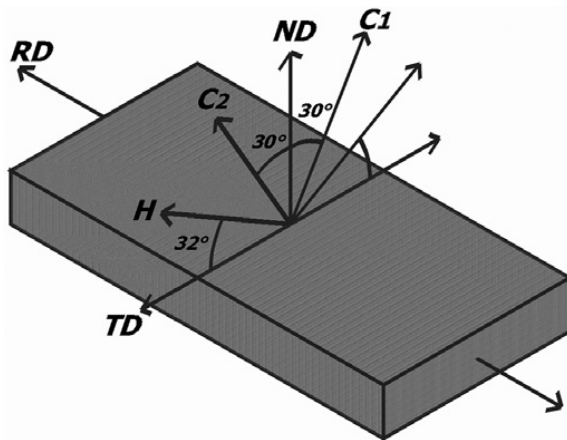


Fig. 7.3. Example of spatial orientation of the rolled sample with respect to the magnetic field H, provides essential driving for GBs force due to the anisotropy of the magnetic susceptibility of titanium (magnetic annealing of titanium, [12])

Two techniques were initially developed using previously proposed approaches for estimating the mobility of a single GB as function of both GBI and GBM.

The first one is an attempt to model GB migration in traditional bicrystal half-loop geometry (Fig.3.1a) This geometry allows investigating the shape of a moving grain boundary and using it as a source of data with regard to the GBI dependence of GB mobility.

The second technique for MD GB mobility estimation is based on the introducing of external driving force which does not depend on GB curvature. This technique was being developed to the study of GB effective mobility for a simple flat GB having the same GBI in each point.

First set of calculations was completed for the (0,0,0) (20,20,20) misoriented boundary. The Born-Mayer potential was used with adding of a constant vector force for affecting each atom within the thin volume close to GB (within 3 lattice periods from GB).

For this particular case no essential influence an external force on GBI energy dependence was seen. The only effect was nearly constant difference in absolute values. The normalized dependencies were similar (see Fig. 7.4). It is also possible, that we selected GB area too wide, and as the result could not see differences in the “relaxed” energies. So, we apply additional driving force for thinner layer around GB.

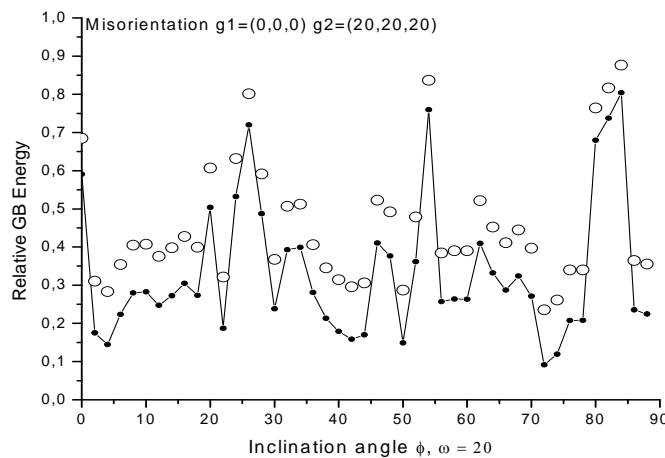


Fig. 7.4. Relative GB energy for (0,0,0) (20,20,20) misoriented GB as function of GBI component ϕ . Open circles are GB energy values when additional driving force is effective.

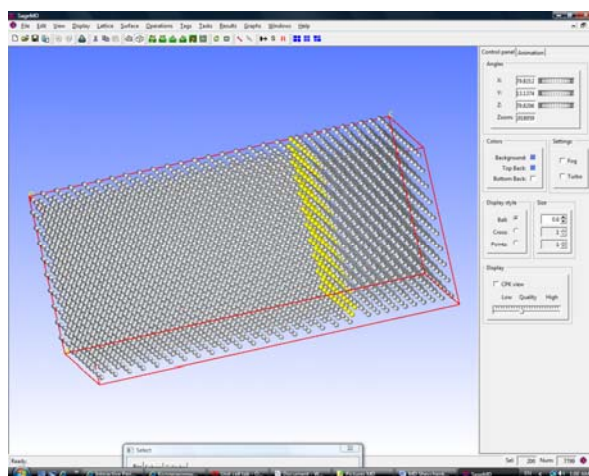


Fig. 7.5. Example of flat relaxed GB in MD simulation

An attempt to model GB migration in traditional bicrystal half-loop geometry was performed. This geometry allows investigating the shape of a moving grain boundary and using it as a source of data with regard to the GBI dependence of GB mobility.

First two runs for $\Sigma 9$ GB and 5 runs for general symmetric tilt boundaries were completed. It was shown, that the movement of such GBs in modeling volume are too slow, and, as expected, they require a huge amount of computational time to build even simple one-dimensional graph.

Hence, to show effects of GBI inclination accounting on grains shape an recrystallization kinetics, it was decided to use data for relative GB energy as effective mobilities for 3D MC Potts modeling code...

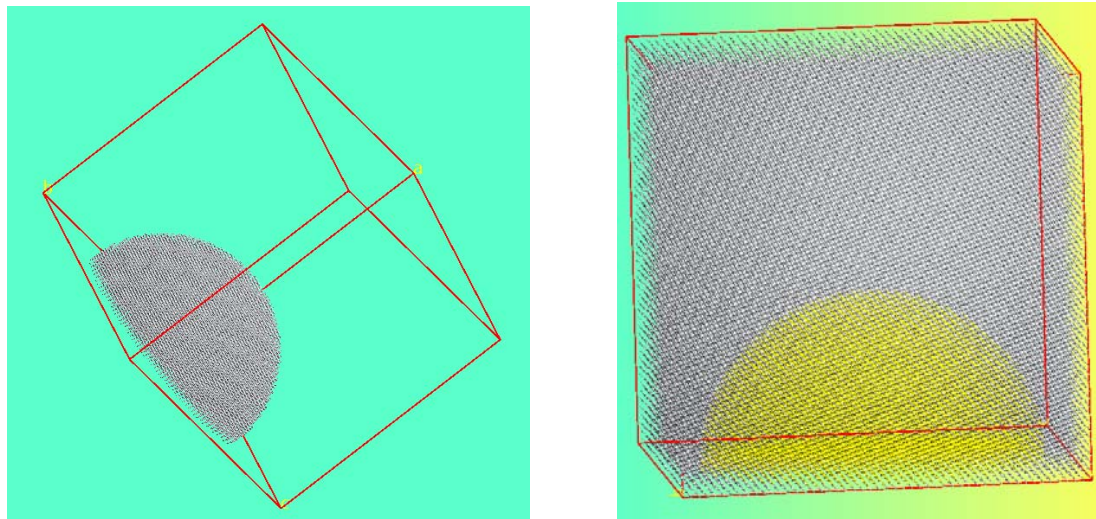


Fig. 7.6. Migrating hemispheric GB geometry used in MD simulation.

8. TOOL FOR ANALYSIS OF NOT RELAXED GB GEOMETRY

As additional tool was developed (Fig. 9.1) for analysis of not relaxed GB geometry. It allows setting lattice misorientation in terms of rotation axis and rotation angle and visualizing the CSL pattern by showing sites of the misoriented lattice which occupy the same or slightly different (difference in position not more than chosen) positions.

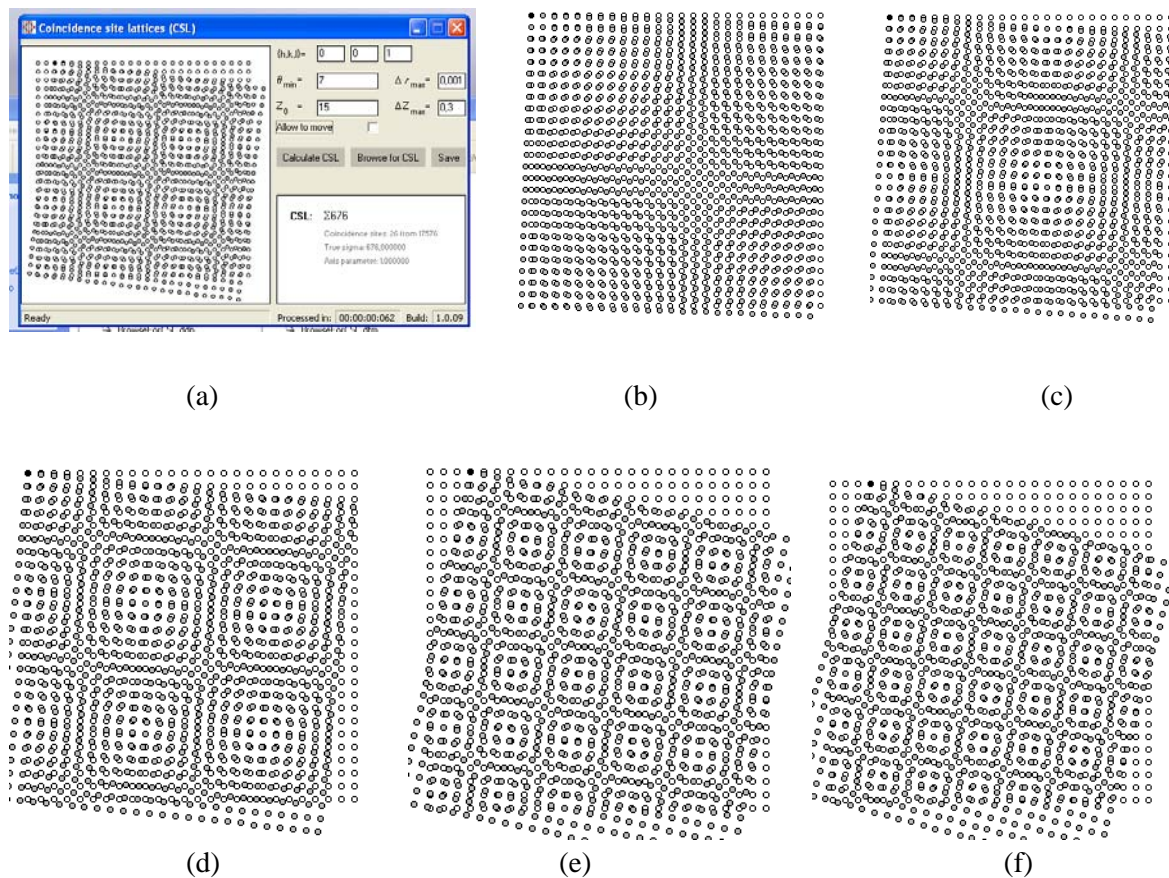


Fig.8.1 CLS visualization tool (a) and CSL patterns changing from LABs to HABs (twist GB, $\Theta= 2$ deg. (b), 4 deg. (c), 6 deg. (e) 12 deg and (f)15 deg).

9. PUBLICATIONS IN THE FRAMES OF THE PROJECT:

1. Ivasishin O.M., Shevchenko S.V., Semiatin S.L., Implementation of exact grain-boundary geometry into a 3-DMonte-Carlo (Potts) model for microstructure evolution. *Acta Materialia*, **57**, 2009, 2834-2844.
2. Shevchenko S.V., Ivasishin O.M., Gazder A., Pereloma E., 3D Monte-Carlo simulation of microstructural evolution upon heating of deformed LCB titanium alloy, presented at TMS 2010 Annual Meeting, to be published in “Metal Physics and Advanced Technologies”

10. LIST OF REFERENCES

- [1] Ivasishin O.M., Shevchenko S.V., Vasiliev N.L., Semiatin S.L.. A 3-D Monte-Carlo (Potts) model for recrystallization and grain growth in polycrystalline materials. *Materials Science and Engineering A*, **433**, 2006, 216-232.
- [2] Raghavan S., Satyam S., Modeling the grain growth kinetics by cellular automation. *Materials Science and Engineering A*, **445-46**, 2007, 203-209.
- [3] Amouyal Y., Rabkin E., Mishin Yu., Correlation between grain boundary energy and geometry in Ni-rich NiAl. *Acta Materialia*, **53**, 2005, 3795-3805.
- [4] Ivasishin, O.M., Shevchenko, S.V., Vasiliev, N.L., and Semiatin, S.L, *Acta Mater.*, 2003, 51, 1019-1034.
- [5] A.P. Sutton and R.W. Balluffi, in: *Interfaces in Crystalline Materials*, Clarendon Press, Oxford, 1995
- [6] <http://www.ks.uiuc.edu/Research/vmd/>; Jin Yu, Andrea J. Yool, Klaus Schulten, and Emad Tajkhorshid. *Structure*, 14:1411-1423, 2006.
- [7] B.W. Zhang, Y.F. Ouyang, *Phys R. B*, 262, 1999, p.218-221.
- [8] J.M. Zhang, Y.H. Huang, Energy calculation for symmetrical tilt boundaries in iron. *Appl. Surf. Sci.* 265, 2006, 4936-4942.
- [9] Luzzi, D.E., *Phil. Mag. Lett.*, **63**, 1991, 281-287.
- [10] G. Gottstein, L.S. Shvindlerman. In. *Grain Boundary Migration in Metals*, CRC Press, 2000, p.48.
- [11] D.M. Kirch, E. Jannot, L.A. Barrales-Mora, D.A. Molodov *, G. Gottstein *Acta Mater.* 56 (2008) 4998.
- [12] D.A. Molodov, A.D. Sheikh-Ali, *Acta Mater.* 52 (2004) 4377.
- [13] D.A. Molodov, P.J. Konijnenberg, N. Bozzolo, A.D. Sheikh-Ali, *Mater. Lett.* 59 (2005) 3209.
- [14] D.A. Molodov, G. Gottstein, F. Heringhaus, L. S. Shvindlerman, True absolute grain boundary mobility: motion of specific planar boundaries in Bi-bicrystals under magnetic driving forces, *Acta Mater.*, 46 (1998) 5627
- [15] N. Gokon M. Kajihara, *Materials Science and Engineering A* 477 (2008) 121.

11. LIST OF SELECTED REFERENCES, STAGE 3

1. V. Randle, G.S. Rohrer, H.M. Miller, M. Coleman, G.T. Owen, Five-parameter grain boundary distribution of commercially grain boundary engineered nickel and copper, *Acta Materialia*, **56**, (2008)1279-1287
2. B. Schonfelder, G. Gottstein, L.S. Shvindlerman, Comparative study of grain-boundary migration and grain-boundary self-diffusion of [001] twist-grain boundaries in copper by atomistic simulations. *Acta Materialia* **53** (2005) 1597-1609.
3. Byeong-Joo Lee, Je-Wook Jang. A modified embedded-atom method interatomic potential for the Fe-H system *Acta Materialia* **55** (2007) 6779-6788.
4. M. Winning, G. Gottstein, L.S. Shvindlerman, On the mechanisms of grain boundary migration, *Acta Materialia* **50** (2002) 353-363.
5. Jian-Min Zhang, Yu-Hong Huang, Xi-Jun Wu, Ke-Wei Xu, Energy calculation for symmetrical tilt grain boundaries in iron, *Applied Surface Science* **252** (2006) 4936-4942.
6. Rasmus B. Godiksen, Zachary T. T., Moneesh U., Jakob S., D. Juul Jensen, S. Schmidt, Simulations of boundary migration during recrystallization using molecular dynamics, *Acta Materialia* **55** (2007) 6383-6391.
7. F.R.N. Nabarro, Atomistic models of a grain boundary in a square lattice. *Materials Science and Engineering A* **409** (2005) 120-124.
8. T. Uehara, N. Wakabayashi, Y. Hirabayashi, N. Ohno, An atomistic study of grain boundary stability and crystal rearrangement using molecular dynamics techniques, *International Journal of Mechanical Sciences*, in press.
9. H. Zhang, M. I. Mendelev, D.J. Srolovitz, Mobility of $\Sigma 5$ tilt grain boundaries: Inclination dependence, *Scripta Materialia* **52** (2005) 1193-1198.
10. Y. Amouyal, E. Rabkin, A scanning force microscopy study of grain boundary energy in copper subjected to equal channel angular pressing, *Acta Materialia* **55** (2007) 6681-6689.
11. T. Skidmore, R. G. Buchheit, M. C. Juhas, Grain boundary energy vs. misorientation in Inconel 600 alloy as measured by thermal groove and OIM analysis correlation, *Scripta Materialia* **50** (2004) 873-877.
12. J. Gruber, D. C. George, A. P. Kuprat, Effect of anisotropic grain boundary properties on grain boundary plane distributions during grain growth, *Scripta Materialia* **53** (2005) 351-355.
13. P. Lejceka, V. Havlova, Growth of metallic bicrystals with high-energy grain boundary, *Journal of Crystal Growth* **275** (2005) e1591-e1596.
14. A. E. Lobkovsky, A. Karma, M. I. Mendelev, M. Haataja, D. J. Srolovitz, Grain shape, grain boundary mobility and the Herring relation, *Acta Materialia*, **52**, Pages 285-292.
15. A. Kazaryan, Y. Wang, S. A. Dregia, B. R. Patton, Grain growth in anisotropic systems: comparison of effects of energy and mobility. *Acta Materialia*, **50**, Pages 2491-2502.
16. Huifang Zhang, Harris Wong, Coupled grooving and migration of inclined grain boundaries: Regime II *Acta Materialia*, **50**, Pages 1995-2012.
17. G. Gottstein, D. A. Molodov, L. S. Shvindlerman, D. J. Srolovitz, M. Winning, Grain boundary migration: misorientation dependence, *Current Opinion in Solid State and Materials Science*, **5**, Pages 9-14
18. N. Goukon, T. Ikeda, M. Kajihara, Ke-Wei Xu, Characteristic features of diffusion induced grain boundary migration for $\Sigma 9$ [110] asymmetric tilt boundaries in the Cu(Zn) system, *Acta Materialia*, **48**, Pages 1551-1562
19. D. A. Molodov, G. Gottstein, L. S. Shvindlerman, True grain boundary mobility: motion of specific planar boundaries in Bi-bicrystals under magnetic driving forces, *Acta Materialia*, **46**, (1998), Pages 5627-5632
20. V. Semenov, E. Rabkin, E. Bischoff, W. Gust, The effect of the grain boundary misorientation on the kinetics of the discontinuous ordering reaction in Fe-50 at.%Co. *Acta Materialia*, **46**, (1998), Pages 2289-2298
21. Diana Farkas, Som Mohanty, Joshua Monk, Strain-driven grain boundary motion in nanocrystalline materials, *Materials Science and Engineering: A* **493**, (2008), Pages 33-40.
22. L. Van Brutzel, E. Vincent-Aublant, Grain boundary influence on displacement cascades in UO_2 : A molecular dynamics study, *Journal of Nuclear Materials*, **377**, (2008), Pages 522-527.

23. David L. Olmsted, Stephen M. Foiles, Elizabeth A. Holm, Grain boundary interface roughening transition and its effect on grain boundary mobility for non-faceting boundaries, *Scripta Materialia*, **57**, (2007), Pages 1161

24. Diana Farkas, Anders Frøseth, Helena Van Swygenhoven, Grain boundary migration during room temperature deformation of nanocrystalline Ni, *Scripta Materialia*, **55**, (2006), Pages 695-698.

25. V. Yamakov, D. Moldovan, K. Rastogi, D. Wolf, Relation between grain growth and grain-boundary diffusion in a pure material by molecular dynamics simulations, *Acta Materialia*, **54**, (2006), Pages 4053-4061.

26. Stephen M. Foiles, J.J. Hoyt, Computation of grain boundary stiffness and mobility from boundary fluctuations, *Acta Materialia*, **54**, (2006), Pages 3351-3357.

27. Lang Zhou, Hao Zhang, David J. Srolovitz, A size effect in grain boundary migration: A molecular dynamics study of bicrystal thin films, *Acta Materialia*, **53**, (2005), Pages 5273-5279.

28. H. Zhang, M. Upmanyu, D.J. Srolovitz, Curvature driven grain boundary migration in aluminum: molecular dynamics simulations, *Acta Materialia*, **53**, (2005), Pages 79-86.

29. U. Wolf F. Ernst ; T. Muschik ; M. W. Finnis, The influence of grain boundary inclination on the structure and energy of $\sigma = 3$ grain boundaries in copper, *Philosophical Magazine A*, **66**, 1992, 991-1002.

30. Onur Saray, Gencaga Purcek, Microstructural evolution and mechanical properties of Al-40 wt.%Zn alloy processed by equal-channel angular extrusion
Journal of Materials Processing Technology, Volume 209, Issue 5, 1 March 2009, Pages 2488-2498.

31. Irene J. Beyerlein, László S. Tóth, Texture evolution in equal channel angular extrusion. *Progress in Materials Science*, In press, available online 20 February 2009

32. M. Asta, C. Beckermann, A. Karma, W. Kurz, R. Napolitano, M. Plapp, G. Purdy, M. Rappaz, R. Trivedi Solidification microstructures and solid-state parallels: Recent developments, future directions. *Acta Materialia*, Volume 57, Issue 4, February 2009, Pages 941-971.

33. G. Gottstein, D. A. Molodov, L. S. Shvindlerman, D. J. Srolovitz, M. Winning, Grain boundary migration: misorientation dependence, *Current Opinion in Solid State and Materials Science*, **5**, Pages 9-14

34. Shen J. Dillon, Gregory S. Rohrer, Mechanism for the development of anisotropic grain boundary character distributions during normal grain growth. *Acta Materialia*, Volume 57, Issue 1, January 2009, Pages 1-7.

35. D. A. Molodov, G. Gottstein, F. Heringhaus, L. S. Shvindlerman, True absolute grain boundary mobility: motion of specific planar boundaries in Bi-bicrystals under magnetic driving forces, *Acta Materialia*, **46**, (1998), Pages 5627-5632

36. V. Semenov, E. Rabkin, E. Bischoff, W. Gust, The effect of the grain boundary misorientation on the kinetics of the discontinuous ordering reaction in Fe-50 at.%Co. *Acta Materialia*, **46**, (1998), Pages 2289-2298

37. H. Zhang, M. Upmanyu, D.J. Srolovitz, Curvature driven grain boundary migration in aluminum: molecular dynamics simulations, *Acta Materialia*, **53**, (2005), Pages 79-86.

38. Diana Farkas, Som Mohanty, Joshua Monk, Strain-driven grain boundary motion in nanocrystalline materials, *Materials Science and Engineering: A* **493**, (2008), Pages 33-40.

39. L. Van Brutzel, E. Vincent-Aublant, Grain boundary influence on displacement cascades in UO_2 : A molecular dynamics study, *Journal of Nuclear Materials*, **377**, (2008), Pages 522-527.

40. Vera G. Sursaeva, Boris B. Straumal, Alena S. Gornakova, Lasar S. Shvindlerman, G. Gottstein, Effect of faceting on grain boundary motion in Zn. *Acta Materialia*, Volume 56, Issue 12, July 2008, Pages 2728-2734.

41. David L. McDowell, Viscoplasticity of heterogeneous metallic materials
Materials Science and Engineering: R: Reports, Volume 62, Issue 3, 29 August 2008, Pages 67-123.

42. M. Reihanian, R. Ebrahimi, M.M. Moshksar, D. Terada, N. Tsuji, Microstructure quantification and correlation with flow stress of ultrafine grained commercially pure Al fabricated by equal channel angular pressing (ECAP) *Materials Characterization*, Volume 59, Issue 9, September 2008, Pages 1312-1323.

12. LIST OF SYMBOLS, ABBREVIATIONS, AND ACRONYMS

- 1) *MC* – Monte Carlo
- 2) *MU* – Modeling unit, modelling units form the Monte Carlo Potts modelling volume.
- 3) *MD* – molecular dynamics;
- 4) *GB* – grain boundary;
- 5) *GBI* – grain boundary inclination;
- 6) *GBM* – grain boundary misorientation;
- 7) $M_o(x, y, z)$ – Current MU position.
- 8) *R* – GB curvature radius.
- 9) *n* – normal for planar linear approximation
- 10) *m* – GB tangential plane normal
- 11) *M* – GB misorientation (matrix form)
- 12) ε – GB misorientation (scalar form)
- 13) *ODF* – orientation distribution function
- 14) *TTC* – tilt/twist component
- 15) *BW* – texture band width;
- 16) *SBG* – subgrain size;
- 17) *LAB* – low angle GB;
- 18) *HAB* – high angle GB;
- 19) *MCS* – Monte Carlo step;
- 20) *CA* – Cellular automata;
- 21) *STGB* – Symmetrical tilt grain boundary;
- 22) *VMD* – Visual molecular dynamics;
- 23) *CLS* – Coinside Lattice Structure (Sites)



Prof. O.M.Ivasishin

Project manager